ANALYSIS OF CRASHWORTHINESS OF THE DIMPLED THIN-WALLED STRUCTURES

CE LIANG

A thesis submitted to the University of Sussex

For the degree of Doctor of Philosophy

December 2017

Declaration

I hereby declare that this thesis has not been and will not be, submitted in whole or in part to another university for the award of any other degree.

Ce Liang

Signature: .....

Date: .....

Abstract

Thin-walled structures are often used as kinetic energy absorbers in vehicular systems and infrastructure designs. In such applications, high specific energy absorption is usually desirable, because it is beneficial for weight reduction. The dimpling cold-roll metal forming process introduces dimpled geometry and increases the strength of sheet metal. This thesis aims to investigate the energy absorption characteristics of the dimpled thin-walled structures.

A finite element (FE) modelling analysis was performed using ANSYS Explicit Dynamics solver, to predict the response of dimpled structures to dynamic and quasi-static loads. A series of experimental tests were conducted and the FE method was validated through comparing the numerical and experimental results.

To understand the response of the dimpled structural components to axial crushing loads, numerical simulations were performed. A parametric study on a key cold-roll forming parameter “forming depth” was carried out to evaluate its effects on the dimpled geometry and material properties. Through the parametric study, manufacturing parameters for the cold-roll forming process were suggested to improve yield strength and energy absorption performance of dimpled steel components. It was shown that the specific energy absorption can be increased by up to 16% after optimizing the forming depth.

To take the most advantage of the dimpled geometry, multi-layer dimpled thin-walled columns were analysed. The interlocking mechanism of dimpled plates were investigated and an empirical model was proposed to describe the interaction between dimpled plates. It was shown that a considerable amount of energy can be absorbed through the interaction between dimpled walls.

The behaviour of dimpled columns under lateral impact loads was also investigated. It was revealed that the introduced dimpled geometry contributes to reducing the peak impact force without sacrificing the energy absorption capacity. However, this is only valid when at least one end of the dimpled thin-walled column is fully restrained.

Keywords: FE analysis, impact loads, thin-walled structures, crashworthiness

Acknowledgement

First of all, I would like to express my deepest gratitude to my supervisor Dr Chang Jiang Wang, for his guidance and encouragement throughout the duration of this study. He shared his expertise in finite element method as well as his valuable experience. He also provided financial support which enabled me to attend conferences. Without him, this thesis will not be possible. I would also like to thank Prof Diane Mynors for her advice.

I am grateful to Dr Martin English, Dr Van Bac Nguyen and everyone at Hadley Group Technology for their encouragement and support. They contributed to this study by providing samples, testing equipment and financial support for the experimental tests.

I would like to acknowledge the School of Engineering and Informatics of the University of Sussex for the studentship.

My special thanks should be given to my family. I would like to thank my parents for their support financially as well as emotionally. I would like to thank my grandparents for their understanding and support, patient and long waiting. I would like to thank my wife Yitong. Thank you for believing in me, for encouraging me to pursue my dream, and for being tolerant throughout the years. Finally, I would like to dedicate this thesis to my precious daughter Zixuan, whom, I hope, to make proud by studying for this award.

Table of Contents

List of Figures

List of Tables

List of Symbols

A	Cross-sectional area
C	Width of a square section column
c	Sound speed
D	Cowper-Symonds strain rate coefficient
E	Young's modulus
F	Minimum force to initiate relative sliding
I	Second moment of area
L	Column length
L_{eff}	Effective column length
l	Characteristic length of elements
N	Normal force
P	Crushing force
P_m	Mean crushing force
P_{max}	Maximum crushing force
P_{axial}	Axial compressive load
$P_{axial,c}$	Critical axial compressive load
P_y	Squash load
q	Cowper-Symonds strain rate coefficient
t	Thickness
v	Velocity of impactor
v_i	Initial velocity of impactor
Δt_c	Critical time step
δ	Displacement
ε	Strains
η_c	Crush efficiency
λ	Slenderness ratio
μ	Friction coefficient
μ_e	Effective friction coefficient

ν	Poisson’s ratio
ρ	Density
σ	Stress
σ_y	Yield strength
σ_0	Static yield strength

List of Acronyms

CFRP	Carbon Fibre Reinforced Polymer
CFST	Concrete Filled Steel Tubular
DGPM	Dimpled Geometry Plain Material
DOF	Degree of Freedom
EA	Energy Absorption
FE	Finite Element
SEA	Specific Energy Absorption
SFE	Super Folding Element

Chapter 1 Introduction

1.1 Background

Impact loads often cause undesired injury of people and damage of machines. To provide protection against impact loads, such as in accidental vehicle collisions or earthquakes, energy absorbers are widely employed. For the energy absorbers, thin-walled metal/composite structures are commonly adopted, for their high energy absorption capacity, low cost and small weight.

One of the most representative applications of the energy absorbers is the longeron in passenger vehicles. In accidental collisions, the longerons are expected to convert the kinetic energy to internal energy mainly through plastic deformation, to provide maximum protection for passengers. In recent years, there is a considerable number of studies presented, aiming to improve the crashworthiness of longerons, and therefore reaching the ultimate goal of car body weight reduction. Apart from the vehicular systems, good energy absorption characteristics are also crucial for some infrastructures such as guard rails, bollards and pipelines, for the purpose of maintaining stability in events of collisions. Some typical applications of energy absorbers are shown in Fig. 1.1.

The interest of research on energy absorption characteristics was initiated by Alexander in 1960 [2]. In the early-stage researches, analytical and experimental methods were used. During the last two decades, the numerical methods have become the mainstream research approach on this subject, mainly due to the

advancement of the finite element (FE) method, computing power and the limitation of costs of experimental studies.

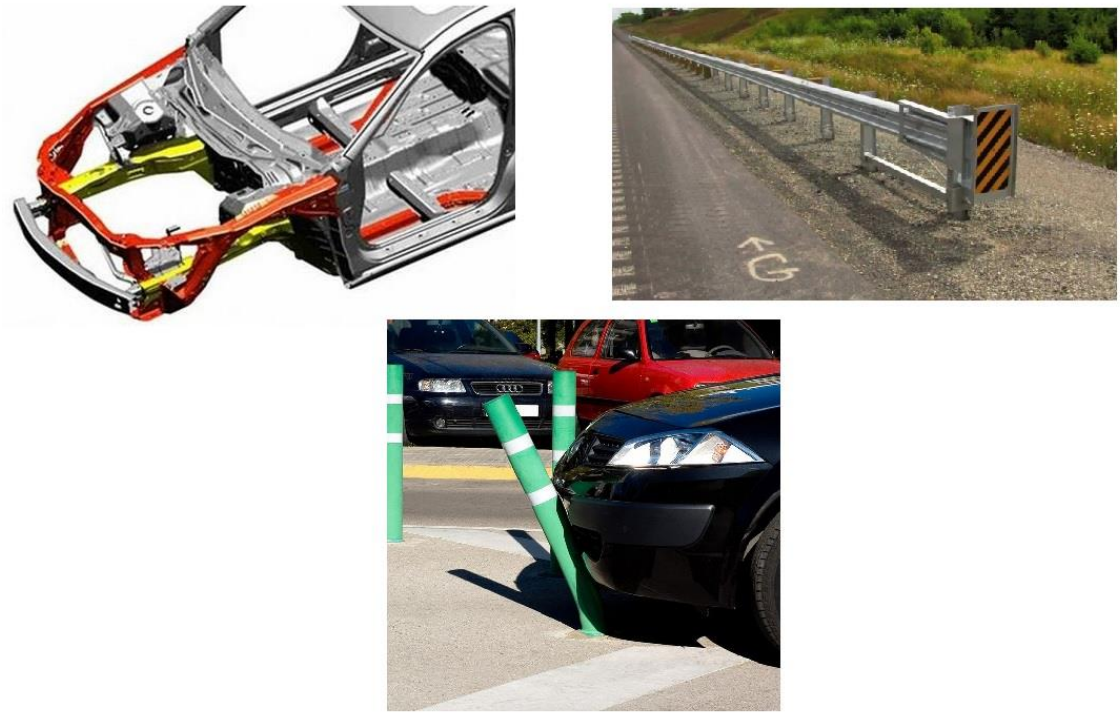

Fig. 1.1. Examples of kinetic energy absorbers

1.2 Research aim and objectives

The aim of the present study is to understand the structural behaviour of the thin-walled structures with dimpled features under axial and lateral impact loads, and propose design strategies to improve energy absorption performance. This aim is achieved through the following objectives:

- Obtaining the mechanical properties of the plain and dimpled steel sheets using both experimental and numerical methods.

- Developing an explicit dynamics finite element modelling method to predict the response of dimpled structural members to low-velocity impact loads, and validating the FE models using experimental data.
- Investigating the behaviour of dimpled thin-walled columns under axial impact loads, and analysing the factors that may influence the axial crushing behaviour.
- Investigating the mechanism of the interaction between two dimpled plates, and therefore proposing innovative structural designs for energy absorbers that can take the most advantage of the dimpled features.
- Investigating the behaviour of dimpled columns under lateral impact loads. Identifying the structural characteristics of the dimpled columns and therefore providing technical support for optimizing the application of dimpled structures.

1.3 Structure of the thesis

This thesis consists of eight chapters. The contents are described below:

Chapter 1 states the background, aim and objectives of the project, and outlines the structure of the thesis.

Chapter 2 presents a comprehensive literature review of the relevant work. The areas include the latest development of thin-walled structures used as kinetic energy absorbers, the UltraSTEEL® dimpling metal forming process, and the theoretical principles of the explicit dynamics finite element method.

Chapter 3 focuses on the UltraSTEEL® forming process and the mechanical properties of the dimpled steel sheets. The forming process is simulated using the FE method. Quasi-static tensile tests are performed experimentally as well as numerically in order to determine the constitutive stress-strain relation, which is critical in the following simulations. The numerical results are validated by the experimentally obtained dimpled geometry and stress-strain curves.

Chapter 4 reports a series of dynamic and quasi-static axial crushing tests on the open section thin-walled columns. The experimental tests are replicated using the explicit dynamics finite element method. The purposes are to validate the FE models as well as to investigate the response of plain and dimpled open section columns to axial crushing loads.

Chapter 5 systematically explores the response of the square closed-section dimpled columns to axial crushing loads. A parametric study has been carried out to understand the effects of forming depth on the material properties and the energy absorption performance. This chapter also investigates the behaviour of dimpled columns under inclined axial impact loads.

Chapter 6 thoroughly investigates the interlocking mechanism between two dimpled plates, and therefore proposes a design strategy which can make use of the interactions of dimpled plates to absorb some extra energy.

Chapter 7 studies the behaviour of dimpled columns under lateral impact loads. The comparison between plain and dimpled columns have been made particularly on the aspect of crush efficiency.

Chapter 8 summaries the main findings of this work. Several topics for future research are suggested.

1.4 Original contributions to knowledge

There are several original contributions in the present work, which improve the understanding of the significance and characteristics of introducing the dimpled feature to thin-walled energy absorbers. A brief summary of the original contributions to the body of knowledge is given as follow.

- A series of experimental tests and the corresponding finite element simulations were carried out to investigate the crashworthiness of the plain and dimpled box-profile columns. The failure modes of the box-profile columns were revealed and the significance of the cutting techniques was pointed out. The knowledge obtained is useful for developing the manufacturing process of thin-walled kinetic energy absorbers.
- The behaviour of dimpled columns under perfect and inclined axial impact loads was investigated and compared with the conventional plain columns. It increased the understanding of the influence of the introduced dimpled geometry and the change in material properties on the energy absorption performance.
- A thorough study on the forming depth was carried out. The influence of forming depth on the mechanical properties of the dimpled material was revealed and explained. Additionally, the influence of forming depth on energy absorption performance was carefully analysed. The knowledge obtained supported the optimization of the dimpling process to suit different engineering applications.
- The interlocking mechanism between dimpled plates was studied. The empirical model and equation to predict the dimple-to-dimple interaction were established. It is helpful for the innovative structural designs involving

dimpled features. The dimpled multi-layer energy absorbers were also investigated.

- The behaviour of dimpled structural members when subjected to lateral impact loads was studied. By predicting the response of the dimpled columns to various types of lateral impact loads, the characteristics and conditions of the dimpled columns were found out and presented.

In addition to the above contributions to knowledge, this study has also helped the industrial collaborator to understand its products better by answering the following two questions:

(a) How does the dimpled thin-walled structures behave when subjected to medium strain rate impact loads.

(b) How can the energy absorption performance of dimpled structures be improved through optimizing the forming process and structural design.

The results and findings presented in this thesis were shared with the industrial collaborator, which provided technical support for the industrial collaborator to expand market from the original construction sector to the new automotive sector. By the time of completion of this thesis, the industrial collaborator is drafting documents for marketing purposes, based on the content of the thesis.

Chapter 2 Literature review

Thin-walled metal structures are widely used as kinetic energy absorbers in vehicles and infrastructures for their high energy absorbing capability, light weight and low cost. Thin-walled metal energy absorbers are designed to convert kinetic energy into mainly internal energy, through irreversible plastic deformation, which means this kind of energy absorbers will be discarded and replaced once crushed. In operation, the thin-walled structures are subjected to various types of impact loads, where axial impact loads and lateral/transverse impact loads are the two most representative types. The intent of this chapter is to provide a comprehensive review of the up to date development in the research area. The explicit dynamics finite element (FE) method, which is usually used in the research area, is reviewed as a supplement. Furthermore, as this thesis focuses on the energy absorption characteristics of the innovative UltraSTEEL® dimpled structures, the latest development on the UltraSTEEL® forming process and the dimpled material are reviewed as well.

2.1 Thin-walled energy absorbing structures under axial impact loads

Energy absorbers designed to withstand axial crushing loads are often found in sea, land and air vehicles [1], such as the front chassis rails in passenger cars. The requirements of these energy absorbers are to have enough energy absorbing capacity while keeping the crushing force sufficiently low. Additionally,

the energy absorbers are also preferred to be light, cheap, and have a predictable and stable failing mechanism during the entire crushing process. Therefore, the indicators that can be used to evaluate the performance of an energy absorber under axial impact loads include:

- Mean crushing force (P_m, defined in Eq. 2.1)
- Maximum crushing force (P_{max})
- Crush efficiency (η_c, defined in Eq. 2.2)
- Specific energy absorption (SEA, defined in Eq. 2.3)

$$P_m = \frac{\int_0^{\delta_{total}} P d\delta}{\delta_{total}} \tag{2.1}$$

$$\eta_c = \frac{P_m}{P_{max}} \tag{2.2}$$

$$SEA = \frac{Total\ Energy\ Absorbed}{Mass\ of\ deflected\ column} \tag{2.3}$$

Where P represents the crushing force and δ represents the axial deformation of the column top surface (i.e. the shortened distance of the column).

Among all these performance indicators, this thesis focuses on the mean crushing force and the specific energy absorption, because the maximum crushing force and the crush efficiency can be relatively easily reduced by introducing imperfections/triggers.

2.1.1 Failing mechanisms and theoretical prediction of the crashworthiness

The investigation on the response of columns under axial crushing loads was initiated by Alexander over fifty years ago [2]. In 1980s, Wierzbicki, Abramowicz and Jones [1, 3-6] made a significant contribution to this field by proposing and developing the super folding element (SFE) theory to predict the crush response of circular and square section thin-walled columns, which are the most common and conventional sectional profiles. The SFE theory then became the foundation of most of the research works in this field till nowadays. In this section, the SFE theory used on the square section columns is reviewed.

To study the behaviour of square section thin-walled columns under axial crushing loads, Abramowicz and Jones [3] conducted a series of experimental tests. From the experimental results, two generic collapse elements were identified: Type I and Type II, as shown in Fig. 2.1, where C represents the width of the column, and H represents the layer-to-layer distance.

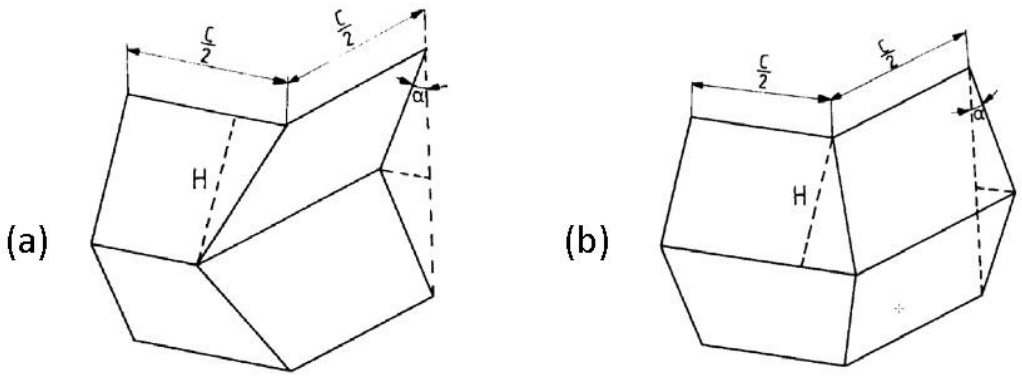

Fig. 2.1. Collapse elements (a) Type I and (b) Type II for square section thin-walled columns [3]

The two generic collapse elements subsequently formed four collapse modes [3]:

- Symmetric collapse mode: all four elements in a layer of folds with a total original height of $2H$ are Type I.
- Asymmetric mixed collapse mode A: there are six Type I and two Type II elements in two adjacent layers of folds with a total original height of $4H$.
- Asymmetric mixed collapse mode B: there are seven Type I and one Type II elements in two adjacent layers of folds with a total original height of $4H$.
- Extensional collapse mode: there is a layer of folds with four Type II elements. However, this collapse mode will only be seen in thick-walled columns, with a width-to-thickness ratio of no larger than 7.5 [7]. Therefore, the extensional collapse mode will not be discussed in this thesis.

The mean crushing forces for the symmetric and two asymmetric collapse modes under quasi-static conditions were then theoretically derived. The derivation was based on the conservation of energy (i.e. the energy absorbed by the column equals to the plastic strain energy developed due to the plastic deformation). The theoretical mean crushing forces for the three collapse modes are presented in Eqs. 2.4 to 2.6 [3], where σ_0 represents the static yield strength of the material, and t represents the uniform wall thickness of the column.

$$P_m = 9.53C^{\frac{1}{3}}t^{\frac{5}{3}}\sigma_0 \qquad \text{(Symmetric)} \qquad (2.4)$$

$$P_m = (8.395C^{\frac{1}{3}}t^{\frac{5}{3}} + 0.73C^{\frac{2}{3}}t^{\frac{4}{3}} + 0.5t^2)\sigma_0 \qquad \text{(Asymmetric A)} \qquad (2.5)$$

$$P_m = (8.885C^{\frac{1}{3}}t^{\frac{5}{3}} + 0.4125C^{\frac{2}{3}}t^{\frac{4}{3}} + 0.25t^2)\sigma_0 \qquad \text{(Asymmetric B)} \qquad (2.6)$$

However, the effective crushing distance observed in experimental tests were only 73% - 77% of the original layer-to-layer distance, depending on the folding element type [3]. Abramowicz and Jones then modified the equations for mean crushing forces by taking the effective crushing distance into account. The modified equations for the mean crushing forces are presented in Eqs. 2.7 to 2.9 [3].

$$P_m = 13.055C^{\frac{1}{3}}t^{\frac{5}{3}}\sigma_0 \quad \text{(Symmetric)} \quad (2.7)$$

$$P_m = (10.9025C^{\frac{1}{3}}t^{\frac{5}{3}} + 0.9475C^{\frac{2}{3}}t^{\frac{4}{3}} + 0.65t^2)\sigma_0 \quad \text{(Asymmetric A)} \quad (2.8)$$

$$P_m = (11.54t^{\frac{5}{3}} + 0.535C^{\frac{2}{3}}t^{\frac{4}{3}} + 0.325t^2)\sigma_0 \quad \text{(Asymmetric B)} \quad (2.9)$$

Abramowicz and Jones then further improved the analytical equations for mean crushing forces by taking the materials' strain rate sensitivity into consideration [3]. The static stress σ was replaced by the dynamic stress σ^d by applying the Cowper-Symonds material model, and the strain rate was estimated based on the initial velocity of the impactor and the dimensions of the column. Therefore, the final equations to predict the mean crushing forces under dynamic loads were derived, as shown in Eqs. 2.10 to 2.12 [3], where v_i represents the initial impact velocity, D and q are Cowper-Symonds coefficients, varying from material to material.

$${P_m}^d = 13.055C^{\frac{1}{3}}t^{\frac{5}{3}}\sigma_0(1 + (\frac{0.33v_i}{CD})^{\frac{1}{q}}) \quad \text{(Symmetric)} \quad (2.10)$$

$$P_m = (10.9025C^{\frac{1}{3}}t^{\frac{5}{3}} + 0.9475C^{\frac{2}{3}}t^{\frac{4}{3}} + 0.65t^2)\sigma_0(1 + (\frac{0.49v_i}{CD})^{\frac{1}{q}})$$

(Asymmetric A) (2.11)

$$P_m = (11.54t^{\frac{5}{3}} + 0.535C^{\frac{2}{3}}t^{\frac{4}{3}} + 0.325t^2)\sigma_0(1 + (\frac{0.41v_i}{CD})^{\frac{1}{q}})$$

(Asymmetric B) (2.12)

Based on the analytical predictions, Abramowicz and Jones [3] carried out a parametric study on the initial impact velocity. It was pointed out that the strain rate effect can significantly affect energy absorption performance (e.g. for mild steel columns, the dynamic mean crushing force can be up to 40% greater than the quasi-static one) [3]. It was also pointed out that the mean crushing forces tend to converge as the impact velocity increasing [3].

The significance of the SFE theory is that it introduced the concept of analytical prediction of the response of square section thin-walled columns to axial crushing loads based on the energy conservation principle, and it enabled further analytical predictions for columns with more complicated cross-sectional profiles. However, the SFE theory has its own limitations. The theoretical model is over-simplified and a large proportion of coefficients involved needs to be adjusted for different loading and support conditions.

2.1.2 Latest research and development in axial crushing energy absorbers

In recent years, there is a particular interest in improving the crashworthiness of thin-walled structures. The research topics can be put into the following three categories.

2.1.2.1 Innovative cross-sectional design

Tang et al. [8] proposed a new strategy to increase the energy absorption capacity of thin-walled columns by introducing non-convex corners in cross sections. Tang et al. [8] carried out analytical and numerical studies and suggested that the essence of this strategy is to distribute a greater proportion of material near the corners. The strategy of adding non-convex corners was then extended by Abbasi et al. [9, 10]. They carried out numerical and experimental studies on hexagonal, octagonal and 12-edge section columns, among which the 12-edge section columns had the highest SEA values [9, 10]. A parametric study on the angle of corners was completed as well. Additionally, the agreement between experimental and numerical results was considered to be good, with errors up to 8.6% [10]. Typical multi-corner sectional profiles are shown in Fig. 2.2. Sun et al. [11, 12] modified the design strategy by replacing the straight lines and right angle corners in the cross sections with the Fourier varying curves, and carried out an optimization study on the design parameters.

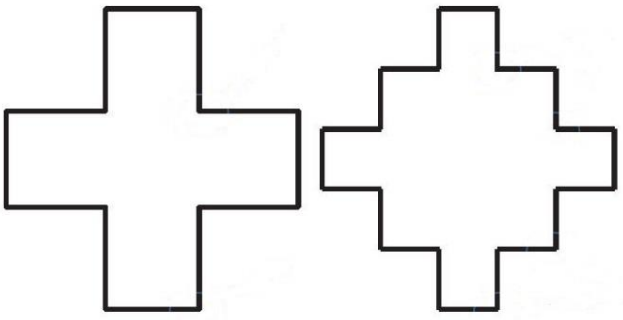

Fig. 2.2. Typical multi-corner sectional profiles [8]

The concept of multi-cell columns was suggested by Chen and Wierzbicki [13]. Theoretical solutions for single-cell, double-cell and triple-cell columns were

reported, and the “multi-cell” strategy was found to significantly increase energy absorption performance [13]. Kim [14] then carried out an optimization study on multi-cell columns, and proposed innovative multi-cell cross-sectional profiles with reinforced corner regions. Zhang et al. [15] further developed the SFE theory by introducing crisscross element and T-shape element, and used the modified SFE theory to predict the energy absorption performance of several square multi-cell columns. Jusuf et al. [16] then used FE and experimental methods to study the energy absorption performance of prismatic multi-cell section columns. It was claimed that with ribs reinforcing the columns, SEA was increased by up to 91.2%, comparing to double-wall columns [16, 17]. Similar research works focusing on the energy absorption performance of multi-cell columns were also presented by Zhang and Cheng [18], Hou et al. [19], Zhang et al. [20], Najafi and Rais-Rohani [21], Zhang and Zhang [22], Tran et al. [23], Wu et al. [24] and Estrada et al. [25]. Vinayagar and Kumar [26] proposed the design of double section bi-tubular thin-walled structures. They assessed the energy absorption performance of circular outer tubes with triangular, square and hexagonal cross-sectional inner tubes, and studied the effects of cross-sectional dimensions [26]. Qiu et al. [27] took off-axis loads into consideration when studying the energy absorption performance of hexagonal multi-cell columns. Tran et al. [28] optimized the geometrical parameters of angle element multi-cell structures. Zhang and Zhang [29] conducted a similar study to optimize the geometrical parameters of quadruple cell section columns. Typical multi-cell sectional profiles are shown in Fig. 2.3.

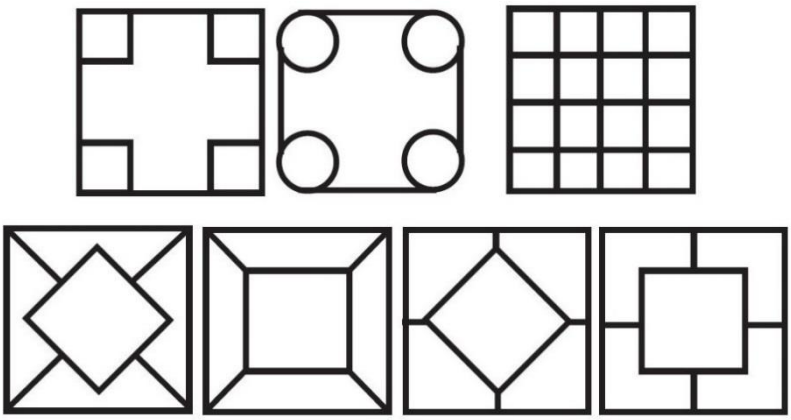

Fig. 2.3. Typical multi-cell sectional profiles [12, 15, 19]

Besides multi-corner and multi-cell cross-sectional profiles, attention has been paid on other innovative sections in previous research. White et al. [30] theoretically studied the crushing characteristics of top-hat and double-hat section columns. Ly et al. [31] then extended the research by using the FE method to optimize the geometrical parameters of top-hat structures. Zhang et al. [32] introduced graded thickness to the corner regions of conventional closed square section columns. It was reported by Zhang et al. that the graded thickness can increase both mean force and crush efficiency by up to 30% - 35% [32]. Asanjarani et al. [33] studied the crashworthiness of tapered thin-walled square tubes with indentations. It was reported that introducing a large number of indentations contributed to improving the crush efficiency, and introducing a medium number of indentations contributed to improving specific energy absorption [33]. Jiang et al. [34] studied the crashworthiness of composite waved beams and carried out a parametric study on triggers. In their study, a wide range of failure modes such as cracking, delamination, fibre fracture was observed in the experimental tests and taken into account in the numerical study [34].

2.1.2.2 High strength materials

Huh and Kang [35] used the explicit dynamics FE method to compare the performance of mild steel and high-strength steel columns under quasi-static and dynamic loading conditions. The Johnson-Cook material model was used by Huh and Kang [35] to handle materials' strain rate sensitivity. A similar research was conducted by Schneider and Jones [36]. By contrast, Schneider and Jones [36] adopted the Cowper-Symonds material model to characterise materials' sensitivity to strain rate. Both studies have revealed that using high-strength material can effectively increase specific energy absorption values, regardless of cross-sectional profiles [35, 36]. In addition to the Johnson-Cook and Cowper-Symonds material models, empirical models were utilized by Xue et al. [37, 38] to characterise the strain rate sensitivity of porous bronze and iron materials. Ying et al. [39] carried out an optimization study on functionally graded strength steel columns under inclined impact loads. Tarigopula et al. [40] studied the response of dual-phase high-strength steel columns to crushing loads, with a particular focus on materials' strain rate effect. Similar to Schneider and Jones's work, Tarigopula et al. also adopted the Copwer-Symonds material properties to characterise materials' strain rate effect under dynamic loads [40]. Additionally, the selection of the Cowper-Symonds coefficients was discussed [40]. Lam et al. [41] used the FE method to analyse the effect of gauge thickness on mild steel, aluminium and magnesium alloy structures' energy absorption performance, when being used as automotive instrument panel supports. Fang et al. [42] investigated the crashworthiness of steel-aluminium hybrid rails in vehicular

systems. In their study, the steel part and the aluminium part were connected using welding techniques. It was reported that the hybrid design was able to reduce peak force as well as enhance energy absorption capacity, comparing to mono-material structures [42]. Reddy and Zhang [43] experimentally studied the effects of heat treatment on columns' response to axial crushing loads. It was pointed out that the removal of strain hardening may result in an overall loss of stability in some cases [43].

2.1.2.3 Filling thin-walled columns

A number of research focused on improving the crashworthiness through filling columns with various types of fillers, especially foams. In 1966, Shaw and Sata [44] studied the mechanical behaviour of foams, and came up with a three-region stress-strain model for foams. Reid et al. [45] tested the tubes with polyurethane foam fillers and their hollow counterparts. Moreover, the effect of the density of foams was covered in their study [45]. It was pointed out that susing foam fillers can considerably increase crashworthiness, due to the strength of foams as well as the interaction between foams and metal walls [45]. This theory was further justified by Zarei et al. [46] through a series of numerical and experimental studies. Abramowicz et al. [47] extended their previous studies to analytically predict the behaviour of the foam-filled structures. Hanssen et al. [48] suggested empirical equations to predict the energy absorption performance of foam-filled thin-walled tubes. These empirical equations were then validated by experimental tests and modified by taking dynamic loading conditions into account [49]. Seitzberger et al. [50, 51] conducted a series of experiments to study the energy

absorption performance of various cross-sectional foam-filled columns. Zhang et al. [52] used experimental and numerical methods to study the energy absorption performance of the thin-walled columns filled with functionally graded foams. It was reported that using foam fillers can considerably improve energy absorption performance [50, 51, 52]. Although there were a lot of promising research results on foam-filled thin-walled structures, it was suggested by Thornton et al. that using polyurethane foam fillers was not as effective as increasing the wall thickness in terms of weight efficiency [53].

Although most of the research in recent years focused on increasing mean crushing force or specific energy absorption, it is worth noting that there is a small proportion of research focusing on increasing the crush efficiencies by reducing maximum crushing forces. Song et al. [54] introduced origami patterns along the longitudinal direction of columns. Their study revealed that the pre-existing origami patterns can effectively reduce the maximum crushing force as well as promote a more uniform crushing process than conventional columns [54].

In previous numerical studies, triggering mechanisms were often used to initiate the crushing process and compensate the difference between numerical simulations and experimental tests. The positions of the triggers were specified based on experimental observations. There are two types of triggering mechanisms. The first type is to create an initial geometrical imperfection, as used by Jusuf et al. [16, 17]. The second type is to introduce indentation triggers on the outside plates of columns, as used by Zhang et al. [29, 32]. The use of both types of triggering mechanisms has been previously justified.

2.2 Thin-walled energy absorbing structures under lateral impact loads

Thin-walled tubular members are widely used in many infrastructures and vehicular systems. It has been identified in some previous researches that hollow tubular members are prone to transverse impact loading [55]. Past research and statistical data have revealed that accidental vehicular collision is one of the main causes of structural failure [56, 57]. The collision energy is absorbed by the tubular members subjected to bending conditions. Similarly, bumpers and B-pillars are required to provide good energy absorption performance through bending in order to protect the driver and passengers in event of collisions [58]. Therefore, the indicators commonly used to evaluate energy absorption performance or structural stability of thin-walled tubular members subjected to lateral loads include:

- Mean crushing (P_m, defined in Eq. 2.1, where δ represents the lateral displacement at the impact location in this case.)
- Permanent lateral displacement at the impact location under a specific impact load. Although this indicator is widely used, it can be considered as an alternative interpretation of the mean crushing force. Both two indicators are used to describe the energy absorption capacity under lateral impact loads.
- Maximum crushing force (P_{max})
- Crush efficiency (η_c, defined in Eq. 2.2)

- Critical axial to squash load ratio ($\frac{P_{axial,c}}{P_y}$), where P_{axial} represents the axial compressive loads applied to the column, and P_y represents the squash load of the column. The column will lose stability under the lateral impact load and an axial load larger than the critical axial load. This indicator is used to describe columns' ability to maintain stability under combined axial compressive and lateral impact loads. This loading condition is usually found in infrastructural applications.

Among the indicators mentioned above, this thesis focuses on the mean crushing force, crush efficiency and critical axial to squash load ratio in particular when evaluating the performance of structural members subjected to lateral impact loads.

The interest in understanding the mechanisms of bending collapse can be dated back to 1970s. In 1979, Kecman [59] presented his in-depth experimental and theoretical study on the bending collapse mechanisms of rectangular section tubes. Kecman [60] then summarized his study and proposed simple failure mechanisms involving stationary and moving plastic hinge lines, as illustrated in Fig. 2.4. The foundation of Kecman's theory is assuming that the walls deform along the concentrated yield lines only, and the walls are incompressible and inextensible [60]. The simplified models proposed and developed by Kecman were then widely adopted in other research for crush calculations analytically as well as computationally. However, Kecman's analytical method is semi-empirical, because experimental tests are required to determine the 'rolling-radius' parameter.

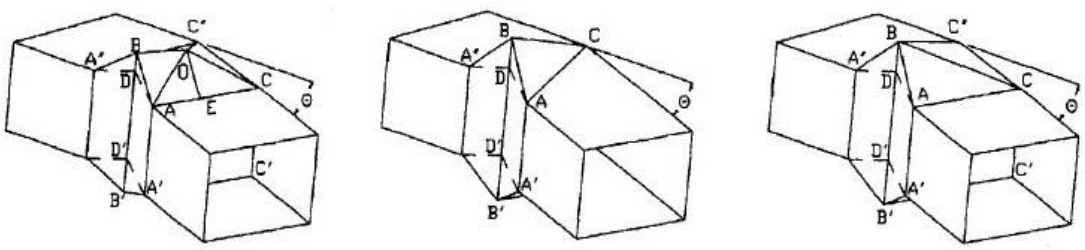

Fig. 2.4. Simplified bending collapse modes of a rectangular section column [60]

Abramowicz [61] then proposed a similar method to Kecman's to theoretically predict the behaviour of thin-walled columns and beams under lateral impact loads. However, only a theoretical study was presented without the support of experimental data [61]. Liu and Jones [62] conducted a series of experimental tests with impact locations varying from the mid-span to the immediate vicinity of a support, in order to validate the theoretical solutions. It was reported by Liu and Jones [62] that the experimental and theoretical permanent deformations of the beams were in very good agreement. Additionally, attention was also put on the beam failure modes, where the beam failure was classified as tensile tearing and shear failure [62]. Yu and Jones [63] carried out further numerical and experimental research on this subject by taking the strain rate effects of mild steel and aluminium alloy into account.

In 1994, Wierzbicki et al. [64] extended the SFE theory, which was originally developed for axially loaded columns. Wierzbicki et al. [64] introduced a new element to analytically solve the bending process of rectangular section columns. Additionally, Wierzbicki et al. [64] unified the three mechanisms shown in Fig. 2.4 by using a floating neutral axis whose position can be determined based on the force equilibrium. Moreover, Wierzbicki et al. [64] used a computational method

to validate their theory and examined the stress distribution along the cross section of columns.

The significant effects of the axial compressive loads on the behaviour of tubular members under lateral impact loads in constructional applications were pointed out by Zeinoddini et al. [65]. Prior to the research of Zeinoddini et al. [66], most of attention was paid to the effects of imperfections when analysing the structural reliability in events of collisions. It was reported that the level of damage in tubes was more dependent on the level of axial pre-load than on the change of imperfection effects [66]. In order to investigate the role of the operating axial compressive loads in event of collisions, Zeinoddini et al. [66] carried out experimental tests on steel tubes with axial compressive load varying from 0 to 75% of the squash load. In the experiments, the axial loads were applied using a spring-disc system, which was able to provide nearly constant compressive loads. The experimental study was then replicated using the finite element method by Zeinoddini et al. [67]. Zeinoddini et al. validated the finite element method using previous experimental results, then used the validated FE method to extend the study by taking the damping effect and strain rate sensitivity of the material into account. Al-Thairy and Wang [68-71] carried out a series of studies to investigate the behaviour of axially compressed steel columns under lateral impact loads. They validated their FE method by comparing against the experimental results reported by Zeinoddini et al. [66]. Al-Thairy and Wang [68] then used the validated FE method to conduct a parametric study on the axially loaded columns subjected to lateral impact loads. It was concluded that the dominant factor for the structural failure was the impact kinetic energy rather than the impact velocity and impactor mass [68]. To address the industrial needs

better, Al-Thairy and Wang [69] developed a simplified analytical method to predict critical velocities, based on the assumption of energy conservation. As quasi-static behaviour was assumed, the simplified analytical method was only suitable for low-velocity collisions [69]. Al-Thairy and Wang then further developed the analytical method to predict the critical velocity of vehicle impact loads [70], and developed a simplified FE model to predict the response of axially loaded steel columns to lateral vehicle impact loads [71].

In recent years, a number of studies were carried out, aiming to improve the resistance of structural members to lateral impact loads. Some studies focused on strengthening hollow tubular members with various types of fillers [72-79, 87]. By contrast, some studies focused on strengthening methods by applying extra reinforcement such as carbon fibre [81-87].

Santosa and Wierzbicki [72] employed analytical and numerical methods to investigate the resistance of low-density metal (aluminium foam and honeycomb core) filled thin-walled columns to lateral impact loads. It was claimed that the fillers significantly improved the resistance, where the adhesive force played an important role [72]. However, the crushing resistance of the low-density metal fillers must be selected with caution, in order to avoid undesired tensile necking [72]. It was also claimed that using those fillers were more preferable than thickening the column walls, on the aspect of weight reduction [72]. Chen [73] performed experimental tests and numerical simulations to study the collapse behaviour of aluminium foam-filled hat profile columns under lateral impact loads. Shahbeyk et al. [74] did a similar research with focuses on various parameters such as spot welding failure, flange location, sheet metal thickness, glue

presence and foam filling. Fang et al. [75] added further contribution to this research topic by performing a numerical optimization study on the parameters of functionally graded foam fillers and metal walls. Besides aluminium foam and honeycomb core, concrete was also commonly used as the filling material to reinforce the strengths of thin-walled steel structures. Wang et al. [76] developed and validated an FE model to predict the behaviour of concrete filled steel tubular (CFST) members under lateral impact loads. Yousuf et al. [77, 78] conducted a similar research on the behaviour of concrete filled columns with and without axial pre-compressions. Alternatively, Yousuf et al. [77, 78] proposed and analysed stainless steel columns instead of steel columns. It was reported that the stainless steel specimens generally showed improved energy absorption performance compared with their mild steel counterparts, especially when concrete was used to fill the hollow tubes [77, 78]. Smith et al. [79] further contributed to this research topic by studying the response of braided stainless steel tubes filled with aluminium foam to lateral impact loads. Wang et al. [80] studied the behaviour of cement filled pipe-in-pipe structures under transverse impact. A similar conclusion was reached.

The carbon fibre reinforced polymer (CFRP) was initially utilized by Teng et al. [81] and Rizkalla et al. [82], for its high strength to weight ratio property. It has then attracted much interest on using such technique in infrastructural applications. In the past decade, although there was a considerable number of research on the CFRP technique, most of them focused on the CFRP strengthened structural members under axial impact loads [83-85]. The response of CFRP strengthened steel columns to lateral impact loads was firstly studied by Alam and Fawzia [86]. In [86], Alam and Fawzia used a numerical method to

predict the performance of steel columns with different wrapping schemes under combined axial compressive and lateral impact loads. They concluded that by applying CFRP strengthening to all four sides of columns, the lateral displacement at the impact zone can be reduced by approximately 42%, while the improvement was not very significant when the CFRP strengthening was applied on only two sides of columns [86]. Additionally, they emphasized the significance of boundary conditions, especially the level of axial compressive loads, on the failure mechanism [86]. Alam et al. [87] combined the design strategies of employing fillers and CFRP by investigating the behaviour of CFRP strengthened concrete-filled steel tubes subjected to lateral impact loads. Through a series of parametric studies, they pointed out the significance of the effective bond length to efficiently utilising CFRP [87].

In addition to the research topics aiming to improve the energy absorption performance under lateral impact loads, attention was also paid on the response of structural members under repeated lateral impact loads, which was less common found in reality. Cho et al. [88] used experimental and numerical methods to study the behaviour of steel beams under repeated lateral impact loads. Another focus of their study was the effects of sub-zero temperatures [88]. It was reported that sub-zero temperatures will reduce the permanent deflections. Demir et al. [89] investigated the behaviour of thin-walled tubes under repeated lateral impact loads. They assumed the thin-walled structure was filled with fluids and used the experimental method to assess the effects of the internal pressure and temperature [89].

2.3 The UltraSTEEL® dimpling cold-roll metal forming process

Dimpled steel sheets are cold-roll formed from plain steel sheets by the UltraSTEEL® process developed by Hadley Industries plc [90]. The concept of UltraSTEEL® was initially proposed and successfully utilized in early 1980s. The process uses a pair of rollers with rows of specially shaped teeth that form dimple shapes from both sides of plain sheets, as shown in Fig. 2.5 [91]. The dimpled sheets are then progressively fed into a series of rolls, arranged in tandem or by press braking, and formed into desired profiles. UltraSTEEL® dimpled products with various sectional profiles are shown in Fig. 2.6 [91]. Currently, the UltraSTEEL® dimpled products are extensively used in buildings, such as wall studs, roofing members, corrugated panels, windows and door reinforcement, etc. [92].

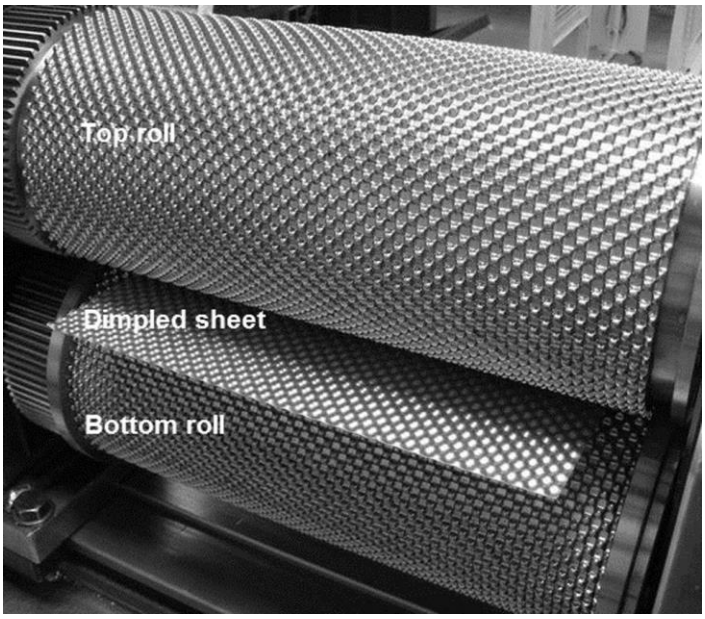

Fig. 2.5. The UltraSTEEL® forming process and dimpled steel sheet [91]

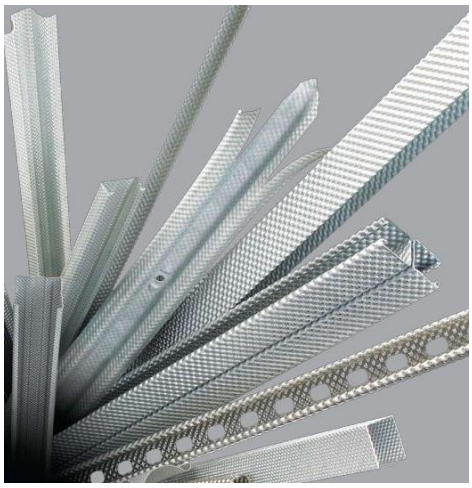

Fig. 2.6. UltraSTEEL® dimpled products with various sectional profiles [90]

The geometry of forming teeth has been optimized throughout the decades. Collins et al. [93] carried out a research to study the effects of tool design on the localised plastic deformation. Nguyen et al. [94] proposed an FE method to simulate the forming process. The FE model was based on a square shape plain steel sheet, where symmetric boundary conditions were applied and the rotational movement of the rollers were assumed to be vertical. Nguyen et al. [94] validated this FE model by comparing the experimental and numerical geometry of the dimpled sheets, and the engineering stress-strain curves. Nguyen et al. [91] then proposed a new FE model to simulate the UltraSTEEL® forming process and predict the resultant material properties more accurately. The new FE model was based on a full-scale model where a pair of quarter rollers was used [91]. Nguyen et al. [91] investigated the effects of parameters including mesh density, element type and loading step. It was revealed [91, 94] that non-uniform plastic deformation was developed during the forming process, which subsequently increased the yield and tensile strength of dimpled steel sheets.

The strength of the dimpled material was increased due to the work hardening developed during the forming process. The simplified FE model [94] and the full-scale FE model [91] are shown in Fig. 2.7.

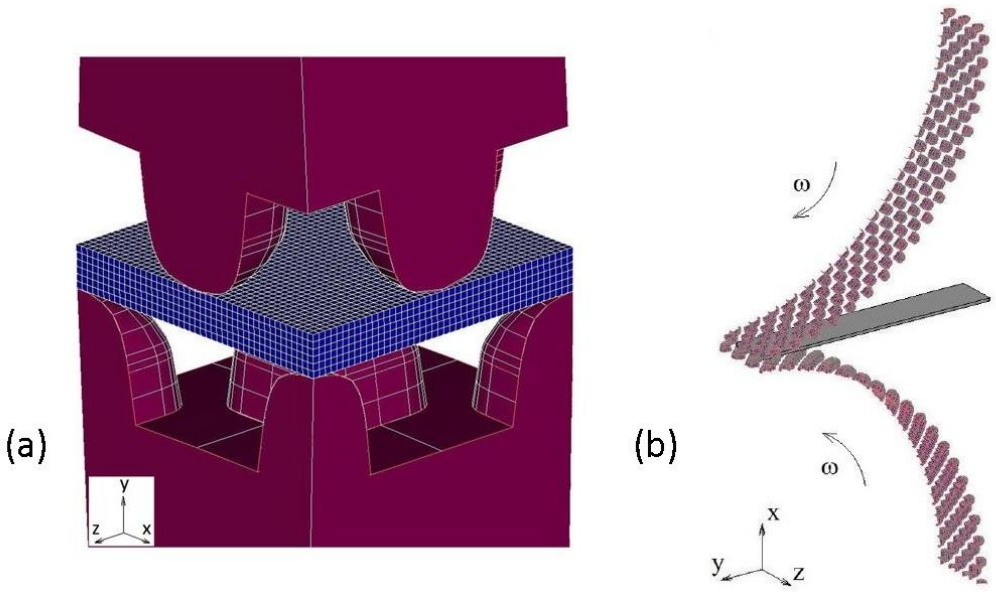

Fig. 2.7. (a) Simplified FE model [94] and (b) full-scale FE model [91]

Nguyen et al. [92, 95-97] performed a series of experimental tests and numerical simulations to compare the structural performance of plain and dimpled products originally from the same coil material. The tests included:

1. Tensile tests: It was reported that the yield and tensile strengths of the dimpled steel samples were 20.7% and 16.8% higher than the plain counterparts, mainly due to the hardening effect [95]. Additionally, it was pointed out that the dimpled samples lacked a yield plateau, which was due to the strain hardening generated [95].

2. Bending tests: The results of three-point bending tests revealed that the yield and ultimate loads were 23% and 21% greater in the dimpled samples when compared to the plain ones, respectively [95].
3. Compression tests: The compression tests on dimpled samples were firstly performed in [92]. Nguyen et al. [92, 95] used numerical and experimental methods to study the response of channel section plain and dimpled columns to quasi-static axial loads. A parametric study was conducted in the meantime to analyse the effects of the dimensions in the cross-sectional profile [92]. The results showed that the buckling and ultimate loads of the dimpled samples were 9-33% and 8-26% (depending on the dimensions) higher than the plain counterparts, respectively [92]. Nguyen et al. [94] then improved the design by introducing lips into the cross-sectional profile. When building the dimpled FE models in the compression tests in [92, 95, 96], Nguyen et al. employed a generic dimpled model and a generic corner dimpled model with shell elements, as shown in Fig. 2.8, for the purpose of reducing the computing time required. According to Nguyen et al. [92, 95, 96], those two generic FE models can be used to accurately predict the response of dimpled structural members under quasi-static loads.

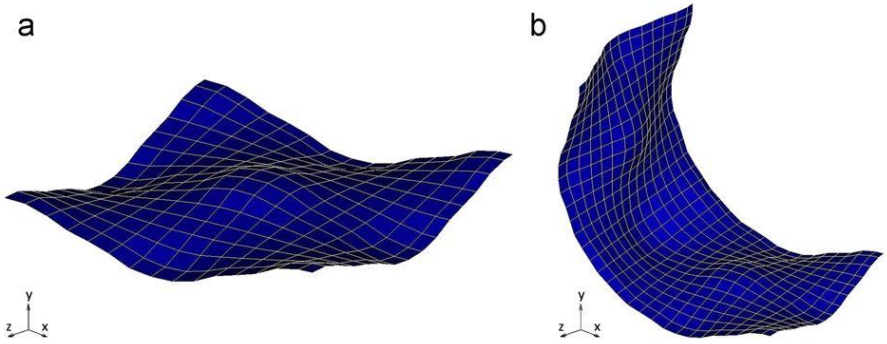

Fig. 2.8. (a) Generic dimpled FE model and (b) corner generic dimpled FE model with shell elements [96]

2.4 Explicit method for transient dynamics analysis

In the past decades, the explicit transient dynamics method has been successfully applied to simulate various types of non-linear transient dynamics problems [98]. This FE method is reported to be suitable for dealing with large deformation, large rotation, non-linear materials, contact, impact, etc. The essential difference between the explicit method and the implicit method is that the explicit method does not require to form the system stiffness matrix. Therefore, the explicit method can avoid some difficulties in non-linear problems because the large matrix does not need to be inverted [98]. The procedure of the explicit method can be summarised below [99]:

(1) Solution starts from the assigned material properties, loads, constraints and initial conditions.
(2) The deformation rate is determined based on the nodal displacements of a certain time step and the previous time step, which is subsequently used to determine the strain rates.
(3) The elemental stresses are updated based on the results from step (2) and the constitutive laws.
(4) The nodal forces are determined based on the results from step (3) and the externally applied loads.
(5) The nodal accelerations are derived.
(6) The nodal velocities are derived.
(7) The nodal displacements are updated based on the results from step (6).
(8) Go back to step (2), and repeat the cycles until the simulation is terminated.

Unlike the implicit method, in the explicit method, the nodal results at a specific step N are completely dependent on the nodal results at its previous step (N-1). Therefore, no iterations are needed when the time moves forward. Due to the nature of the explicit method that no iterations are involved, selecting an appropriate time step is crucial, as the mistakenly selected time step will result in errors in results. The principle of selecting a proper time step in an explicit dynamics analysis is that the stress wave must not travel through more than one element during one time step. Therefore, the specified time step must not be greater than the critical time step Δt_c, as defined in Eq. 2.13.

$$\Delta t_c = \min\{\frac{l}{c}\} \tag{2.13}$$

In Eq. 2.13, l represents the characteristic length of elements, and c refers to the sound speed in the material, which is dependent on the density, Young's modulus and Poisson's ratio of the material. For 4-node shell elements, which are the elements used in the present study, the characteristic length L is the shortest edge in an element, and the stress wave speed can be determined from Eq. 2.14 [100].

$$c = \sqrt{\frac{E}{\rho(1-\nu^2)}} \tag{2.14}$$

Therefore, by substituting Eq. 2.14 into Eq. 2.13, the critical time step in the present study can be calculated using Eq. 2.15, which implies that the critical time step is proportional to the minimum element size, assuming the mass scaling method is not adopted [101]. Additionally, a time step safety factor must also be specified when contact is involved in an explicit analysis, because the contact may be missed when the time step is inappropriately large [102].

$$\Delta t_c = \frac{L}{\sqrt{\frac{E}{\rho(1-\nu^2)}}} \tag{2.15}$$

2.5 Summary

In this chapter, the up-to-date research on the mechanisms and optimized designs of structural components under axial as well as lateral impact loads were reviewed. The previous research on the UltraSTEEL® dimpling metal forming process and the explicit Finite Element method were reviewed, too. Topics and key points covered in this chapter include:

- Mean crushing force, maximum crushing force, crush efficiency and specific energy absorption are the most commonly used variables to evaluate the energy absorption performance of structural components.
- The super folding element (SFE) theory is widely adopted to analytically predict the mean crushing forces of columns under axial impact loads.
- In recent decades, various types of designs were proposed and developed to improve the energy absorption performance of thin-walled structures. These designs may be generally categorized as using innovative cross-sectional profiles, high strength materials, and fillers.
- There is a particular interest in recent years in improving the resistance of structural members to lateral impact loads. Mainstream strategies include reinforcing the strengths of materials and employing various types of fillers.
- The UltraSTEEL® forming process can significantly increase the strengths of sheet metals, due to the work hardening developed throughout the forming process.

- The explicit transient dynamics FE method is suitable for dealing with dynamic events involving large non-linearity. However, due to the nature of this method, much attention must be paid when selecting time steps, which are dependent on the minimum element size, density, Young's modulus and Poisson's ratio of the material.

Chapter 3 Numerical modelling of the UltraSTEEL® dimpling forming process and determination of material properties

3.1 Introduction

As introduced in Chapter 2, The UltraSTEEL® dimpling forming process, developed by the Hadley group, changes the geometry and mechanical properties of the input plain steel sheets. The Hadley group is currently using this process to form dimpled sheets from 0.5 to 3 mm thickness gauges. The present study focuses on the 1 mm gauge UltraSTEEL® dimpling process, considering that vehicular structural components are the target applications.

In this chapter, the UltraSTEEL® dimpling forming process and the mechanical properties of dimpled steel sheets were studied. This chapter aims to establish and validate a finite element method to determine the geometry and material properties of various types of dimpled metal sheets, which will be used in later simulations. In this chapter, the UltraSTEEL® dimpling forming process and the subsequent tensile tests were simulated. The FE method was validated by comparing the numerical results with the experimental ones. The main objectives of this chapter are:

- Developing and validating an FE method that can be used to simulate the UltraSTEEL® forming process with different design parameters.

- Developing and validating an FE method to accurately simulate the tensile tests of plain and dimpled metal sheets.
- Obtaining the geometric models for the 1 mm gauge dimpled plates, which can be used in later simulations.
- Determining the mechanical properties for the 1mm gauge plain and dimpled plates through experimental tests.
- Comparing the mechanical properties of plain and dimpled steel sheets, and therefore understanding the effect of work hardening during the UltraSTEEL® forming process.
- Understanding the influence of using different element types in the tensile simulations.

3.2 Numerical simulation of the UltraSTEEL® forming process

The UltraSTEEL® forming process for 1 mm gauge plain galvanised steel sheets was simulated using ANSYS Mechanical APDL. The numerical results were validated by comparing to the experimental results.

3.2.1 FE modelling of the UltraSTEEL® forming process

The FE model was simplified by applying symmetric boundary conditions and the formation of only one dimple was simulated. Comparing to the full-scale simulation including the entire rollers and steel sheets (e.g. the FE simulation carried out by Nguyen et al. [94]), the advantages of this method are:

(1) The computational time is reduced.

(2) It is easy to assemble large FE models out of generic dimpled models.

The forming process was simulated based on a rectangular plain plate model. This is feasible because the tooth height is smaller than 1/25 of the roller radius. As illustrated in Fig. 3.1, the lengths along x-axis and z-axis of the model represent the circular bandwidth and axial pitch, respectively, and the dimension along y-axis of the plain plate represents the thickness of the input plate. The circular bandwidth is defined in Eq. 3.1, and the axial pitch refers to the horizontal separation between two adjacent teeth. The circular bandwidth and axial pitch are 6.4758 and 6.64 mm, respectively.

$$Circular\ bandwidth = (Roller\ radius + Tooth\ height) \times \frac{\tan(rotational\ pitch)}{2} \quad (3.1)$$

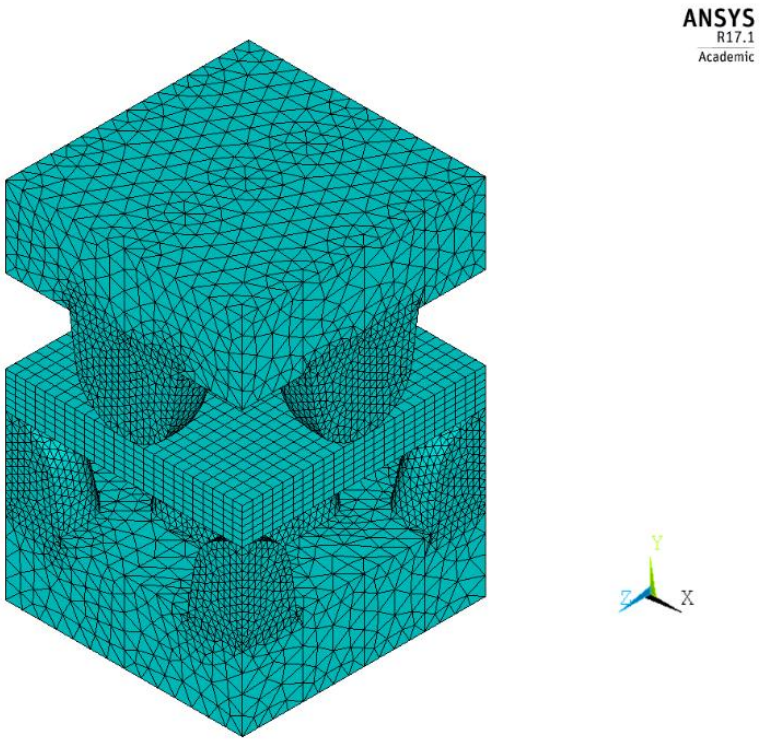

Fig. 3.1. FE model of the UltraSTEEL® forming process

In the simulation, the translational displacements of all the nodes on the side surfaces were constrained in x and z directions, while the translational displacements of all other nodes were free in all DOFs. A displacement of 0.53mm along –y direction was applied to the base of the top teeth and a displacement of 0.53mm along +y direction was applied to the base of the bottom teeth. The value was selected to ensure that the overall thickness after the forming process equals to twice of the gauge thickness, which is currently the manufacturing standard adopted by Hadley group.

ANSYS solid45 4-node elements were used to mesh the forming teeth, and solid45 8-node elements were used to mesh the plain plate. Mapped mesh with 24 divisions along the x direction, 6 divisions along the y direction and 24 divisions along the z direction was adopted, based on an element size sensitivity study. ANSYS contact 173 and target 170 elements were used to deal with the contact between forming teeth and the plate. A Coulomb friction coefficient of 0.3 was used in the simulation.

Because nonlinearity was involved in this case, true stress and strain as defined in Eq. 3.2 were employed to describe the material properties. For the plain plate, the piecewise linear true stress-strain relation was used to describe the mechanical properties, as shown in Fig. 3.2. The data was obtained from quasi-static tensile tests, which are introduced in Section 3.3. For the forming teeth, the bi-linear stress-strain relation was used.

$$\sigma_{true} = \sigma_{eng}(1 + \varepsilon_{eng}) \tag{3.2a}$$

$$\varepsilon_{true} = \ln(1 + \varepsilon_{eng}) - {}^{\sigma_{eng}}/_{E} \tag{3.2b}$$

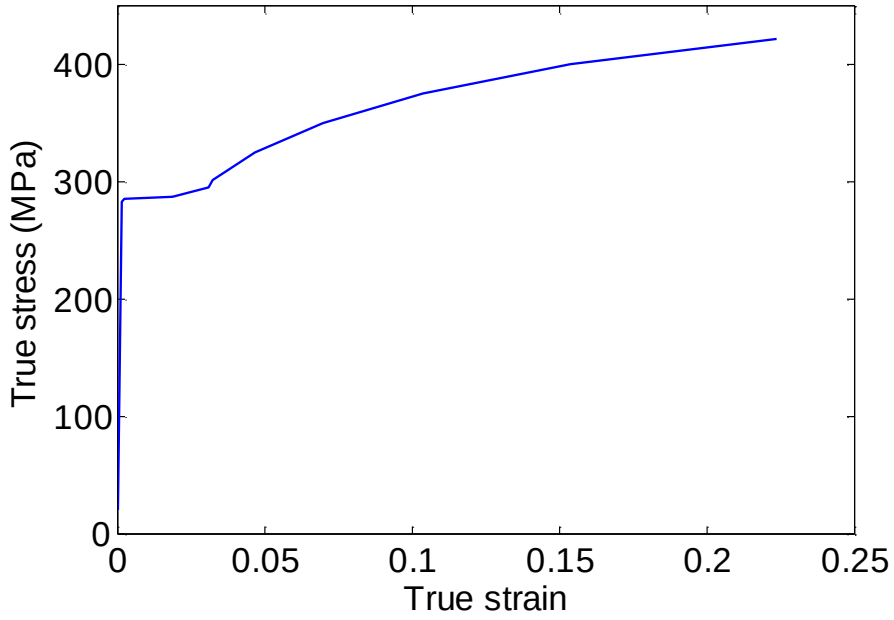

Fig. 3.2. Input piecewise linear true stress-strain relation of the plain steel plates

3.2.2. Numerical results of the UltraSTEEL® forming process and validation

The simulation was validated by comparing the numerical deformed shape with the experimental one. After the forming process, the local thickness was not uniform throughout the dimpled plate. The numerical and experimental cross-sectional areas of the dimpled plates are compared in Fig. 3.3. The local thickness reaches its maximum value at the slope region and minimum value at the peak region. The numerical and experimental thicknesses at the peak and slope regions are listed in Table 3.1. It was noted that the errors are less than 2%. Therefore, the geometrical change due to the forming process can be considered to be accurately simulated.

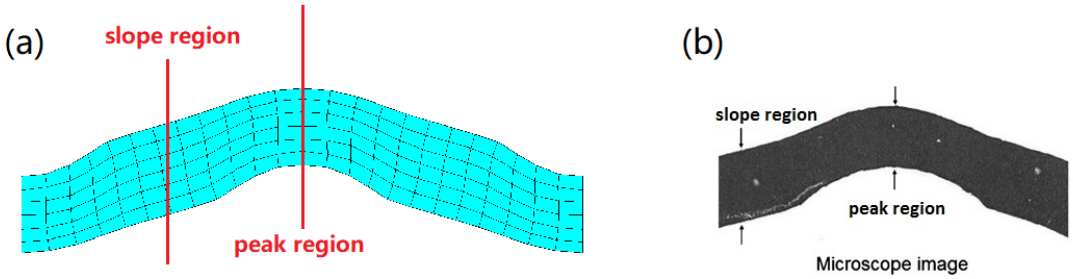

Fig. 3.3. (a) Numerical and (b) experimental cross-sectional areas after the UltraSTEEL® forming process

Table 3.1. Numerical and experimental thicknesses of the dimpled plate

	FE (mm)	EXP (mm)	Error
Peak region	0.861	0.844	2.0%
Slope region	0.989	0.989	0

3.3 Quasi-static tensile tests

Quasi-static tensile tests were carried out to determine the mechanical properties of plain and dimpled materials. Seven samples of each material were tested.

3.3.1 Test procedure

The plain and dimpled samples used in the quasi-static tensile tests were prepared according to the British Standard BS EN 10002-1:2001. All the samples originated from the same coil 1 mm gauge thickness material. The ‘dog bone’

shape samples were cut from large plain and dimpled plates, using the wire cutting technique. The plain and dimpled samples are shown in Fig. 3.4(a), and the dimensions of the samples are shown in Fig. 3.4(b). As shown in Fig. 3.4(b), the overall length is 200 mm, the parallel part has a length of 75 mm and width of 12.5 mm. The dimensions of all samples were measured prior to testing. For plain samples, the initial cross-sectional area was calculated based on the thickness and width, which were measured using a micrometre and a vernier calliper. For dimpled samples, the initial cross-sectional areas at three positions along the samples were measured using a microscope, and the average value was considered to be the initial cross-sectional area.

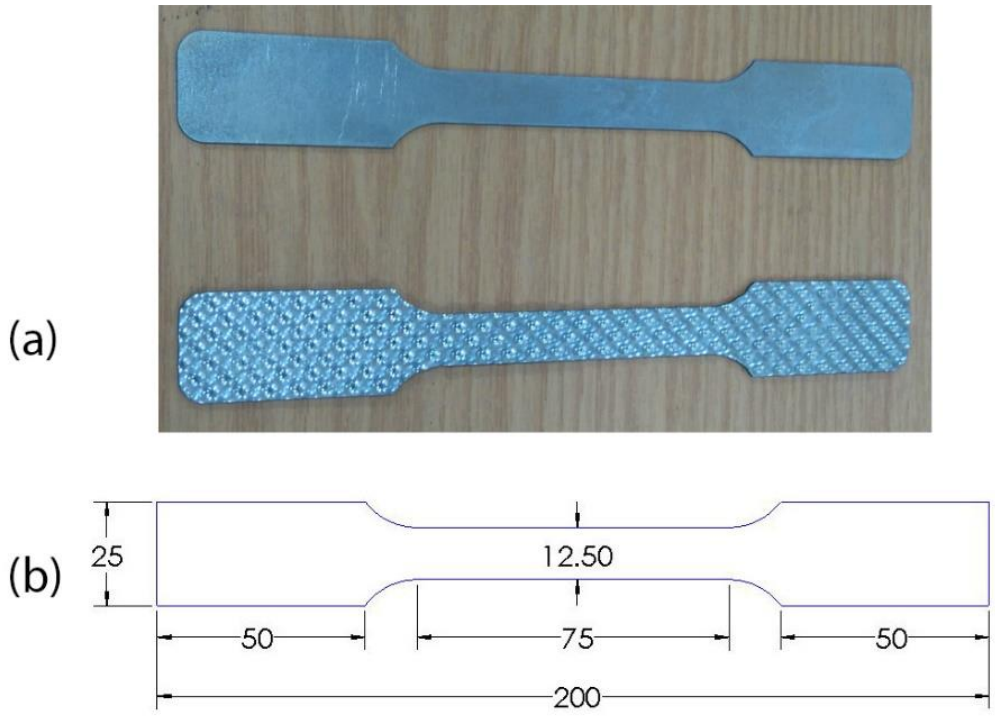

Fig. 3.4. (a) Samples and (b) dimensions of the samples used in the quasi-static tensile tests

In the tests, grip was applied on two sides of the samples to ensure only the parallel parts were stretched. A constant displacement rate of 2.5 mm/min was applied throughout the testing till the samples failed. The displacement rate resulted in an engineering strain rate of approximately 5.6×10^{-4} s^{-1}, to ensure that the effect of strain rate was negligible. Force and axial displacement were measured with a sampling frequency of 3.3 Hz.

3.3.2 Test results

Engineering stress and strain were calculated based on the measured forces, axial displacements and initial cross-sectional areas of the samples. The results are displayed in Table 3.2 and Fig. 3.5. Yield strengths were obtained using the standard offset method at a strain level of 0.2%. Average yield and ultimate strengths were determined based on the experimental results for all the samples. It was found that the average yield and ultimate strengths of the dimpled samples were 25.4% and 9.3% higher than those of the plain samples, respectively.

Table 3.2. Summary of quasi-static tensile test results

	Yield strength (MPa)				**Ultimate strength (MPa)**			
	Average	Standard deviation	Max. value	Min. value	Average	Standard deviation	Max. value	Min. value
Plain	276	4.02	281	272	368	2.09	371	364
Dimpled	346	4.57	351	342	399	2.44	402	396

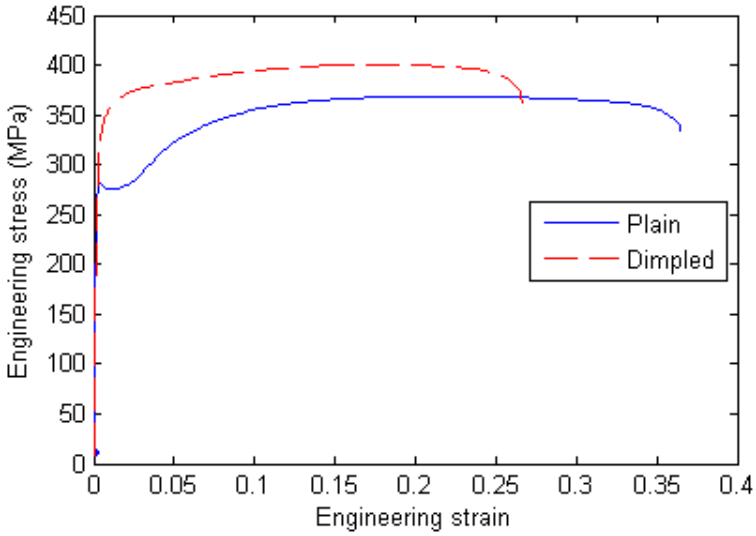

Fig. 3.5. Engineering quasi-static stress-strain curves of plain and dimpled materials

The true stress-strain relations were derived using Eq. 3.2, and then converted to the exponent format, as shown in Eq. 3.3a. The purpose is to determine the input parameters for the simulations in Chapters 4 to 7. Eq. 3.3a was re-arranged to the form of Eq. 3.3b. The strain hardening constant B and the strain hardening exponent n were determined through the linear fitting of $\log(\sigma - \sigma_y) - \log(\varepsilon_{pl})$ curves, which are shown in Figs. 3.6. and 3.7. In those two figures, the strain hardening exponent n is represented by the slope and $\log(B)$ is represented by the intercept with vertical axis. Values of B and n are shown in Table 3.3.

$$\sigma = \sigma_y + B{\varepsilon_{pl}}^n \tag{3.3a}$$

$$\log(\sigma - \sigma_y) = log(B) + nlog(\varepsilon_{pl}) \tag{3.3b}$$

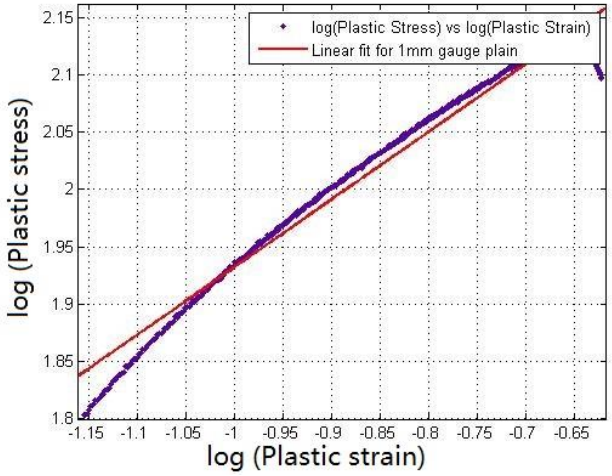

Fig. 3.6. Linear fit of $\log(\sigma - \sigma_y) - log(\varepsilon_{pl})$ for plain steel sheet

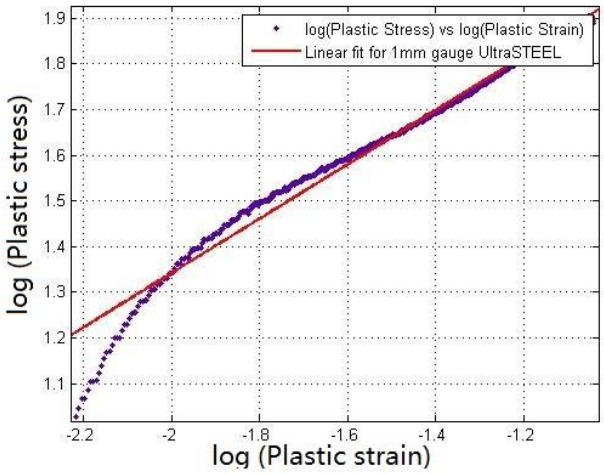

Fig. 3.7. Linear fit of $\log(\sigma - \sigma_y) - log(\varepsilon_{pl})$ for dimpled steel sheet

Table 3.3. Strain hardening coefficients for plain and dimpled materials

	Plain	**Dimpled**
Strain hardening constant B	378 MPa	383 MPa
Strain hardening exponent n	0.6018	0.6036

3.4 Numerical simulation of the tensile tests on dimpled samples

The tensile tests on the dimpled samples introduced in Section 3.3 were simulated, using three different modelling methods. Key features of these three models are:

(1) Solid elements and non-uniform material properties.

(2) Solid elements and uniform material properties.

(3) Shell elements and uniform material properties.

3.4.1 FE modelling

In the actual tensile tests, the load was applied across the entire cross section of the sample, at a constant axial velocity. Additionally, it was considered that only the parallel parts of the ‘dog bone’ samples were stretched. Therefore, symmetric boundary conditions were applied and the FE model was simplified down to the size of only one dimple, as shown in Fig. 3.8. ANSYS solid45 elements were used to model the dimpled plate, with the same mesh density as introduced in section 3.2.1. Symmetric boundary conditions in x-direction were applied on face B and its opposite face. Displacement along z-axis was restrained for all the nodes on the opposite face of face A. Displacement along y-axis was restrained for node 1 to prevent the plate from moving as a rigid body along y-axis. Displacement along x-axis was restrained for all the nodes on the mid-plane between face B and its opposite face, to prevent the plate from moving as a rigid body along x-axis. A

uniform displacement of 0.8 mm in z-direction was applied to all the nodes on face A, representing the tensile loading conditions applied in reality.

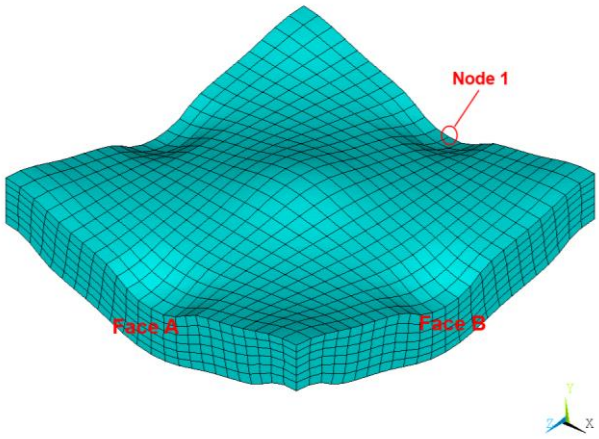

Fig. 3.8. Dimpled FE model (with solid elements) of the tensile tests

In the model with solid elements, there are six layers of elements and seven layers of nodes throughout the thickness. To create the model with shell elements, the coordinates of the mid-layer nodes of the solid element model were exported. ANSYS shell181 elements with 5 integration points throughout the thickness were used. All the shell elements had a uniform thickness of 0.959 mm and an element size of 0.275 mm. The model with shell elements is shown in Fig. 3.9. Boundary conditions applied were the same as on the solid element model.

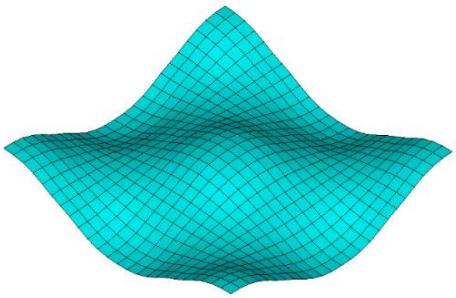

Fig. 3.9. Dimpled FE model (with shell elements) of the tensile tests

During the UltraSTEEL® forming process, work hardening was developed to different extents across the plate, which means the mechanical properties of local regions are not identical. The effect of residual stress after the forming process was taken into account in one of the solid element models. The total 3456 elements were divided into seven segments, based on the local von-Mises stress after being formed. Seven different stress-strain relations were then assigned to the elements accordingly. The seven materials have true yielding strengths of 278, 295, 320, 345, 370, 395, 415 MPa, respectively. The post-yield stress-strain relations remained unchanged. Elements with each mechanical properties are shown in Fig. 3.10.

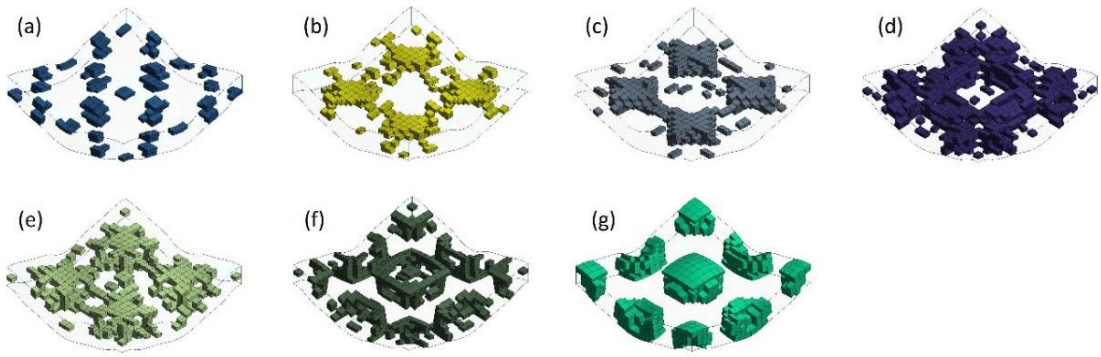

Fig. 3.10. Elements with true yield strengths of (a) 278, (b) 295, (c) 320, (d) 345, (e) 370, (f) 395 and (g) 415 MPa

3.4.2 Results and discussions

The numerical deformed shape under the tensile load is shown in Fig. 3.11, where the white dotted line represents the original un-deformed shape. When processing results, the displacements and the sum of nodal forces along z-axis of all the nodes on face A were exported at each solving step. Engineering stress

and strain were then calculated based on the exported data. The numerical stress-strain curves for plain and dimpled plates are shown in Fig. 3.12. The numerical results reveal that the yield strengths of the plain and dimpled samples are 277 and 349 MPa, respectively. The errors comparing to experimental results are less than 1%, which can be neglected. Therefore, the numerical method used to simulate the UltraSTEEL® dimpling forming process and the tensile tests was validated.

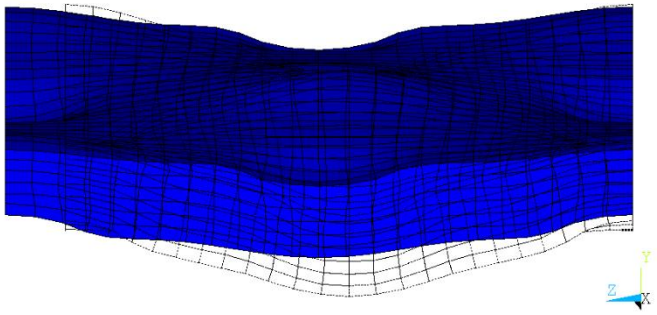

Fig. 3.11. Deformed shape of the dimpled plate under tensile loading

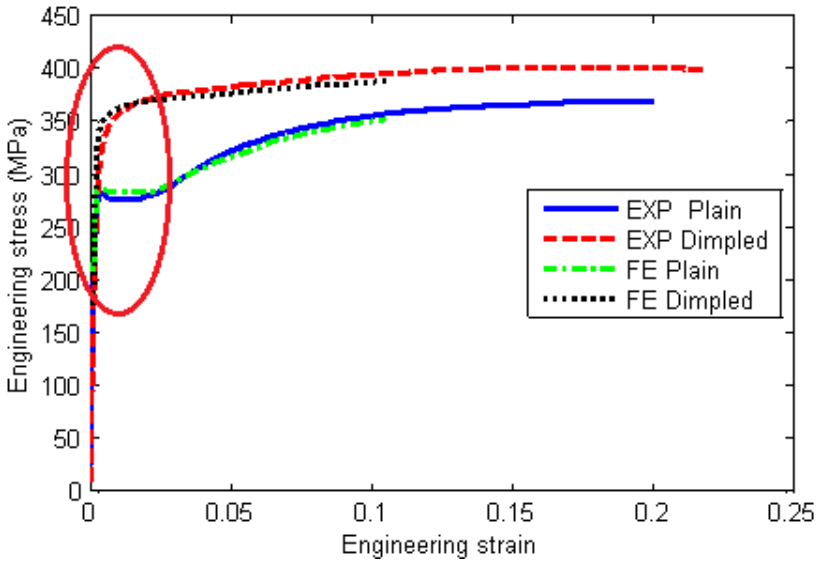

Fig. 3.12. Experimental and numerical engineering stress-strain curves

Additionally, it was found that in both experimental tests and numerical simulations, the dimpled samples show a smoother transition from the elastic region to the plastic region, as highlighted in Fig. 3.12. It is due to the fact that the local strains in the plain plate are identical across the sample, therefore all the elements enter the plastic region simultaneously. By contrast, the local strains in the dimpled plate are different under tensile loads, as shown in Fig. 3.13. Therefore, the elements progressively enter the plastic region. This is one of the effects of the dimpled geometry on the mechanical behaviour. The other effects are studied in Chapter 5.

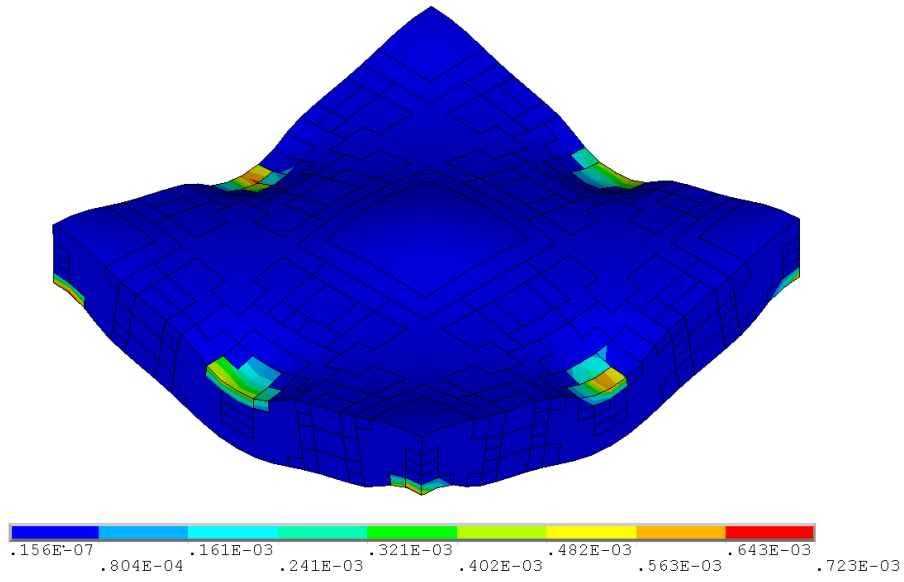

Fig. 3.13. Equivalent plastic strain in the dimpled plate under tensile loading

Theoretically, the FE model with solid elements and non-uniform material properties will provide the most accurate results, because the geometry and residual stress have been fully taken into account. However, when simulating dynamic events (e.g. simulations in Chapters 4 to 7), it is impractical to use solid

elements and non-uniform material properties, due to the constraint of computational resources. Therefore, shell elements with uniform material properties were used. It can be considered as a two-stage simplification. The first stage is to apply homogeneous material properties while still using solid elements, which means the effect of non-uniform work is neglected. The second stage is to replace the solid elements by shell elements, which means the stress distribution throughout thickness and the slightly varying thickness across the dimpled plate are neglected. In the second stage, the equivalent thickness was determined, based on the conservation of mass. The comparison among the three FE models and experimental results are shown in Fig. 3.14. It shows that the error after the two-stage simplification can be neglected. To be more specific, at the yielding point and when the strain was 0.05, the difference between the FE model with shell elements and the experimental results in stress are 0.6% and 2.7%, respectively.

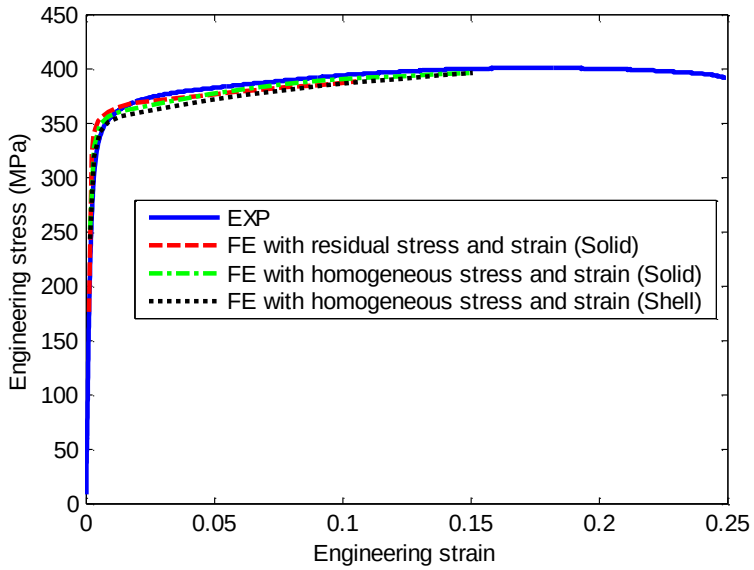

Fig. 3.14. Experimental and numerical stress-strain curves with different FE models

3.5 Integrated FE analysis of forming process and tensile test

In the UltraSTEEL® forming process, residual stress and strain will develop and slightly change after the forming teeth being retreated. Theoretically, this will influence the properties of the dimpled steel sheets. This section focuses on the effects of the generation and release of residual stress and strain.

To take the generation and release of residual stress and strain into account, the forming, releasing, and tensile processes were reproduced in only one simulation, using ANSYS Mechanical APDL. The FE model is shown in Fig. 3.15. All the details except for boundary conditions are identical to those in section 3.2.1. In terms of boundary conditions, this integrated quasi-static simulation involves three load steps. Fig. 3.16 shows the original shape and the deformed shapes at the end of each load step, which helps explain the three stages of the FE simulation.

(1) Forming: In load step 1, the boundary conditions are the same as described in section 3.2.1.

(2) Retreating forming teeth: In load step 2, the displacements for upper and lower forming teeth are changed to 2 mm along –y and +y directions, respectively. All the rest boundary conditions remain unchanged.

(3) Applying tensile load: The DOF restrained on faces A, B and their opposite faces are removed. Faces B and its opposite face are defined to be symmetric in x-axis. DOF in x-axis equals to zero for all nodes on the mid-plane between face B and its opposite face. DOF in z-axis equals to zero

for all nodes on the opposite face of face A. Displacement in z-axis of all the nodes on face A equals to 0.8 mm.

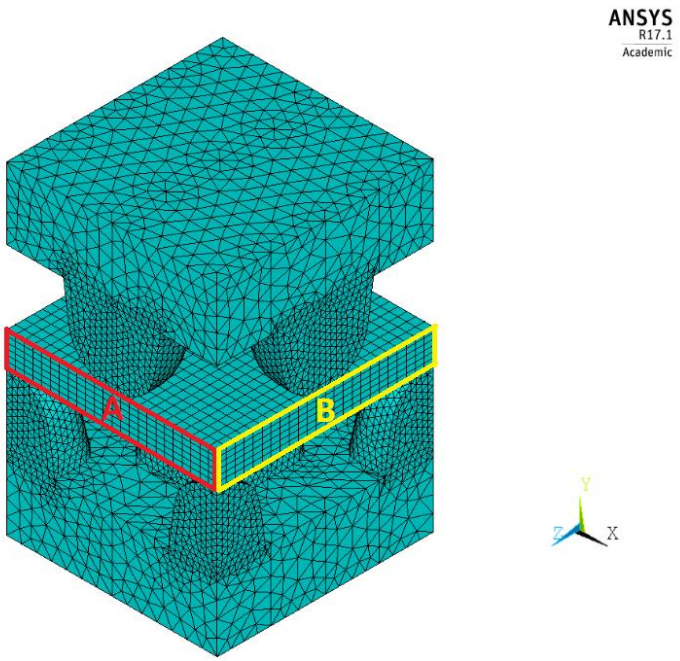

Fig. 3.15. FE model of the integrated forming process and tensile test

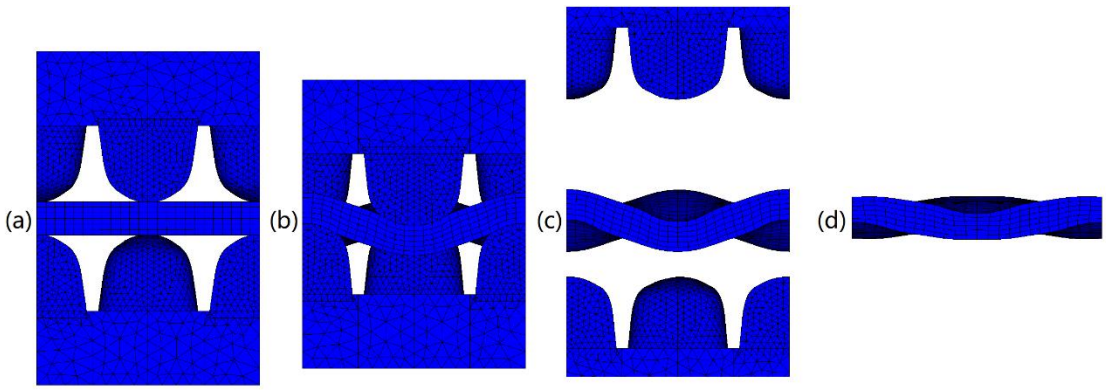

Fig. 3.16. Deformed shapes at the end of (a) original shape, (b) load step 1, (c) load step 2 and (d) load step 3

In terms of the mechanical properties of dimpled steel sheets, three engineering stress-strain relations of dimpled steel sheets are shown in Fig. 3.17. A very good

agreement is observed among the results obtained from experimental tests and two different FE approaches. Therefore, it is found that both FE approaches can accurately predict the mechanical properties of dimpled steel sheets.

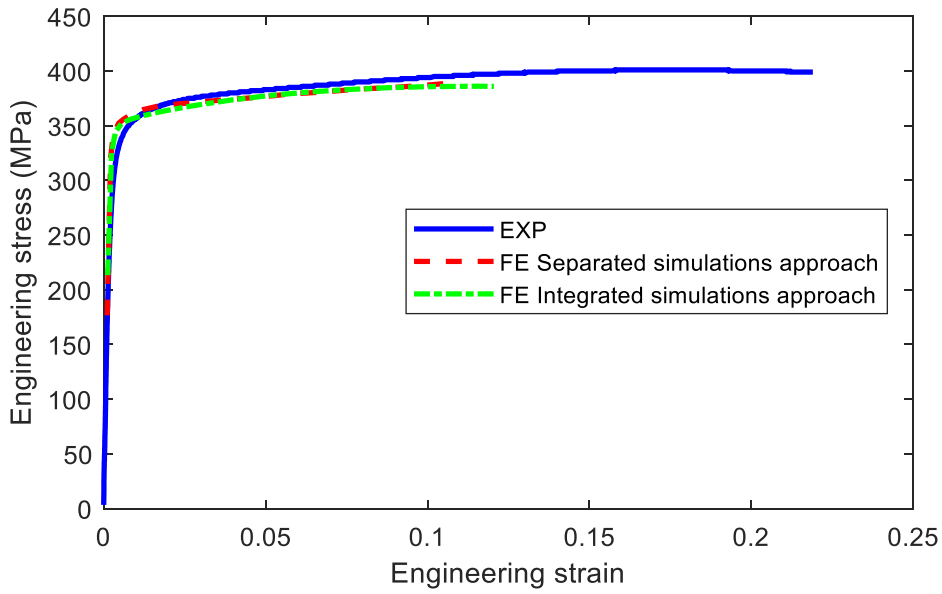

Fig. 3.17. Engineering stress – strain curves obtained from experiments and different numerical approaches

3.6 Summary

In this chapter, the UltraSTEEL® dimpling forming process was simulated on a simplified model of a rectangular plain plate. Experimental quasi-static tensile tests for plain and dimpled materials were conducted. The tensile tests were then simulated using the FE method. Comparisons in terms of mechanical properties have been made between the plain and dimpled samples, experimental and numerical results, and numerical results obtained through different approaches. The following conclusions can be made from the study:

- An FE model was developed to simulate the UltraSTEEL® forming process. Boundary conditions were applied to simplify the model and simulation. The dimpled geometry was obtained using this numerical method, and the geometry agreed very well with the experimental one.
- Experimental quasi-static tensile tests show that the engineering yield and ultimate strengths of the dimpled samples are 25.4% and 9.3% higher than the plain samples, which are originated from the same coil of material. True stress-strain relations for the plain and dimpled materials were determined from the experimental results, and the true stress-strain relations were then normalized to the exponent format.
- An FE model was developed to simulate the quasi-static tensile tests. The numerical results agreed very well with the experimental results. Therefore, this FE model was validated. The tensile simulations reveal that due to the dimpled geometry, the local stress and strain are not uniformly developed in dimpled plates under tensile loads, which can subsequently result in a smoother transition from the elastic region to the plastic region, when subjected to tensile loads.
- The FE model of dimpled plates was simplified by assuming homogeneous local material properties and utilizing shell elements. Results reveal that the effects of these simplifications can be neglected.

Chapter 4 Experimental and numerical study of the response of open section columns to axial crushing loads

4.1 Introduction

As introduced in Chapter 1, this project aims to investigate the energy absorption performance of dimpled structures, mainly using the explicit dynamics finite element method. It requires validation to use the explicit dynamics FE method to predict the response of dimpled columns to impact loads. Experimental tests and numerical simulations were carried out, aiming to validate the FE method. The author designed the test procedure, processed the experimental data, and selected all the testing parameters based on the availability of facilities and samples. The practical work (e.g. connecting the data acquisition system, fitting the samples and operating the facilities) was carried out by local technicians. The axial crushing loading type was selected because it is one of the most typical loading types that thin-walled structures are designed to withstand. In the experimental and numerical analysis, two types of loads were applied: dynamic and quasi-static loads. The objectives of this chapter are:

- Developing and validating an FE method to simulate the dynamic and quasi-static crushing events of dimpled thin-walled structural components.
- Understanding the failure mechanism of open section plain and dimpled thin-walled columns under dynamic axial crushing loads.

- Understanding the failure mechanism of open section plain and dimpled thin-walled columns under quasi-static axial crushing loads.
- Evaluating the energy absorption performance of dimpled columns by comparing to their original plain counterparts.
- Understanding the significance of the strain rate sensitivity of materials, and selecting an appropriate mathematical model and governing coefficients to accurately represent the strain rate effect.

4.2 Response of open section columns to dynamic axial crushing loads

4.2.1 Experimental tests

The dynamic crushing tests were conducted at the Warwick Manufacturing Group (WMG). A total number of 20 tests (excluding the trial tests) were conducted on plain and dimpled samples under 2 different impact energies.

4.2.1.1 Test procedure

The dynamic crushing tests were performed using the INSTRON 9250 drop hammer test machine, as shown in Fig. 4.1. The schematic plot of the experimental setup is shown in Fig. 4.2. The test machine was connected to a computer control and a data acquisition system. Data acquired included instantaneous forces and axial displacements at a sampling frequency of 80 kHz, and videos taken at 12,500 fps. The duration of recording was set as 100 ms. A

sensor was fitted to activate the recording approximately 10% prior to the start of impact, in order to ensure the initial peak force was not missed. Buffers were fitted below the support plate in order to protect the equipment, and the buffers can absorb up to 500 J energy. The mass of the impactor was 168.5 kg, including all the accessories. Two springs were fitted at the top of the test machine. In the experiments, the impactor was raised to a specific height, and the kinetic energy of the impactor was converted from gravitational potential energy and the elastic energy of the compressed springs. Two impact velocities were selected, based on the results of trial tests. The principles of selecting impact energies were to ensure that at least two folds of layers can be formed, while not damaging the equipment. Impact velocities of 3.44 and 4.33 m/s were selected. Therefore, the two impact energies were 997 J and 1580 J.

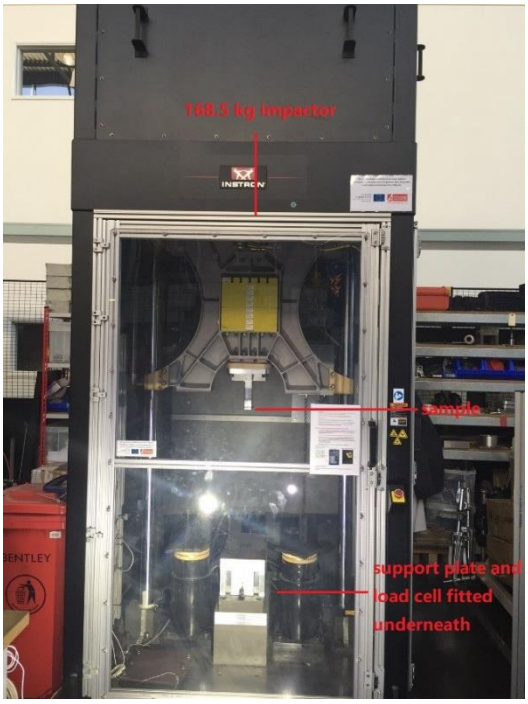

Fig. 4.1. INSTRON model 9250 drop hammer test machine

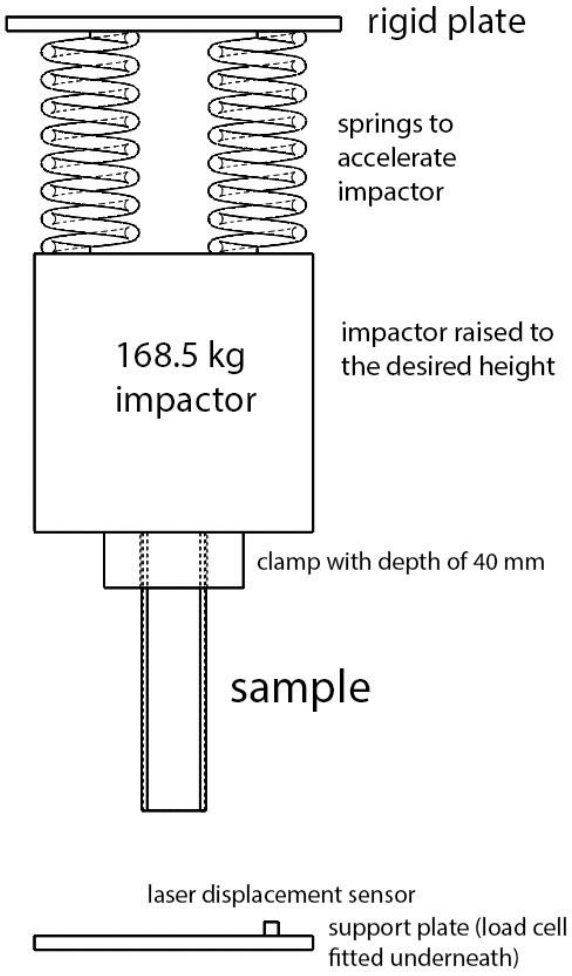

Fig. 4.2. Schematic plot of the test system

The specimens were made of plain and dimpled galvanised steel, as shown in Fig. 4.3(a). All the specimens were originated from the same coil of material. Profile 5082 samples from Hadley group were used in the tests, due to its availability. The cross-sectional profile was shown in Fig. 4.3(b), where the gap size d_3 was controlled to be between 1 and 3 mm. The specimens were 200 mm long and fixed at one end by clamps with a depth of 40 mm (i.e. the effective axial length was 200-40=160 mm), as shown in Fig. 4.4. Triggers highlighted in Fig. 4.4 were applied on the samples subjected to the 1580 J impact energy. The

reasons are explained in Section 4.2.1.2. The gauge thickness of all samples is 1 mm.

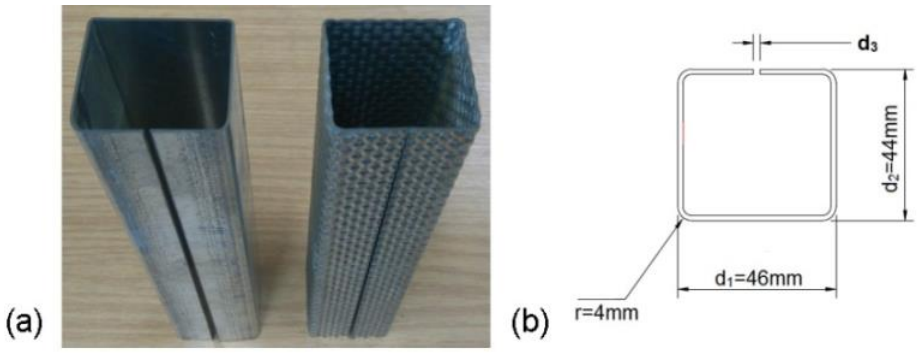

Fig. 4.3. (a) Plain and dimpled samples and (b) cross-sectional profile of the samples

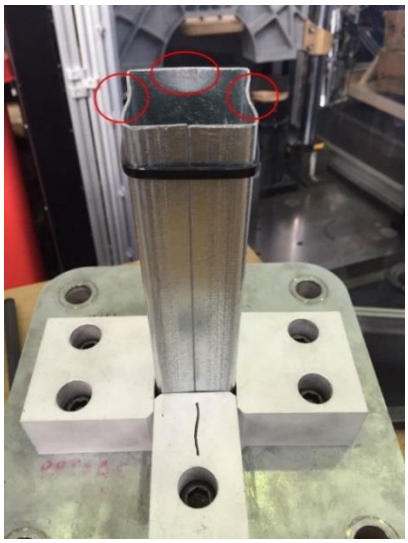

Fig. 4.4. Fixture of samples in the dynamic crushing tests

The material properties of plain and dimpled steel materials were determined from quasi-static tensile tests introduced in Chapter 3. Detailed information on the materials' mechanical properties are presented in Fig. 3.5 and Table 3.2. Specimens prepared using the wire-cut as well as the band saw-cut techniques were tested in the trial runs. However, only the band saw-cut specimens were

used in the formal tests. Reasons and discussions are presented in Section 4.2.1.2.

4.2.1.2 Test results and discussions

In the experiments, the tests were repeated for five times under each condition. The typical crushing force - axial displacement curves and the deformed shapes are shown in Figs. 4.5 to 4.8. During the crushing process, the 40 mm deep clamps prevented the flanges from folding outwards. Therefore, the folding mechanism of the tested open section specimens were very similar to the closed square section columns, which was comprehensively studied by Wierzbecki et al. and introduced in Chapter 2. To prepare the crushing force - axial displacement curves, a Savitzky-Golay filter was applied to the raw data to eliminate the effect of noise, as the recorded data were in the time domain. For each data set, the span was set as the nearest odd number to 1/5 of the total number of data points, while the polynomial fitting degree was set as 4.

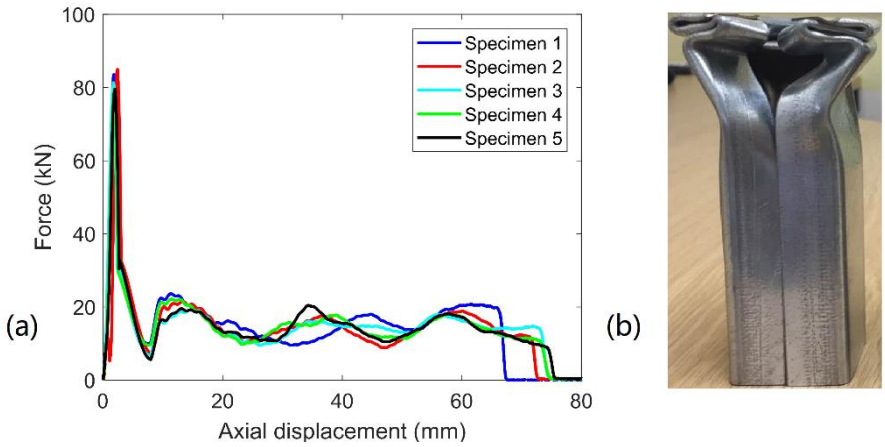

Fig. 4.5. (a) Force - displacement curve and (b) deformed shape of the plain sample under 3.44 m/s impact velocity

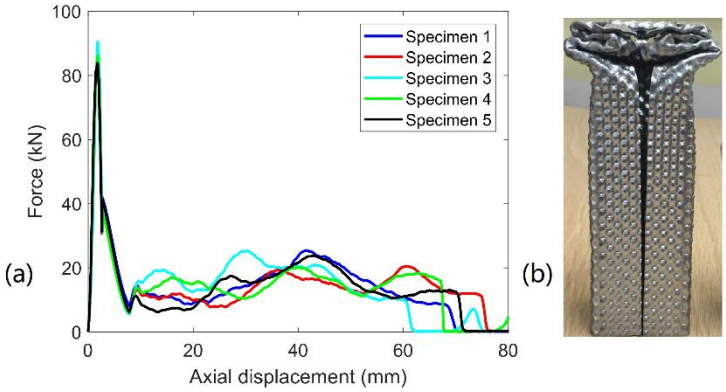

Fig. 4.6. (a) Force - displacement curve and (b) deformed shape of the dimpled sample under 3.44 m/s impact velocity

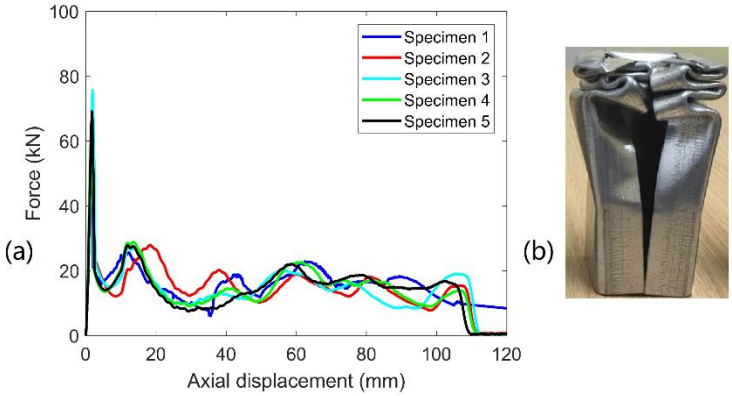

Fig. 4.7. (a) Force - displacement curve and (b) deformed shape of the plain sample under 4.33 m/s impact velocity

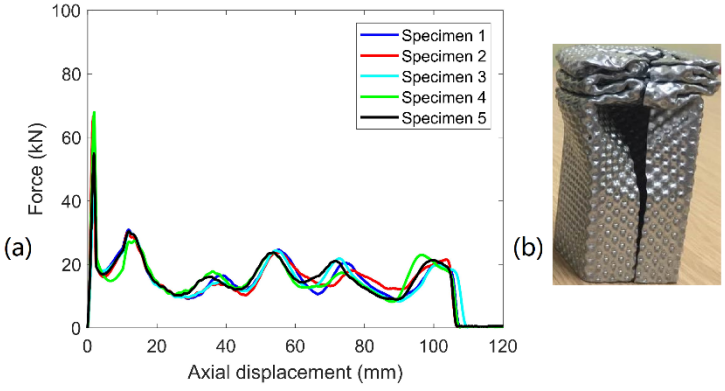

Fig. 4.8. (a) Force - displacement curve and (b) deformed shape of the dimpled sample under 4.33 m/s impact velocity

As introduced in Chapter 2, the primary variable used to evaluate a structure's energy absorption efficiency is specific energy absorption (SEA). SEA is defined in Eq. 4.1, where EA represents the Energy Absorbed.

$$SEA = \frac{Total\ EA}{Mass\ of\ deflected\ column} \tag{4.1}$$

The SEA value can be determined based on the gradients of the EA - axial displacement curves. In the experimental tests, instantaneous velocities and axial displacements of the impactor were measured. Therefore, the energy absorbed can be calculated from Eq. 4.2.

$$EA = mg\delta + \frac{1}{2}m({v_i}^2 - v^2) \tag{4.2}$$

Where m is impactor mass, δ is instantaneous axial displacement of the column's free end, v_i is impact velocity, and v is instantaneous velocity. An example of obtained EA - axial displacement curves is shown in Fig. 4.9. Linear fitting has been performed to determine the gradient.

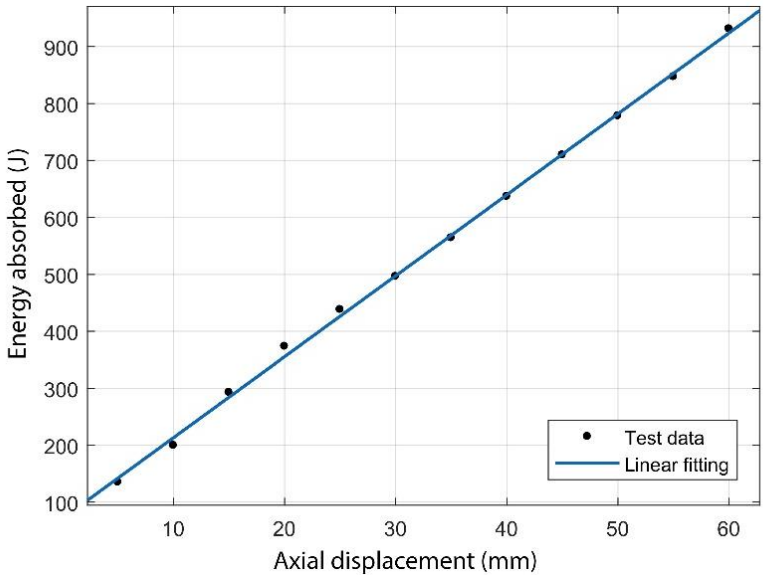

Fig. 4.9. An example of linear fitting for EA - axial displacement curves

Using the method described above, SEA values for all four test groups were determined and presented in Fig. 4.10. Based on the number of tests and distribution of results, median values were used. The median values are represented by the red bars in Fig. 4.10, and listed in Table 4.1.

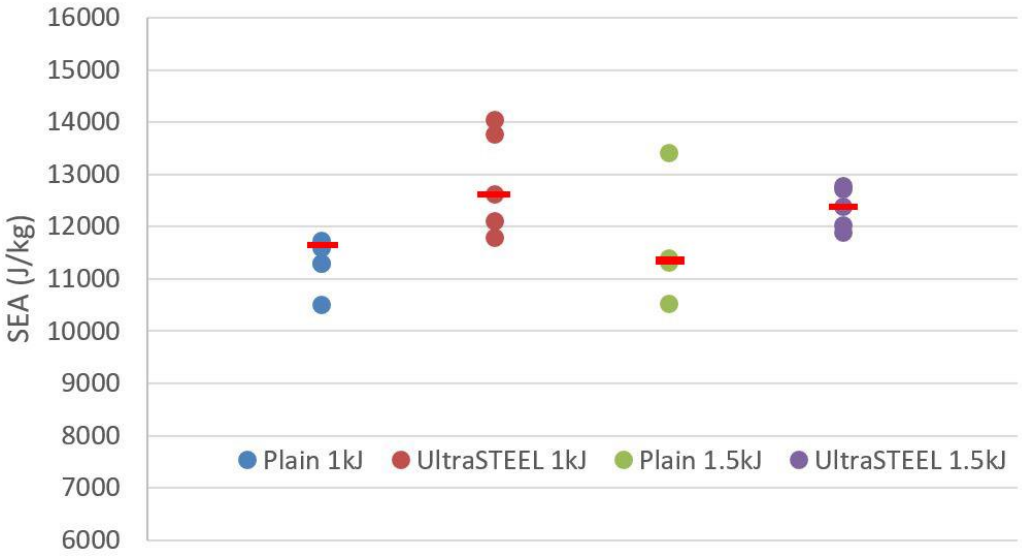

Fig. 4.10. Dynamic crushing experimental test results

Table 4.1. Dynamic crushing experimental test results

Test condition	Material	Impact energy (J)	Impact velocity (m/s)	SEA (J/kg)
1	Plain	997	3.44	11437
2	Dimpled	997	3.44	12628
3	Plain	1580	4.33	11351
4	Dimpled	1580	4.33	12376

For the 1580 J impact energy test groups, because initiators have been introduced, SEA for both plain and dimpled samples are slightly lower than the 997 J impact energy test groups. However, the difference between dimpled and

plain samples in SEA is hardly influenced by either impact energy or the use of initiators. Comparing to the plain columns, SEA of the dimpled columns are 10.40% and 9.02% higher when impact energies are 997 J and 1580 J, respectively.

In addition to the above tests, trial tests were performed to determine the loading conditions and the suitable manufacturing technique to prepare samples. The trial test results have revealed the effect of the columns' inherent imperfections. In the trial tests, both wire-cut and band saw-cut samples were crushed under the impact velocity of 3.44 m/s. As shown in Fig. 4.11(a), the wire-cut samples have smoother cross-sectional surfaces and the cross-sectional surface is almost perfectly perpendicular to the longitudinal direction. At the instant that contact begins, the entire end surface of the wire-cut samples is touching the impact face, and the column is almost perfectly perpendicular to the impact face. These two facts will prevent the edges from folding in or out. Instead, the wire-cut samples tend to start buckling at a random location. An example of the crushed wire-cut samples is shown in Fig. 4.11(b). This failure mechanism has made the subsequent crushing behaviour unpredictable. By contrast, the imperfection in the band saw-cut samples is more significant, as shown in Fig. 4.12(a). The inherent imperfection helps initiate the crushing process from the column ends. An example of the crushed band saw-cut samples is shown in Fig. 4.12(b). Therefore, band saw-cut samples were used in the formal tests, to eliminate the uncertainty in the columns' failure modes.

However, the inherent imperfection is not always sufficient to initiate the first fold, especially when the impact velocity is high. As the impact velocity increasing, the

effect of imperfection becomes less significant. Repeated trial tests indicated that the inherent imperfection of the band saw-cut samples was sufficient under the impact velocity of 3.44 m/s. When the impact velocity was increased to 4.33 m/s, the columns started to buckle from mid-point due to the insufficient inherent imperfection, as shown in Fig. 4.13. Therefore, to compensate, initiators were employed in the 4.33 m/s tests, in order to artificially increase the imperfection.

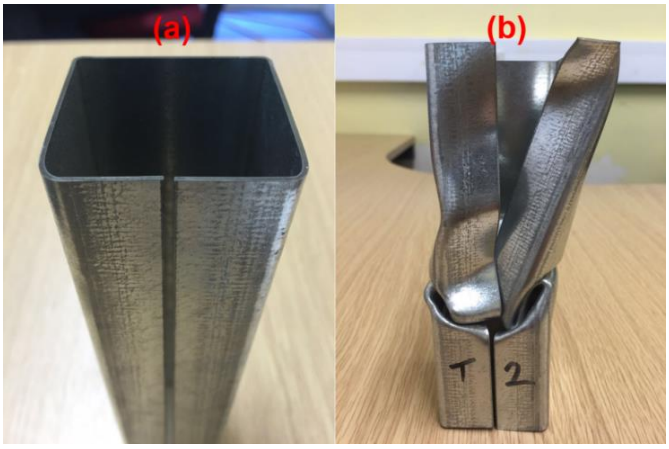

Fig. 4.11. (a) Cross-sectional surface and (b) typical deformed shape of wire-cut samples under the impact velocity of 3.44 m/s

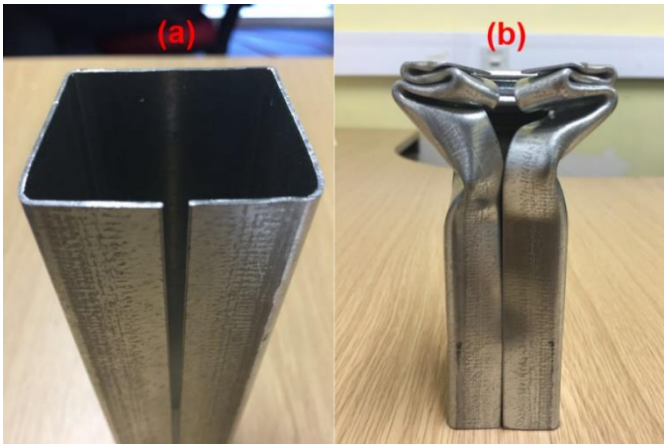

Fig. 4.12. (a) Cross-sectional surface and (b) typical deformed shape of band saw-cut samples under the impact velocity of 3.44 m/s

Fig. 4.13. Deformed shape of band saw-cut samples without triggers under the impact velocity of 4.33 m/s

Another phenomenon observed in both trial and formal tests is side-sliding. Due to the uncertainty of imperfections, asymmetric crushing modes may occur after several layers of folds have been formed (i.e. the crushed columns tend to slide towards one side), as illustrated in Fig. 4.14. It was found that four out of the five plain samples showed noticeable side-sliding, while only one out of the five dimpled samples showed noticeable side-sliding. This phenomenon may reveal that dimpled columns are less likely to be affected by the imperfections. However, due to the number of tests, such a conclusion cannot be made yet.

Fig. 4.14. Asymmetrically crushed columns

4.2.2 Numerical analysis

Finite element models were built to simulate the dynamic crushing tests. The tests were simulated using the Explicit Dynamics module in ANSYS Workbench 17.1 software package. The details of the FE modelling method are introduced in this section. The numerical results were compared to the experimental results, in order to validate the FE method.

4.2.2.1 FE modelling

The geometric modelling and meshing process were completed in ANSYS Mechanical APDL. These two processes were challenging as the dimpled geometry was difficult to be described and specified. In this study, two types of generic models with shell elements were used to assemble the whole dimpled column. The two types of generic models are: (1) a normal single dimple and (2) a 90-degree corner single dimple, as shown in Fig. 4.15(a) and 4.15(b), respectively. As introduced in Chapter 3, a normal single dimple model can be obtained from the numerical results of the UltraSTEEL® forming process. As for the 90-degree corner single dimple, in reality, the corner is obtained by feeding the dimpled plate through a series of rolls, which gradually bend the dimpled plate from 0 to 90 degrees. Therefore, the corner dimple model was obtained by fully fixing one end and applying an angular displacement of 90 degrees on the other end of a normal dimple. Corner dimpled models with other angles can be obtained using the same approach.

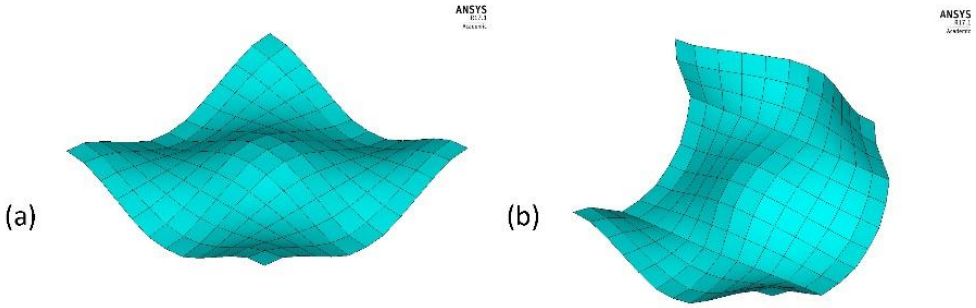

Fig. 4.15. (a) Normal single dimple and (b) 90-degree corner single dimple

Through patterning the normal and corner generic dimpled models in ANSYS Mechanical APDL, a geometric model of the dimpled structure and other accessories (e.g. the impactor) was built. The geometric model was then meshed in ANSYS Mechanical APDL.

The impactor was meshed using hexahedral 8-node solid elements. The plain and dimpled columns were meshed using full-integration thin shell elements with four nodes and five integration points throughout the thickness. Thin shell elements were selected over solid and thick shell elements because of the limitation of computing power. Although thin shell elements do not allow non-linear stress/strain distribution throughout thickness, which may potentially cause inaccuracy when dealing with folds and buckling, thin shell elements are usually used to predict the crushing behaviour of thin-walled structures in research works [11, 12, 16, 17, 24, 27]. In addition, Nguyen et al. [95, 96] has also demonstrated the validity of using thin shell elements to simulate the buckling behaviour of dimpled thin-walled structures. A sensitivity study on mesh density was carried out. The result of the mesh size sensitivity study is shown in Fig. 4.16. It can be found that the specific energy absorption (SEA) converges when there are 26,720

elements in the plain columns, corresponding to a uniform element size of 1 mm. Therefore, the element size of 1 mm was used for the plain FE models, which was similar to the work published by other researchers. However, the element size of 1 mm caused severe geometrical distortion for the dimpled FE models, due to the complicated dimpled geometry. Therefore, for the dimpled models, an element size of 0.55 mm was used.

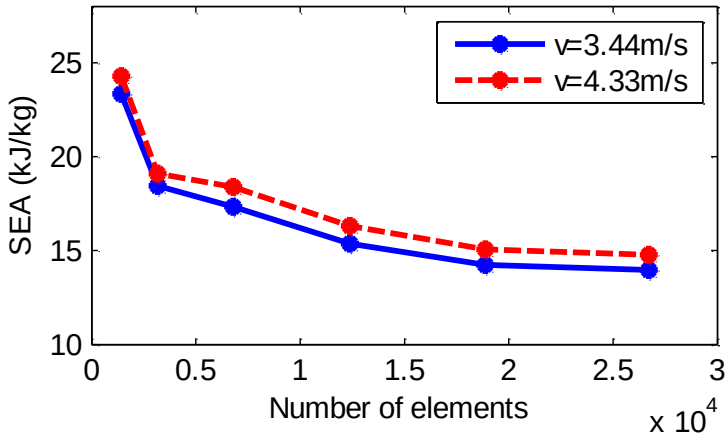

Fig. 4.16. Results of the sensitivity study on the element size

After the meshing process, the files containing information of all the elements and nodes were imported into the ANSYS Workbench Explicit Dynamics module. The imported plain and dimpled FE models are shown in Figs. 4.17 and 4.18, respectively. In the FE models, the length of the columns was 160 mm, which was equal to the effective crushing length in the experiments. All the nodes attached to the bottom of the columns were fully fixed in all DOFs. Standard earth gravity was applied along z-axis. The impactor was treated as a rigid body. An initial velocity of the rigid impactor was specified along z-axis. The DOF along x

and y axes of the impactor was restrained, representing the impactor travelling along tracks.

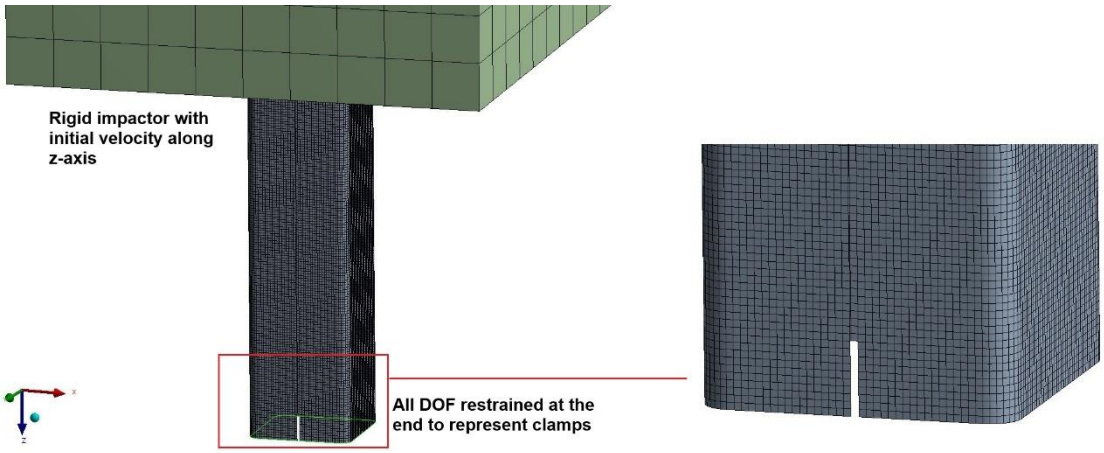

Fig. 4.17. FE model of the plain column

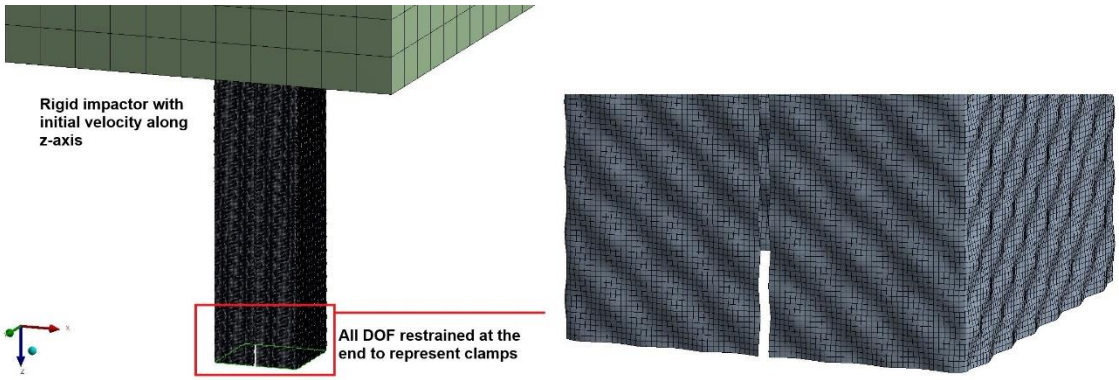

Fig. 4.18. FE model of the dimpled column

As mentioned in Section 4.2.1, the gap size of the specimens varies from 1 to 3 mm. Therefore, three gap sizes were compared in order to determine which gap size to use in the simulations. Fig. 4.19 shows the crushing force – axial displacement curves when the gap sizes are 1, 2 and 3 mm, respectively. It can be seen that within the range from 1 to 3 mm, the influence of the gap size on the

crushing force was negligible. Therefore, a representative gap size of 2 mm was adopted for all the plain and dimpled FE models.

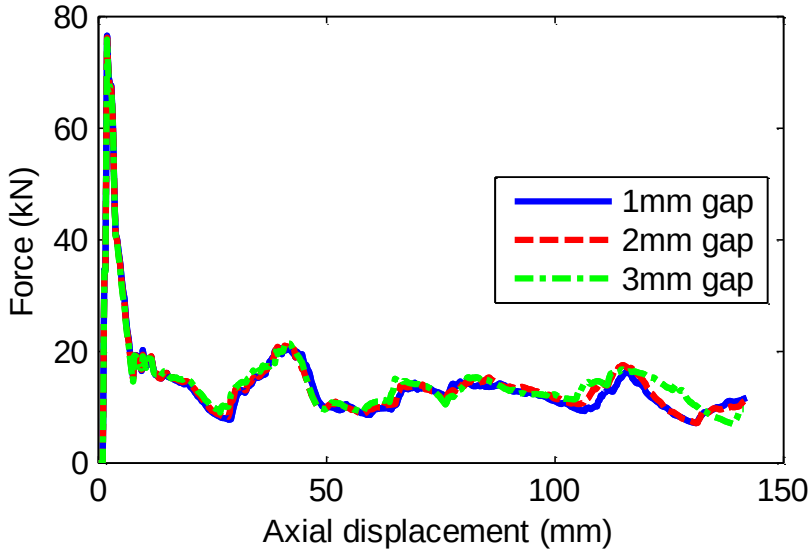

Fig. 4.19. Force – axial displacement curves for columns with gap sizes of 1 to 3 mm

In the simulations, triggers were introduced to initiate the crushing process. Prior to the impact, two rigid bodies pressed the free end of the flanges inward from both sides to create imperfection. The triggering position was selected based on the experimental observations. Fig. 4.20 shows the plain and dimpled columns after the triggering and before the impact starts, where the imperfection created by the triggers is highlighted. Fig. 4.21 illustrates the failure modes with and without triggers. Through comparison, it is evident that the plastic deformation starts at the free end when triggers are applied, and a random position when triggers are not applied.

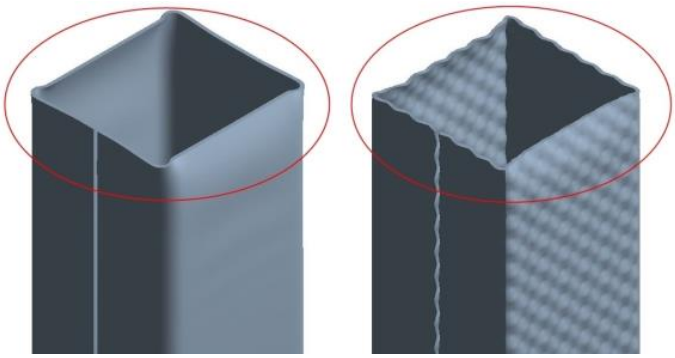

Fig. 4.20. Plain and dimpled columns after introducing triggers

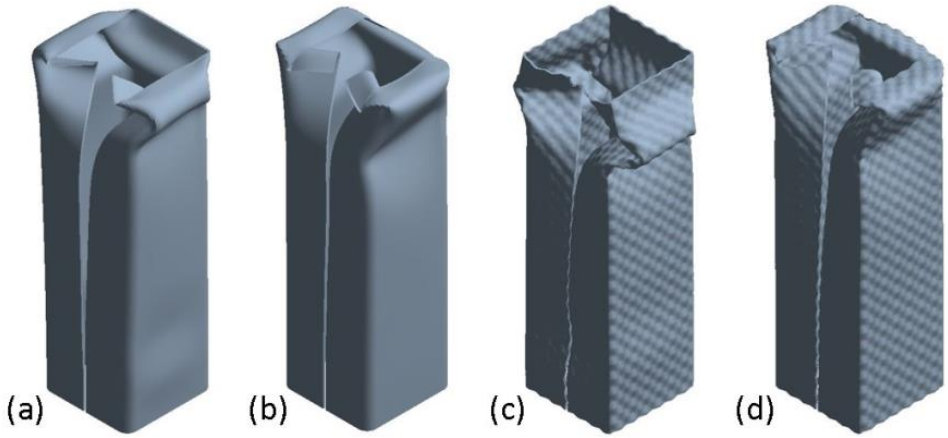

Fig. 4.21. Crushing process for (a) plain column without triggers, (b) plain column with triggers, (c) dimpled columns without triggers and (d) dimpled columns with triggers

As introduced in Chapter 2, the stress in materials can be significantly influenced by the strain rate. In this study, the strain rate is between 0.1 and 100 s^{-1}. Therefore, the strain rate sensitivity of materials must be taken into account. Two models are commonly used in similar researches to characterise materials' strain rate sensitivity: (1) Cowper-Symonds material model and (2) Johnson-Cook material model. The primary difference of these two material models is that the

Johnson-Cook material model takes the thermal stress into account. In this study, the average temperature rise does not exceed 20 K, assuming the kinetic energy is completely converted to internal energy of columns. Therefore, the effect of thermal stresses can be neglected, and the Cowper-Symonds material model was adopted, as shown in Eq. 4.3. The strain hardening coefficients B and n were determined from the quasi-static tensile tests, which has already been explained in Chapter 3, and the strain rate coefficients D and q were adopted from previous similar research papers. The true stress-strain curves for the plain and dimpled materials at different strain rates are shown in Fig. 4.22.

$$\sigma^d = \left(\sigma_y + B\varepsilon^n\right)\left[1 + \left(\frac{\dot{\varepsilon}}{D}\right)^{1/q}\right] \tag{4.3}$$

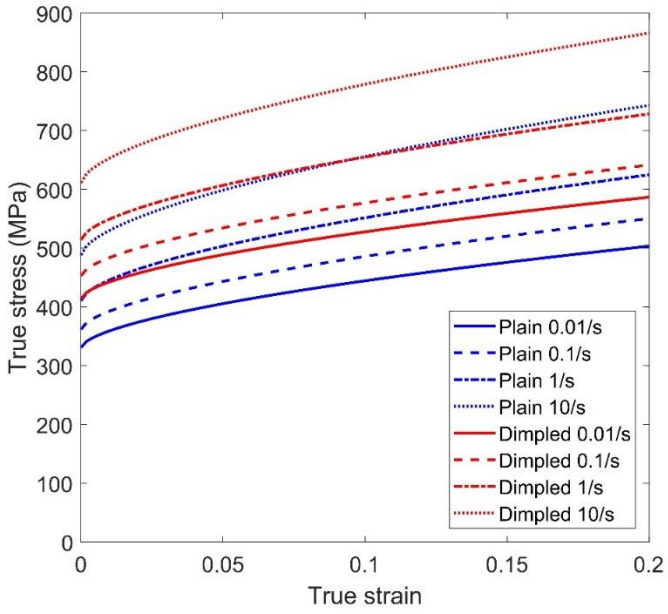

Fig. 4.22. True stress – strain curves at different strain rates

In this study the AUTODYN automatic contact with the penalty formulation and trajectory detection method. The self-contact of bodies was also taken into account. The sheet thickness factor was set to be 1 and the friction coefficient

was set to be 0.3. When simulating the dynamic crushing events, the AUTODYN standard hourglass error energy control was applied, to ensure that the hourglass energy was not higher than 5% of the total energy. An example of the energy conservation in the simulations is presented in Fig. 4.23.

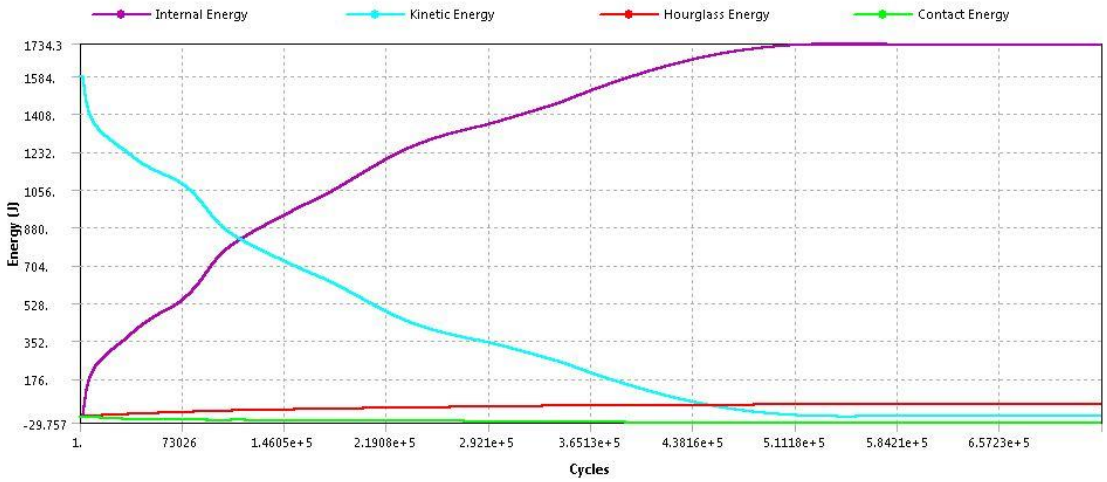

Fig. 4.23. An example of the energy conservation when simulating the crushing events

4.2.2.2 FE results and validation

The numerical and experimental results were compared from the following three aspects:

- Instantaneous crushing force and energy absorption: The numerical and experimental crushing force and energy absorption curves are shown in red and blue, respectively, in Fig. 4.24. It was observed that the numerical and experimental results agreed very well. Most of the features in the experimental tests were successfully captured in the simulations, except for the initial peaks. The initial peaks in the simulations occurred

prematurely. This was due to the fact that the Cowper-Symonds material model was used in the numerical analysis. As a result, the numerical stress-strain curves started from the yielding points. However, it does not significantly affect the prediction of the whole crushing process.

- Failure mechanisms: numerical and experimental failure modes are shown in Fig. 4.25. All the numerically crushed columns were extended for 40 mm, representing the part clamped by the fixture in the experimental tests, as introduced in Sections 4.2.1.1 and 4.2.2.1. Overall, the agreement is good. However, it was noted that the folding wavelengths tend to be slightly overestimated in the simulations. For example, in Fig. 4.25(d), the fourth layer of folds has fully developed in the experiment while the fourth layer of folds is still developing in the simulation. To be more specific, in the 3.44 m/s tests, the numerical folding wavelengths are 3.36% and 7.83% greater than the experimental ones for plain and dimpled columns, respectively. In the 4.33 m/s tests, the numerical folding wavelengths are 3.34% and 16.81% greater than the experimental ones for plain and dimpled columns, respectively.

- Specific energy absorption (SEA): as shown in Table 4.2, the errors of numerical SEA do not exceed 5%. Therefore, the numerical SEA can be considered to be accurate.

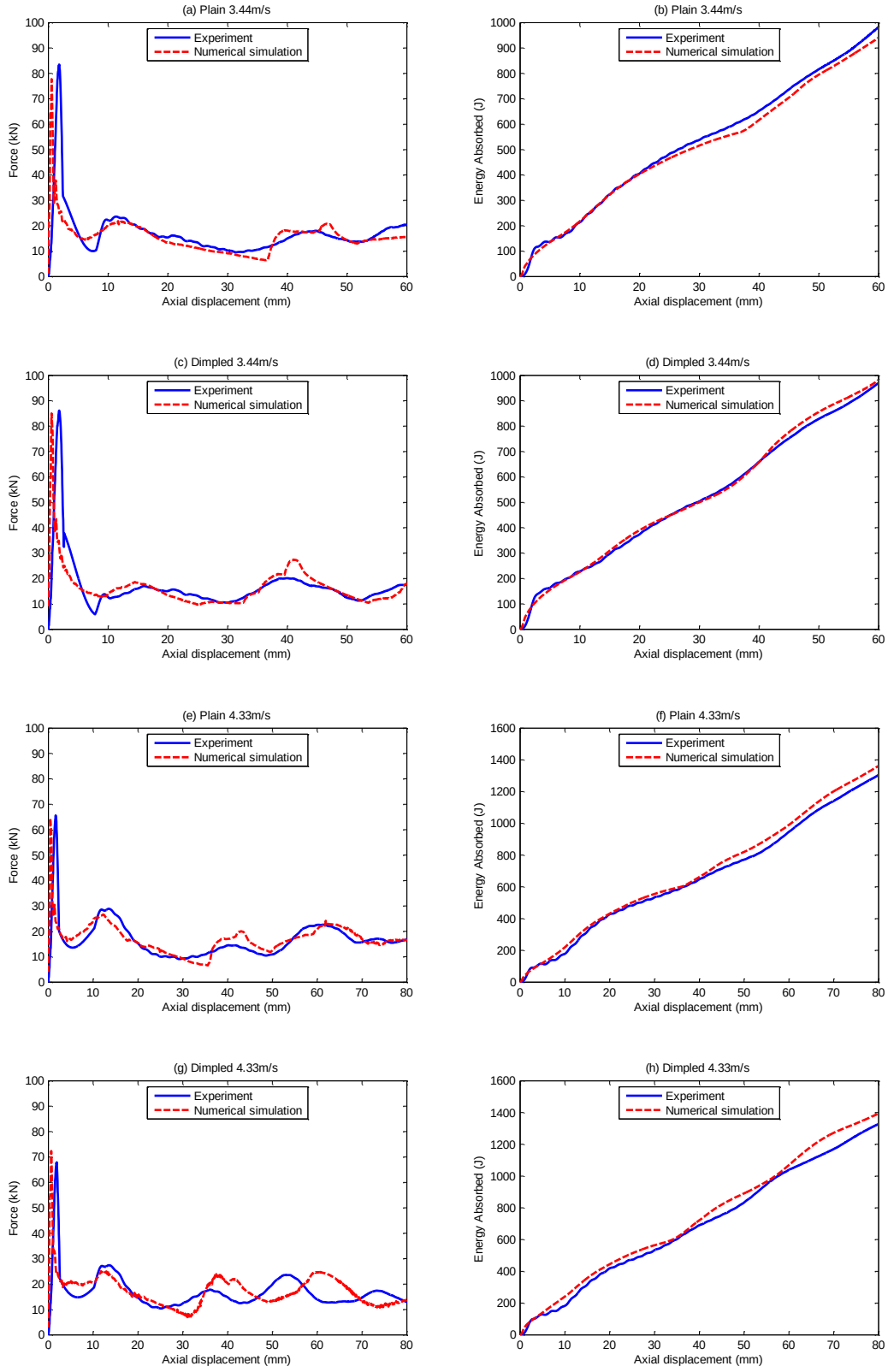

Fig. 4.24. Numerical and experimental force – axial displacement and energy absorbed – axial displacement curves for (a, b) plain 3.44 m/s, (c, d) dimpled 3.44 m/s, (e, f) plain 4.33 m/s and (g, h) dimpled 4.33 m/s

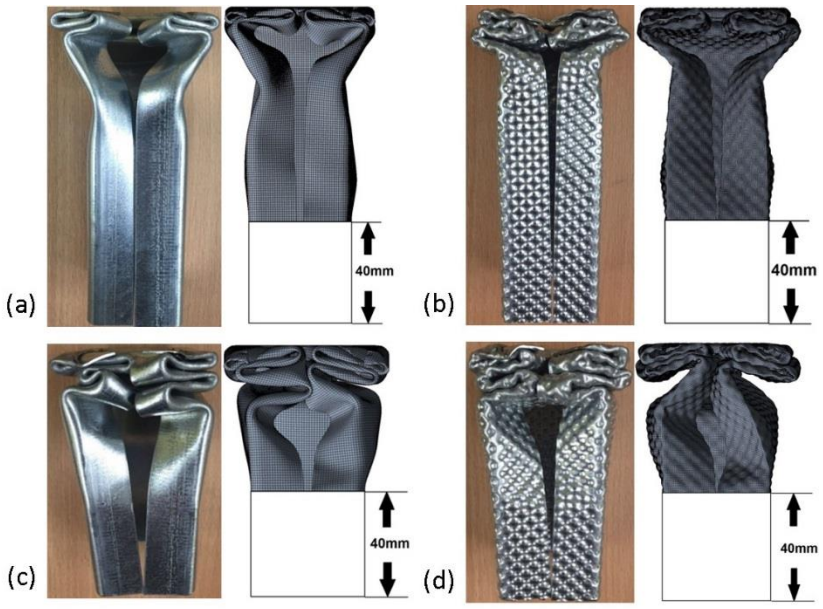

Fig. 4.25. Experimental and numerical failure modes of (a) plain 3.44 m/s, (b) dimpled 3.44 m/s, (c) plain 4.33 m/s and (d) dimpled 4.33 m/s

Table 4.2. Experimental and numerical SEA of plain and dimpled columns

Material	Impact velocity (m/s)	EXP SEA (kJ/kg)	FE SEA (kJ/kg)	Error
Plain	3.44	11.437	11.140	2.60%
Dimpled	3.44	12.628	12.113	4.08%
Plain	4.33	11.351	11.774	3.73%
Dimpled	4.33	12.376	12.818	3.57%

4.3 Response of open section columns to quasi-static crushing loads

The purpose of the quasi-static compression tests and simulations is to further validate the FE method when being applied to simulate the quasi-static process. This section includes the test procedures, major differences from the dynamic

tests in FE modelling, and the comparison between numerical and experimental results.

The quasi-static compression experimental tests were conducted at Hadley group. Five plain specimens and five dimpled specimens were tested. The samples used in the quasi-static experimental tests are identical to those in the dynamic tests. The experimental setup is illustrated in Fig. 4.26. The specimens were placed in the test rig with the bottom end fixed. The specimens were compressed under a constant axial displacement rate of 0.5 mm/s. Displacement transducers (LVDTs) were fitted to measure the axial shortening of the samples. When designing the quasi-static tests initially, it was anticipated that the computing time required to simulate the quasi-static compression tests will be significantly longer than dynamic tests, which means it is only practical to simulate a small part of the crushing process. Therefore, the axial compressive load was only applied till the first layer of folds was formed.

Fig. 4.26. Experimental setup of the quasi-static compressive tests

The FE models used for the quasi-static tests are similar to the ones used for the dynamic tests. Three major modifications have been made to better represent the quasi-static process. All setups other than the following three points are the same as in the dynamic FE models.

- Piecewise linear true stress-strain curves were assigned, instead of the previously used Cowper-Symonds material model, as the strain rate effect was negligible in the quasi-static tests.
- Triggers were applied at the buckling positions observed in the experimental tests, to initiate the crushing process.
- A rigid plate was added at the top end of the columns. A constant axial velocity was applied on the plate instead of initial velocities in the dynamic simulations. Additionally, although only a small part of crushing process was simulated, it was still impractical to use the actual displacement rate (i.e. 0.5 mm/s) in the simulations. Therefore, a sensitivity study was carried out to determine the most appropriate displacement rate to use in the numerical analysis. Through the sensitivity study, it was found that when the displacement rate of 100 mm/s (i.e. 200 times of the actual displacement rate) can provide sufficiently accurate results and an acceptable computational time. Therefore, the axial displacement rate was set to be 100 mm/s in the quasi-static simulations.

The numerical and experimental force – displacement curves are shown in Fig. 4.27. Overall, when comparing the numerical and experimental results, good agreement can be found. The errors in the peak forces are 4.6% and 4.9% for

plain and dimpled columns, respectively. Additionally, it has been shown that the maximum load dimpled column took is 25.85% higher than that of the plain column in the experiments and 26.21% higher in the numerical simulations. Last but not least, the numerical force – displacement curves are less smooth than the experimental ones. It is due to the high displacement rate applied in the simulations. Smoother curves can be observed when lower displacement rates are applied.

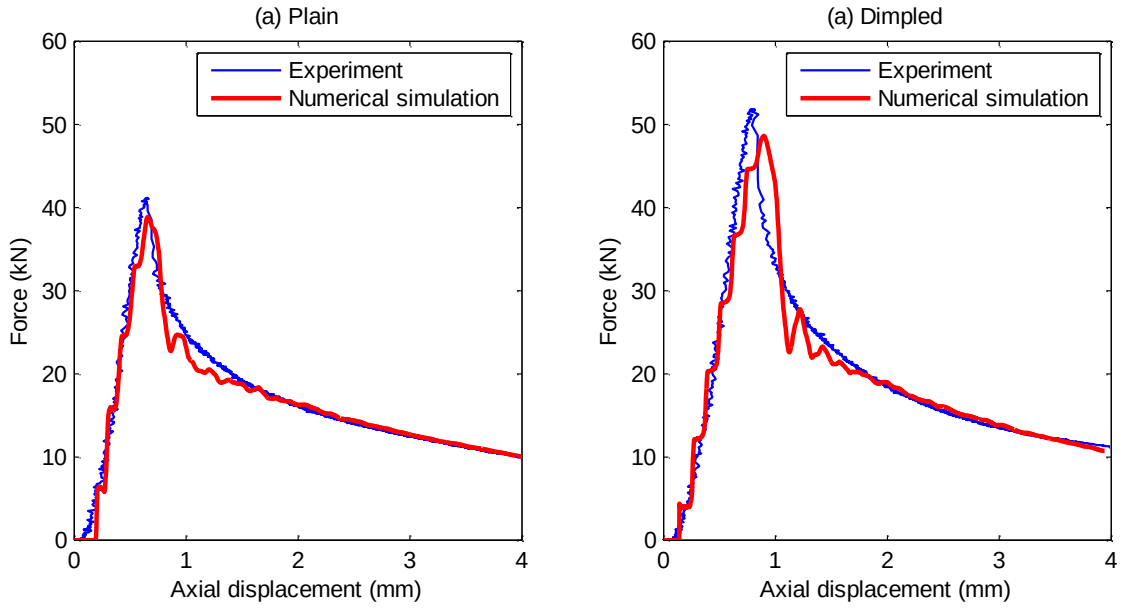

Fig. 4.27. Experimental and numerical force – displacement curves for quasi-static tests

4.4 Summary

In this chapter, dynamic and quasi-static crushing experiments were conducted. FE models for plain and dimpled samples were created to simulate the experimental tests. The FE models were validated by comparing the numerical

results to experimental results, especially in terms of failure mechanism, instantaneous crushing force and instantaneous energy absorption. The following conclusions can be made from this study:

- Dynamic experimental tests were performed with two impact energies of approximately 1 kJ and 1.6 kJ. Specific energy absorption (SEA) was employed to evaluate the energy absorption performance of the samples. Comparing to the plain samples, SEA of the dimpled samples are 10.40% and 9.02% under the two test conditions, respectively.
- The explicit dynamics module integrated in ANSYS Workbench was used to simulate the experiments. The geometric models were constructed based on two types of generic models. 1 mm was selected to be the element size for the plain models, because of the element size sensitivity study. 0.55 mm was selected to be the element size for the dimpled models, because of the complicated dimpled geometry and the element size sensitivity study. The Cowper-Symonds material model was employed to take the strain rate effect into account.
- For the dynamic crushing tests, the numerical and experimental results agree very well in terms of the failure mechanism, crushing force and energy absorption performance. The errors in SEA are not greater than 4.08% for all the test conditions. The FE method was therefore considered to be accurately predicting the response of plain and dimpled columns to dynamic loads.
- Quasi-static experimental tests were performed on the plain and dimpled samples, which were identical to the ones used in the dynamic tests. The quasi-static tests were then reproduced using the explicit dynamics FE

method. It was revealed that the FE method can also accurately predict the response of plain and dimpled columns to quasi-static loads with some modifications on the material properties and loading rates.

Chapter 5 Numerical investigation of the crashworthiness of thin-walled dimpled columns under axial impact loads

5.1 Introduction

Thin-walled structures are widely used as energy absorbers in sea, land and air vehicles. Among various types of loading conditions, axial impact is one of the most important loads that thin-walled structures are designed to withstand for protecting passengers.

This chapter aims to investigate the behaviour and energy absorption performance of dimpled thin-walled columns under axial impact loads. To achieve this aim, numerical simulations were conducted, using the FE method validated in Chapters 3 and 4. In this chapter, the response of plain and dimpled columns to axial impact loads were compared. Additionally, a series of parametric study on the forming depth and gauge thickness was carried out to optimize the dimpling forming process. Finally, the behaviour of plain and dimpled columns subjected to inclined axial crushing loads were compared and discussed. The main objectives of this chapter are:

- Modifying the FE models used in Chapter 4 in accordance with the boundary conditions, and making simplifications.
- Identifying the behaviour of dimpled columns under axial impact loads, and comparing the failure mechanisms of plain and dimpled columns.

- Understanding the effects of the dimpled geometry on the energy absorption characteristics.
- Understanding the effects of the forming depth and gauge thickness on the mechanical properties of dimpled materials.
- Understanding the effects of the forming depth and gauge thickness on the energy absorption performance.
- Identifying the difference between plain and dimpled columns when subjected to inclined crushing loads.

5.2 FE modelling

The explicit dynamics code integrated in ANSYS Workbench 17.1 was employed to simulate the axial crushing process in this chapter.

Hollow square cross-sectional thin-walled columns were used in the analysis. When the columns are subjected to axial loads, three failure modes can be identified depending on the slenderness ratio, which is defined in Eq. 5.1, where the effective length L_{eff} and the radius of gyration r were defined in Eqs. 5.2 and 5.3, respectively. The coefficient K in Eq. 5.2 depends on the support conditions of the column. As illustrated in Fig. 5.1, a column is considered to be short, intermediate and long when the slenderness ratio λ is smaller than 40, between 40 and 150, and greater than 150, respectively. When being used as kinetic energy absorbers, the thin-walled columns must be short to achieve good energy absorption performance in terms of stability and efficiency. The dimensions of the columns in this study were specified by taking the slenderness ratio factor into

consideration. The baseline length, width and gauge thickness were 250 mm, 46 mm and 1 mm, respectively, resulting in a slenderness ratio of approximately 13, which satisfied the requirement as short column.

$$\lambda = \frac{L_{eff}}{r} \tag{5.1}$$

$$L_{eff} = K \times L \tag{5.2}$$

$$r = \sqrt{\frac{I}{A}} \tag{5.3}$$

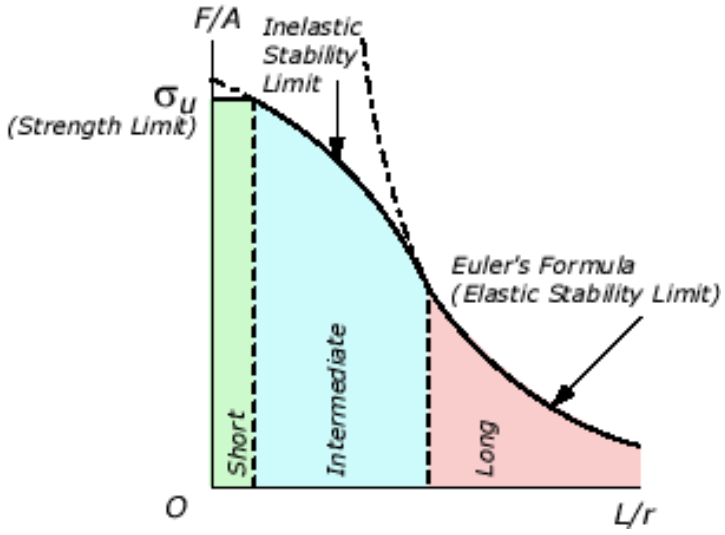

Fig. 5.1. Strength limit – slenderness ratio for columns under axial loads [103]

The boundary conditions are shown in Fig. 5.2. The bottom end of the column was fixed in all directions, and the other end was free. The 250.89 kg rigid impactor had an initial velocity of 6 m/s along the z-axis (i.e. the impact energy was 4.5 kJ). The translational DOFs of the rigid impactor was restrained in x and y directions, representing the impactor was sliding along a track. Imperfections were introduced at the top of the column to ensure that the crushing process

initiated from the top of the column. It was also ensured through running trial simulations that the influence on the initial peak forces due to the imperfections were less than 2%. Moreover, symmetric boundary conditions were applied to simplify the FE model, which significantly increased the computing efficiency. The original full models were simplified down to quarter models, after applying the symmetric boundary conditions about yz and xz planes. The responses of the original and simplified models under the above loading conditions were found to be identical.

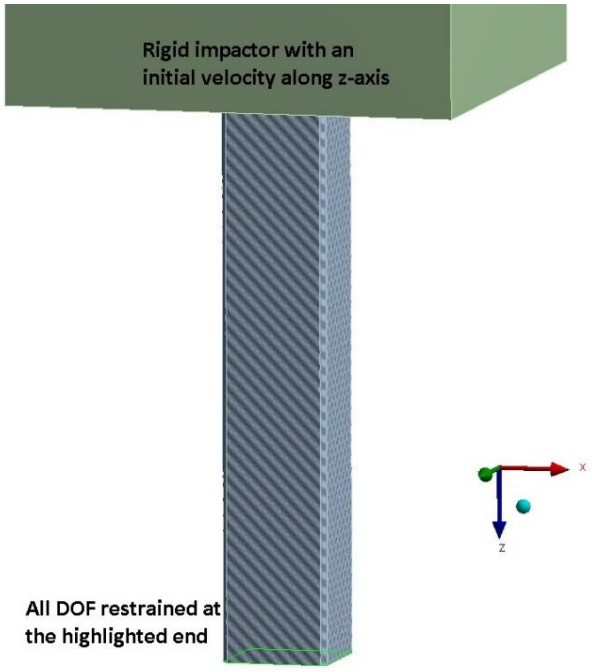

Fig. 5.2. FE model of the dimpled column and impact mass

Apart from the geometries and boundary conditions, the other setup for the FE models remained the same as described in section 4.2.2.1. To summarize, the important setups of the FE models were:

- The Cowper-Symonds material model was used to include the strain rate sensitivity of plain and dimpled materials.
- 4-node full-integration shell elements with five integration points throughout the thickness were used to mesh the plain and dimpled columns. 8-node solid elements were used to model the impactor, which can be approximately treated as a rigid body.
- A uniform element size of 1 mm was used for all the plain columns, and a uniform element size of 0.55 mm was used for all the dimpled columns.
- The penalty formulation and trajectory detection method were used to deal with contact. The sheet thickness factor was set to be 1 and the friction coefficient was set to be 0.3.

5.3 Typical crushing process of dimpled columns

In order to investigate the energy absorption performance of dimpled columns, it is crucial to understand the crushing process. As introduced in Chapter 2, the failure mechanism of the square section thin-walled columns has been well studied. In this section, the typical crushing process of dimpled columns is compared to the conventional plain counterparts.

For dimpled columns subjected to axial crushing loads, the typical deformed shapes, force – axial displacement relations and specific energy absorption (SEA) – axial displacement relations are shown in Fig. 5.3.

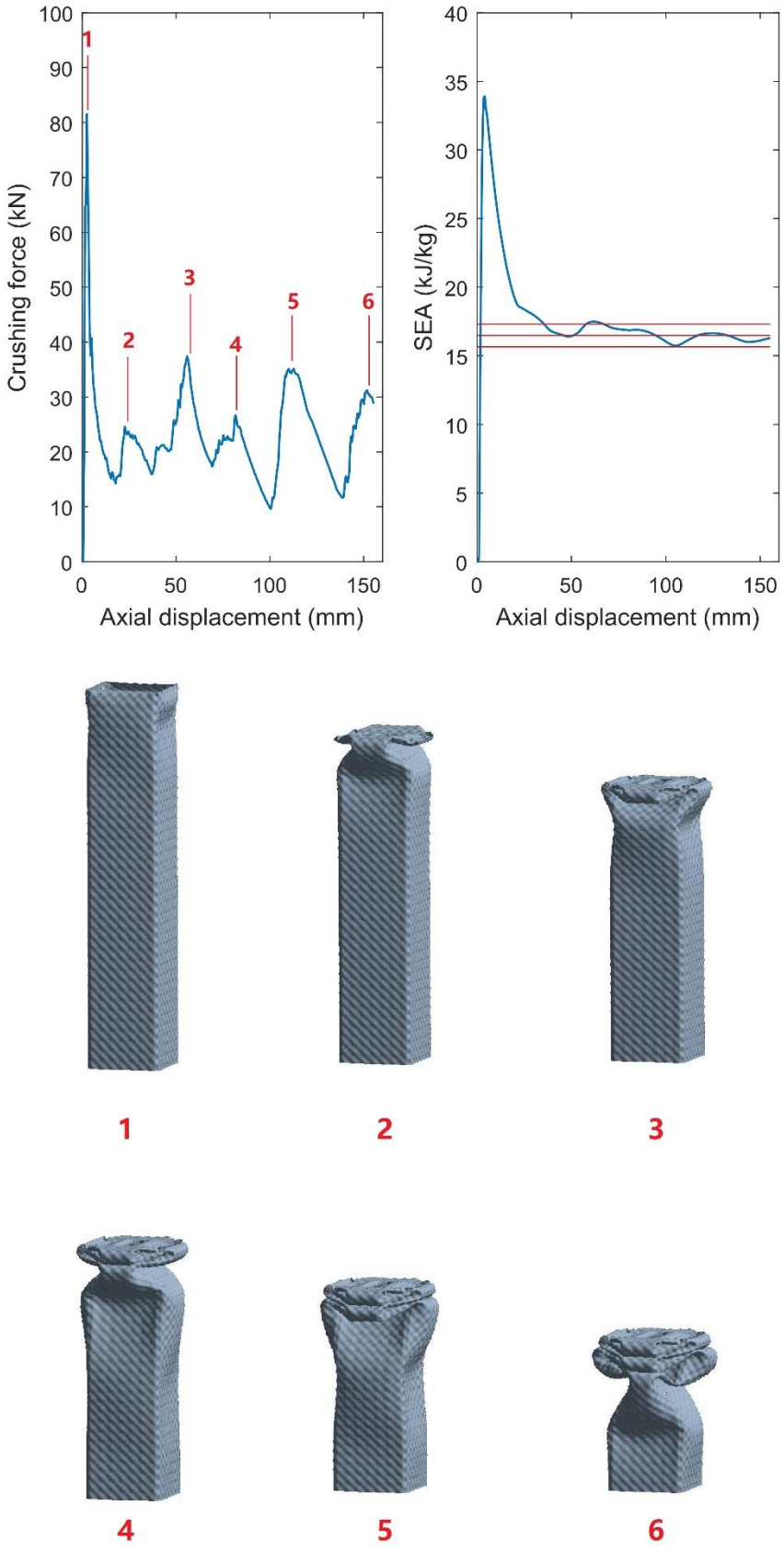

Fig. 5.3. A typical axial crushing process of dimpled square section columns

Overall, the crushing process of dimpled columns is very similar to that of plain columns. Contrary to the plain columns, the wavelength (i.e. peak-to-peak distance in the force – displacement curve) of dimpled columns is not constant. Additionally, no pattern in the variation of wavelength can be found. The SEA value was determined by applying linear fitting to the energy absorbed – axial displacement curve, as described in Section 4.2, and the steady-state SEA value was represented by the middle red lines in the SEA – axial displacement curves. Although the wavelength was not constant, it can be found that the SEA value has converged and varied within the 5% error range after the third layer of folds was formed. Therefore, in order to reduce the computational time while not sacrificing the accuracy in SEA, the simulations lasted only until 6 layers of folds were formed, instead of the whole column were crushed.

5.4 Optimization study of the forming depth and gauge thickness

In the dimpling forming process, the forming depth is defined as the relative vertical movement between the upper and lower forming teeth, as shown in Fig. 5.4. The forming depth can be directly controlled by adjusting the relative positions of the rollers. It is obvious that different forming depths and gauge thickness have a direct influence on the geometry of the dimpled plates, which will subsequently affect the energy absorption performance, as explained in Section 5.3. Additionally, the forming depth and gauge thickness are dominant factors for the mechanical properties of the dimpled plates due to work hardening, which will also significantly affect the energy absorption performance. Fig. 5.5 shows how the energy absorption performance of dimpled structures are

dependent on the forming depth. In this section, the effects of the forming depth on energy absorption performance through the “Geometry” pathway and “Mechanical properties” pathway are numerically analysed individually as well as combined. The purpose of this analysis is to help to understand the significance of the dimpled features as well as to optimize the forming process for the best yield strengths and energy absorption performance.

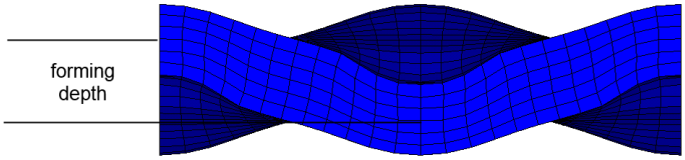

Fig. 5.4. Forming depth in the UltraSTEEL® dimpling forming process

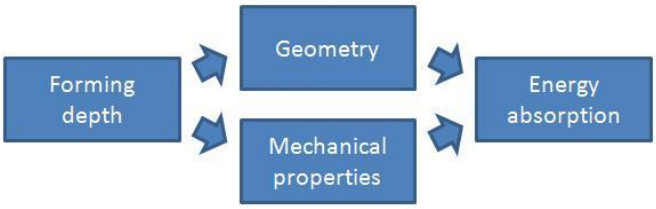

Fig. 5.5. The relationship between forming depth and energy absorption performance of dimpled structures

5.4.1 Effect of the forming depth on mechanical properties

During the forming process, work hardening is developed, which causes the equivalent yield strength of the dimpled plate to increase, as explained in Chapter 3. However, it was noted that the equivalent yield strength of dimpled plates does not always increase with the forming depth increase. The UltraSTEEL® dimpling

forming process and the tensile tests for various gauge thickness and forming depths were simulated, using the method presented in Chapter 3. The numerical results of equivalent yield strengths varying with forming depths are shown in Fig. 5.6.

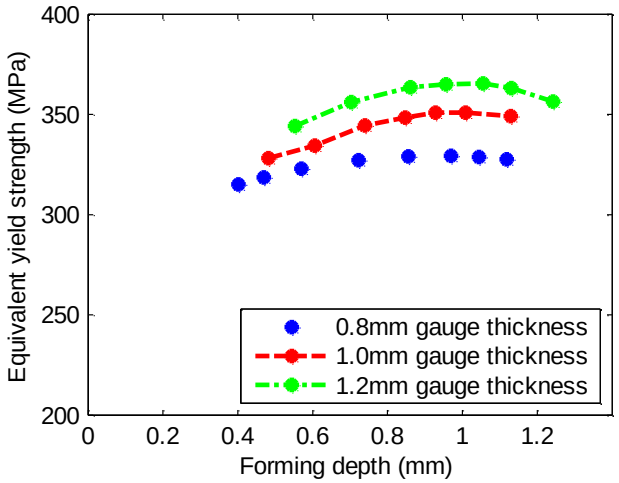

Fig. 5.6. Equivalent yield strengths – forming depth

The results in Fig. 5.6 shows that for the 0.8 to 1.2 mm gauge thickness plates, the equivalent yield strength tends to peak when the forming depth is approximately 1 mm. The drop in the yield strength is caused by the stress concentration due to the dimpled geometry. When the dimpled plates are being pulled in tensile tests, higher von-Mises stress can be observed in the peak and trough regions of dimples. Therefore, when the dimpled plates are subjected to tensile loads, yielding in some local areas has already initiated while other areas are still in the elastic region. Figs. 5.7 and 5.8 show the von-Mises stress distributions under axial tensile loads for the 1 mm gauge dimpled steel plates at the equivalent strains of 0.1% and 0.2%, respectively. In both cases, the stress concentration effect is more severe for higher forming depths. The same

phenomenon was also observed on the dimpled plates with other gauge thickness.

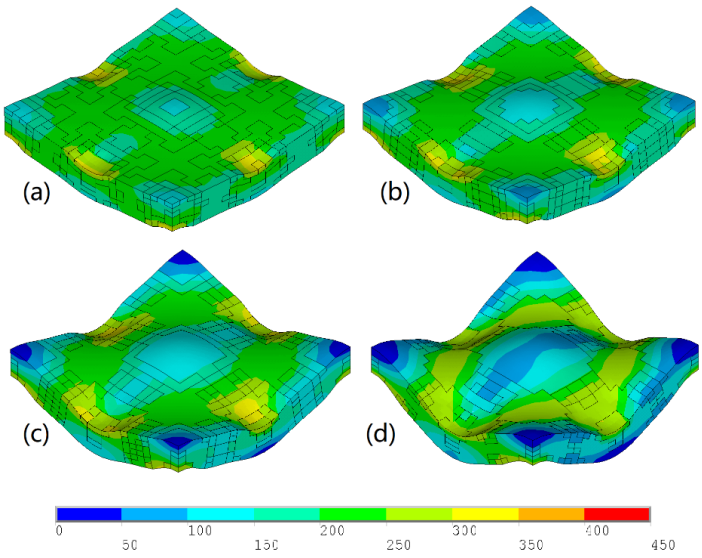

Fig. 5.7. Von-Mises stress (MPa) in dimpled plates under tensile loads with 0.1% equivalent strain and forming depths of (a) 0.5 mm, (b) 0.75 mm, (c) 1 mm and (d) 1.25 mm

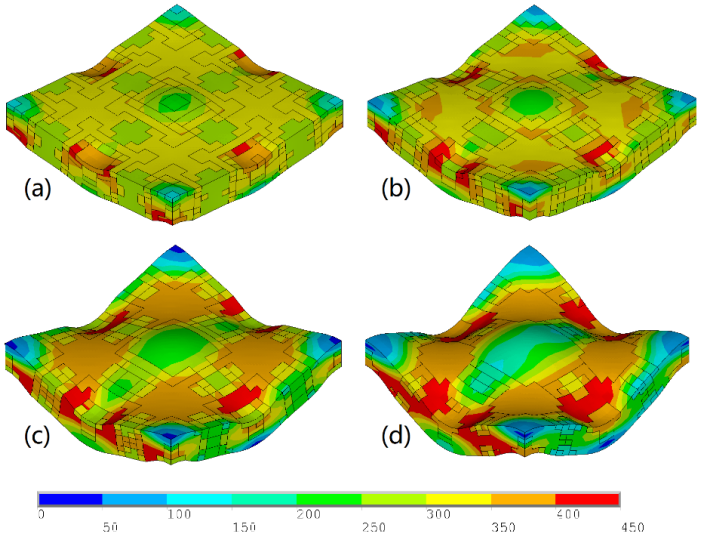

Fig. 5.8. Von-Mises stress (MPa) in dimpled plates under tensile loads with 0.2% equivalent strain and forming depths of (a) 0.5 mm, (b) 0.75 mm, (c) 1 mm and (d) 1.25 mm

To quantify the results, the normalized stress is used as the indicator, as defined in Eq. 5.4. The maximum and minimum normalized stress values are shown in Fig. 5.9. The trends of maximum and minimum normalized stress values are diverging as the forming depth increasing. It reveals that the stress concentration in dimpled plates is more severe when greater forming depths are used. Therefore, it can be concluded that as the forming depth increasing, the work hardening effect outweighs the stress concentration effect before the maximum equivalent yield strength is reached, and vice versa thereafter.

$$Normalized\ stress = \frac{Local\ stress \times Sectional\ area}{Axial\ tensile\ force} \tag{5.4}$$

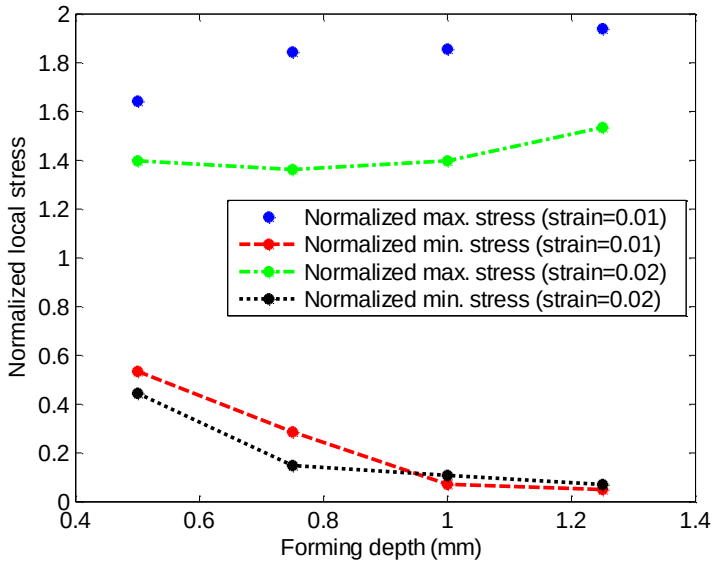

Fig. 5.9. Maximum and minimum normalized local stress – forming depth for the 1 mm gauge dimpled plates

Besides influencing the equivalent yield strengths, the stress concentration effect was also found to influence the dimpled plates' behaviour when transforming from the elastic region to the plastic region. The numerical and experimental stress-strain curves for plain and dimpled steel plates are presented in Fig. 3.12. It can

be observed that in the experimental tests and numerical simulations, the transition from the elastic region to the plastic region is smoother for dimpled plates. This is due to the fact that in plain plates, all the local elements enter the plastic region simultaneously, while in dimpled plates, because of the stress concentration, the local elements enter the plastic region gradually. However, as this project focuses on the response of the dimpled structures subjected to dynamic impact loads, where the plastic deformation is in dominance, the transition from the elastic region to the plastic region for plain and dimpled materials is not analysed in detail.

5.4.2 Effect of the various dimpled geometries on energy absorption performance

In order to better understand the influence of the dimpled geometry on the energy absorption performance, the variation of material properties is not taken into account at this stage. In this section, the variable normalized SEA is employed to evaluate the energy absorption performance, as the normalized SEA better reflects the difference between dimpled columns and the comparable plain ones. The normalized SEA is defined in Eq. 5.5. The variation of normalized SEA against forming depth with the work hardening effect neglected is shown in Fig. 5.10. The results show that the normalized SEA values vary from 1.013 to 1.035, 1.015 to 1.025, 1.006 to 1.027 and 0.976 to 1.019 for 0.7, 0.8, 0.9 and 1.0 mm gauge columns, respectively. It means that the dimpled geometry does not significantly affect the SEA. Although the influence of the dimpled geometry is not significant, obvious SEA drops can be spotted when the forming depth increases

beyond 0.9 mm. This is mainly due to the enhanced stress concentration and the reduced actual wall thickness.

$$Normalized\ SEA = \frac{SEA}{SEA\ of\ the\ original\ plain\ column} \tag{5.5}$$

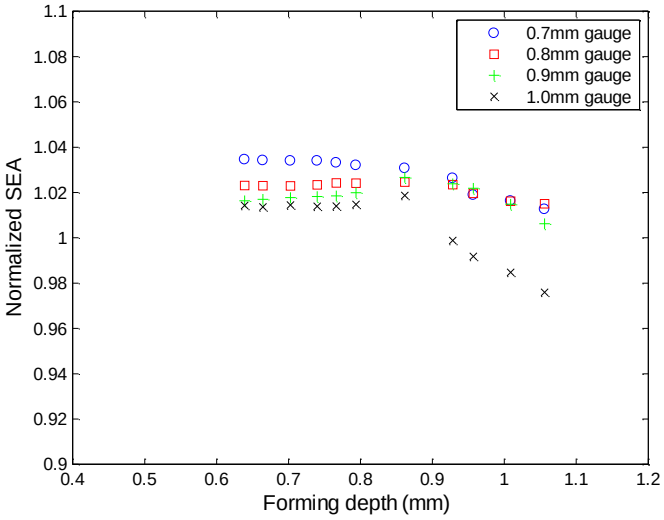

Fig. 5.10. Normalized SEA – forming depth (work hardening not taken into account)

5.4.3 The overall effect of the forming depth on energy absorption performance

The effect of the forming depth on SEA must be comprehensively analysed when both the dimpled geometry factor and the material properties factor are taken into account. Fig. 5.11 shows the SEA values of dimpled columns. It can be observed that the SEA values tend to peak at specific forming depths. The drop in SEA after the peak points is mainly due to the reductions in yield strengths and the actual wall thickness. To clearly find out the relation between the optimal forming depth and the gauge thickness, the variable normalized forming depth, as defined

in Eq. 5.6, is employed. The results shown in Fig. 5.12 indicate that the optimal forming depth is nearly proportional to the gauge thickness. For 0.7, 0.8, 0.9 and 1.0 mm gauge dimpled columns, the maximum SEA values are 10.4%, 13.7%, 14.9% and 16.3% higher than the comparable plain ones, respectively.

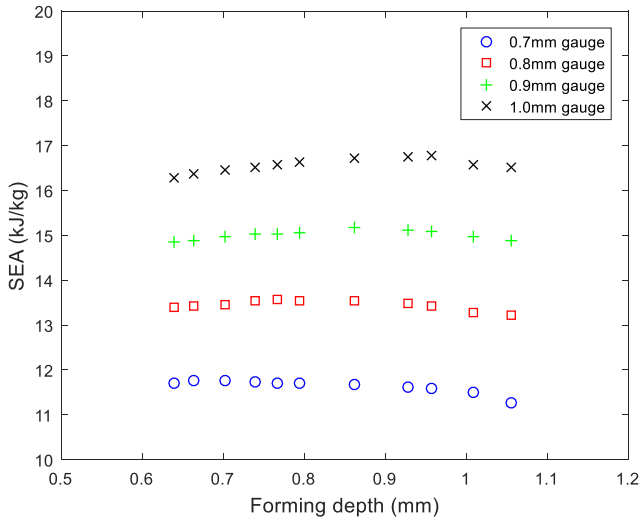

Fig. 5.11. SEA – forming depth (work hardening taken into account)

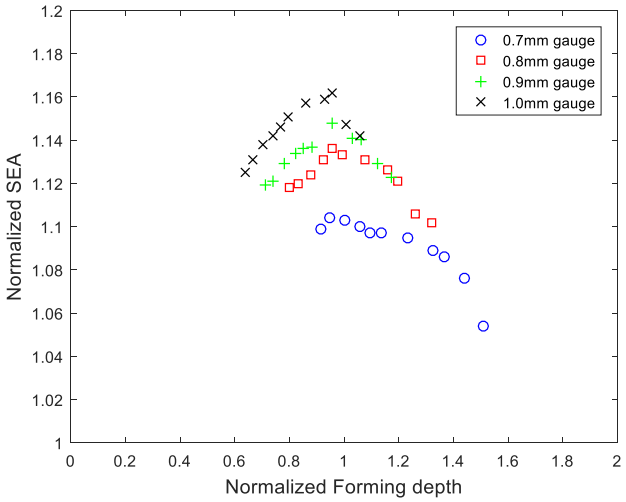

Fig. 5.12. Normalized SEA – Normalized forming depth (work hardening taken into account)

$$Normalized\ forming\ depth = \frac{Forming\ depth}{Gauge\ thickness} \tag{5.6}$$

5.5 Response of the dimpled columns to inclined axial impact loads

Although the response of thin-walled columns to perfectly axial impact loads (i.e. the impact face is perpendicular to the column's longitudinal direction and the impact velocity is along the column's longitudinal direction) is studied in most of research works, the impact loads are usually inclined to some extend in reality. Therefore, it is crucial to understand how differently the dimpled columns behave from the comparable plain ones under inclined axial impact loads. This section focuses on the response of dimpled columns to axial impact loads, where the impact surface is not perpendicular to the column's longitudinal direction and the impact velocity is directed along the longitudinal direction.

The loading conditions are illustrated in Fig. 5.13. The FE models used were quite similar with the ones introduced in section 5.2. Comparing with those models, the only modifications included:

- The geometry of the rigid impactor was changed by adding an inclined angle, as shown in Fig. 5.13. The inclined angle refers to the angle between the end surface of the column and the impact face. The range of the inclined angle in the present study is from 10 to 30 degrees. In the meantime, the mass of the impactor was kept constant by adjusting the length of the impactor.
- Columns with two different lengths (250 mm and 400 mm) were simulated to investigate the behaviour of columns with different slenderness ratios.

- Besides plain and dimpled samples, columns with dimpled geometry and plain material properties (DGPM) were simulated as well, in order to isolate the effect of material properties on the behaviour of columns.
- Full models were used instead of the simplified models with symmetric boundary conditions, due to the nature of the problem.

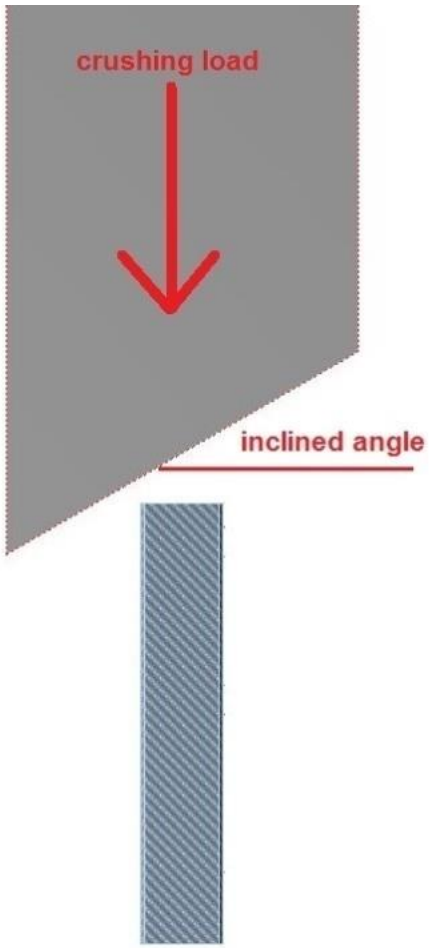

Fig. 5.13. Schematic plot of a dimpled column subjected to inclined axial impact load

From the numerical results, the following three failure modes were identified:

- Failure mode 1: regular folding. This failure mode was observed for inclined angles smaller than 16 degrees (plain) and 20 degrees (dimpled). Typical deformed shapes and energy absorbed – axial displacement curves of this failure mode are shown in Fig. 5.14. The folding mechanism and energy absorption performance are very similar to those under perfect axial impact loads.
- Failure mode 2: side sliding. The failure mode transforms from regular folding to side sliding as the inclined angle increasing. Typical deformed shapes and energy absorbed – axial displacement curves are shown in Fig. 5.15. Comparing to mode 1, the crushed part slides towards one side. Additionally, the energy absorbed is about 10% lower, because the plastic deformation in the highlighted region is not fully developed.
- Failure mode 3: global bending. This failure mode was observed for inclined angles larger than 26 degrees (250 mm) and 22 degrees (400 mm). In this failure mode, the bending component of the impact load is dominant due to the large inclined angle. The deformed shapes and energy absorbed – axial displacement curves are shown in Fig. 5.16. The most critical feature of this failure mode is that obvious plastic hinge emerged near the bottom end of the column, and afterwards the column did hardly absorb any more kinetic energy.

Therefore, in the events of collisions, the global bending failure mode should be avoided, and the regular folding failure mode is preferred for its relative high energy absorption capacity.

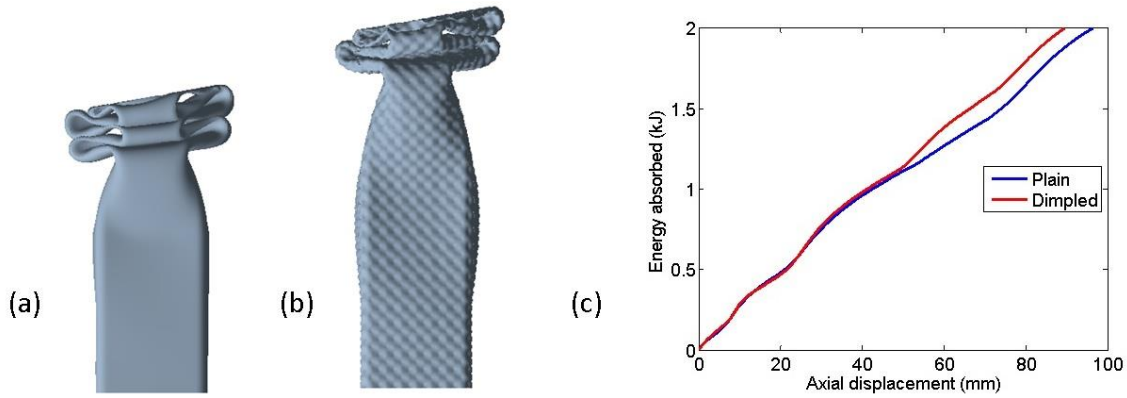

Fig. 5.14. The regular folding failure mode: (a) plain, (b) dimpled column deformed shape and (c) energy absorbed – axial displacement

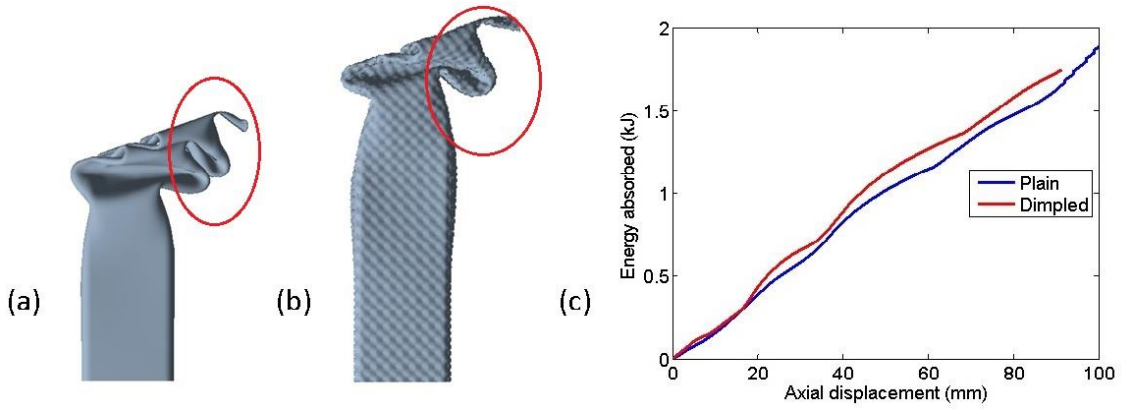

Fig. 5.15. The side sliding failure mode: (a) plain, (b) dimpled column deformed shape and (c) energy absorbed – axial displacement

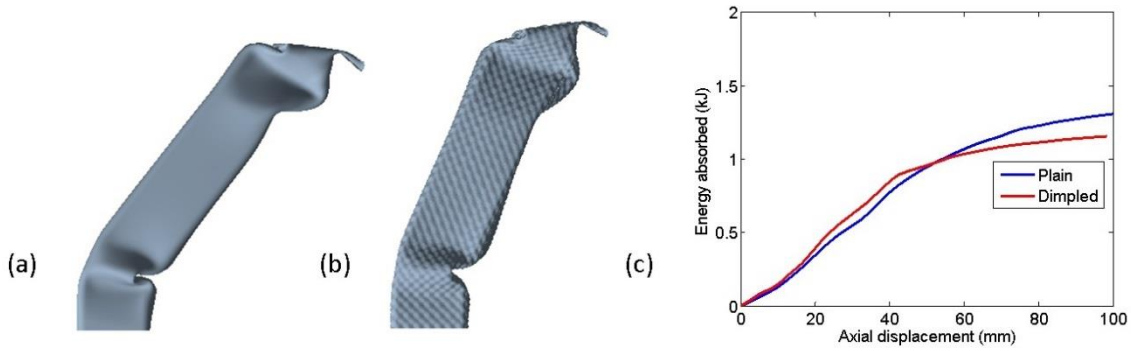

Fig. 5.16. The global bending failure mode: (a) plain, (b) dimpled column deformed shape and (c) energy absorbed – axial displacement

The crushing process was then simulated for plain and dimpled columns with various inclined angles. The failure modes are presented in Table 5.1. For the 250 mm long columns, the critical inclined angles from the regular folding mode to the side sliding mode of plain dimpled columns are 16 and 20 degrees, respectively, and the critical inclined angles from the side sliding mode to the global bending mode are 26 degrees for both columns. For the 400 mm long columns, the transformation from regular folding to side sliding does not significantly change, however, the global bending failure mode starts to appear at an inclined angle of 22 degrees, for both plain and dimpled samples. The results reveal that the dimpled columns perform better at resisting side sliding, while the performance at resisting global bending of plain and dimpled columns are similar, regardless of the columns' slenderness ratio.

Table 5.1. Failure modes of plain and dimpled columns

Material	**Dimensions (mm)**	**Inclined angle (degrees)**										
		10	12	14	16	18	20	22	24	26	28	30
Plain	46x46x250	1	1	1	2	2	2	2	2	3	3	3
Dimpled	46x46x250	1	1	1	1	1	2	2	2	3	3	3
Plain	46x46x400	1	1	1	2	2	2	3	3	3	3	3
Dimpled	46x46x400	1	1	1	1	1	2	3	3	3	3	3

5.6 Summary

In this chapter, simulations were carried out to analyse the response of thin-walled square hollow section plain and dimpled columns to axial impact loads. The FE method developed and validated in Chapters 3 and 4 was used. The

behaviour of dimpled columns was analysed and compared to the conventional plain counterparts. An optimization study was carried out to find out the forming depths for the optimal equivalent yield strengths and specific energy absorption values. The behaviour of dimpled and plain columns under inclined axial impact loads were studied as well. The following conclusions can be made from the study:

- When subjected to axial impact loads, layers of folds are progressively formed in the thin-walled square hollow section dimpled columns, which is similar to the failure mechanism of the plain ones. The SEA value has well converged after the third layer of folds is formed. However, unlike in plain columns, the folding wavelength in dimpled columns is not constant.
- The gauge thickness and forming depth of dimpled plate can significantly affect the energy absorption performance through the material properties pathway and the geometry pathway. These two factors were analysed individually as well as combined:
    - Yield strength of the dimpled plate does not always increase with the forming depth. It is essentially a trade-off between the work hardening and stress concentration effects. For 0.8, 1.0 and 1.2 mm gauge plates, the yield strengths reach their maximum values at approximately 1 mm forming depth.
    - The dimpled geometry factor standalone does not significantly influence the energy absorption performance, which is indicated by the SEA value. However, it can be observed that great forming depths have a negative influence on SEA.

  - Taking both the material properties factor and the dimpled geometry factor into account, the optimal forming depth is nearly proportional to the gauge thickness, in terms of the SEA values. The SEA of 1 mm gauge dimpled columns is up to 16.3% higher than the plain counterparts.

- When subjected to inclined axial impact loads, three failure modes can be observed for plain and dimpled columns: regular folding, side sliding and global bending. Comparing to plain columns, dimpled columns have better resistance against side sliding. The resistance against global bending of the two types of columns are similar.

Chapter 6 Design and numerical analysis of the innovative dimpled thin-walled structures for improved crashworthiness

6.1 Introduction

In recent years, improving energy absorption performance (crashworthiness) has become a popular research area. A number of strategies have been proposed, to achieve the goal of increasing either the mean crushing force or the specific energy absorption (SEA). As introduced in Chapter 2, mainstream designs include introducing multi-corner, multi-cell, material-filled, etc.

This chapter aims to improve the energy absorption performance of dimpled columns by introducing an innovative design features, namely extra layers of columns. To achieve this aim, FE simulations are run to predict the interaction between multiple layers of dimpled steel plates, and the energy absorption performance of multi-layer plain and dimpled columns. The effects of a series of parameters are further analysed, for the purpose of optimizing the design. The main objectives of this chapter include:

- Identifying the mechanism of the interaction between two dimpled plates.
- Developing a mathematical model to characterise the interaction between two dimpled plates, and understanding the difference from the plain counterparts.

- Understanding the difference between plain and dimpled multi-layer thin-walled structures subjected to axial crushing loads.
- Understanding the effects of a series of factors that may influence the energy absorption performance of multi-layer thin-walled structures.

6.2 The interaction between two dimpled plates

It has been previously reported that the interaction between materials may contribute to improving the energy absorption performance. The interaction between dimpled plates is expected to be more significant than the plain counterparts, due to the wavy geometry. Therefore, understanding the fundamental mechanisms and characteristics of the interaction between two dimpled plates is crucial. In this section, the interaction between two dimpled plates is investigated.

6.2.1 FE modelling

When two plain plates are relatively sliding, the most commonly adopted method to predict the interaction is the Coulomb's law, as shown in Eq. 6.1, where F represents the static frictional force, or the minimum force required to initiate the relative sliding, μ represents the friction coefficient between the two plates, and N represents the normal pressing force.

$$F = \mu N \tag{6.1}$$

Similarly, the variable ‘effective friction coefficient’, as defined in Eq. 6.2, was employed in the present study to describe the relative sliding of two dimpled plates.

$$\mu_e = {}^{F}/_{N} \tag{6.2}$$

To obtain the values of μ_e, quasi-static simulations were run, using ANSYS Mechanical APDL. The finite element model is shown in Fig. 6.1. Similar to the FE method described in Chapter 3, model for only one dimpled section was built and symmetric boundary conditions were applied. The material properties, element types and sizes were identical to those in section 3.4.1. Additionally, ANSYS contact 173 and target 170 elements were generated on the lower surface of the upper plate and the upper surface of the lower plate. The following loading and boundary conditions were applied in the FE model:

(1) DOF in y-axis of the four mid-points on the bottom surface of the lower plate was constrained, representing the support from the object below the lower plate.
(2) DOF in x-axis of all the nodes on side faces D and E and their opposite faces was constrained, representing the symmetry in x-direction of the upper and lower dimpled plates.
(3) DOF in z-axis of all the nodes on face B and its opposite face was constrained, representing the symmetry in z-direction of the lower plate.
(4) A uniform normal pressure was applied across surface A.
(5) A displacement of 3.32 mm along z-axis was applied on all the nodes on face C.

Additionally, a constant Coulomb's friction coefficient of 0.3 was used as the baseline.

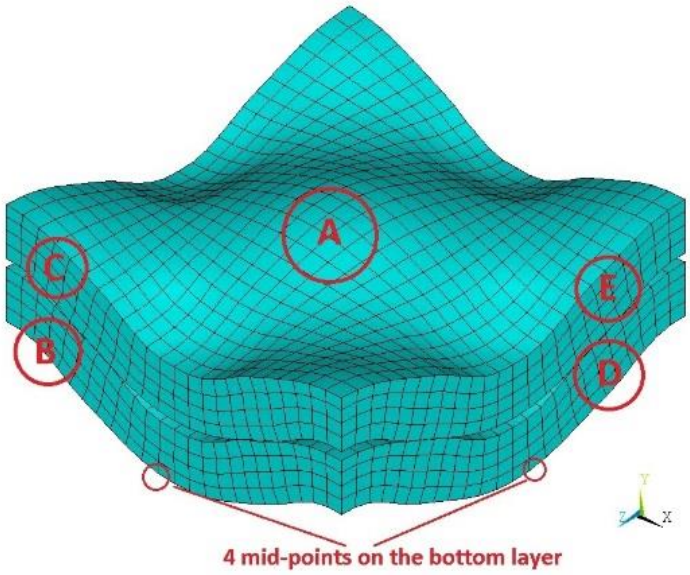

Fig. 6.1. Isometric view of the FE model

6.2.2 The interaction mechanisms

It has been mentioned in Chapter 3 that the thickness of the dimpled plates is non-uniform. As a result, contact between the two dimpled plates only occurred around the slope region, as shown in Fig. 6.2. It can be seen that there is an angle between the contact surface and the horizontal plane. As a result, unlike the plain plates, the effective friction coefficient μ_e is not constant when the upper plate is being pulled along the z-direction. The pattern of the effective friction coefficient varying against the relative movement is displayed in Fig. 6.3. Three stages were identified. In stage 1, μ_e increases with the relative movement and converges when the relative movement reaches approximately 0.002 mm. In stage 2, μ_e remains at almost a constant value. In stage 3, μ_e drops as the

relative movement increasing. The variation of μ_e in stage 1 is not analysed in this study, because the corresponding relative movement is smaller than the usual tolerance in the engineering applications of the dimpled structures. The transition from stage 2 to 3 is due to the change in the contact angle. The deformed shapes at points (A), (B) and (C) in Fig. 6.3(a) are presented in Fig. 6.4. The decreasing contact angle has reduced the pulling force required to move the upper plate, which subsequently reduces the effective friction coefficient. It has been noticed that the stress concentration effect causes high stress levels around the contact region, which may potentially result in material failure. The von-Mises stresses displayed in Fig. 6.4 are obtained when the normal pressure was 1 MPa, which exceeds the operating limit in the actual applications of the dimpled products. However, the maximum von-Mises stress still has not reached the material's yielding point. Therefore, the stress concentration will not cause any material failure in reality.

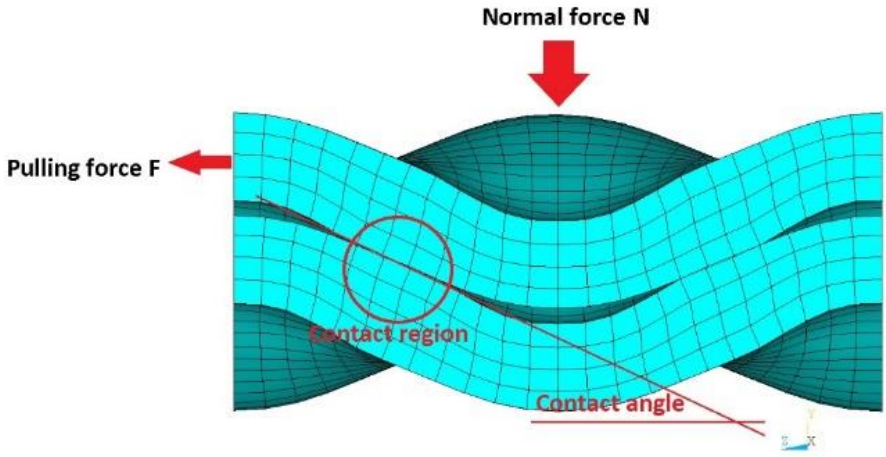

Fig. 6.2. Side view of the FE model

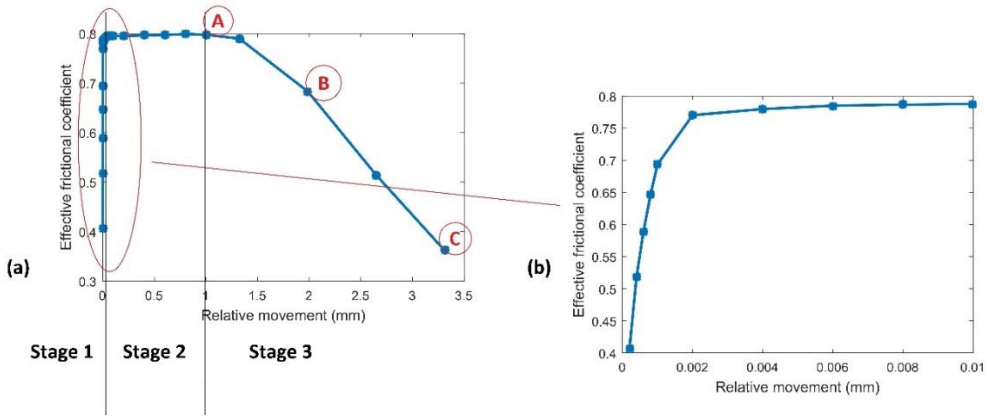

Fig. 6.3. (a) Pattern of the effective friction coefficient – relative movement and its (b) locally enlarged view

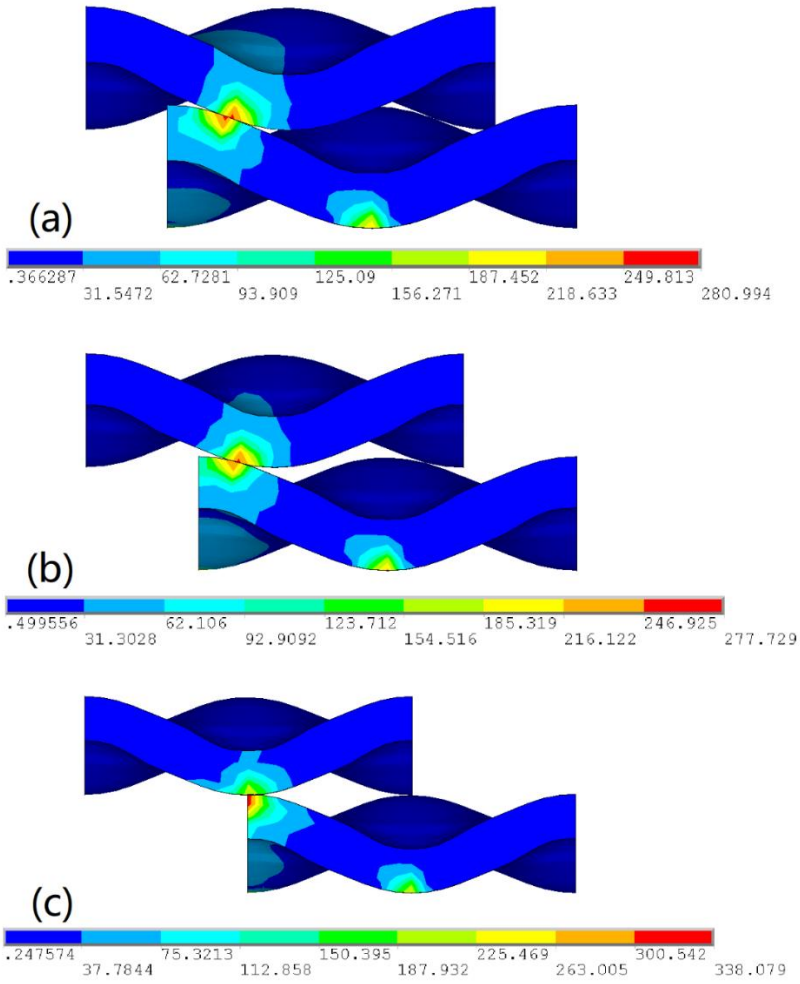

Fig. 6.4. Deformed shapes and von-Mises stress at (a) point A, (b) point B and (c) point C in Fig. 6.3.

6.2.3 Prediction of the equivalent friction coefficient

A series of simulations were run under different conditions, aiming to establish an empirical equation to predict the equivalent friction coefficient μ_e at the steady stage (stage 2). Factors that can possibly affect μ_e include:

(1) The geometry of dimpled plates, however, this will not be discussed in this thesis because only one dimple is analysed.
(2) The actual friction coefficient μ of the material. This value may change when the dimpling forming process is applied on other materials such as aluminium and stainless steel.
(3) The normal force N applied on the plate. However, simulations were performed under the normal force from 5 to 50 N, and the effective friction coefficient μ_e was found to be independent from the normal force.

The actual friction coefficient μ was initially set to be from 0 to 1. The range covers most of materials and some extreme conditions. The effective friction coefficients are shown in Fig. 6.5. It was observed that the relation between μ_e and μ is close to quadratic. Therefore, the expression for μ_e can be written as Eq. 6.3.

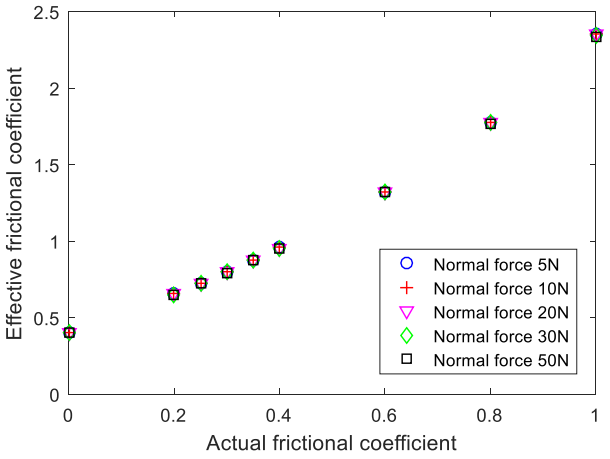

Fig. 6.5. $\mu_e - \mu$ relations under various normal forces

$$\mu_e = a\mu^2 + b\mu + c \tag{6.3}$$

Quadratic curve fitting was carried out using the Matlab curve fitting tool. The result for the quadratic fitting is shown in Fig. 6.6. It was found that the quadratic fitting can capture the trend of the data points very well. The output parameters were $a = 0.9589$, $b = 0.9564$, and c$= 0.4163$. By substituting these values into Eq. 6.3, the effective friction coefficient can be calculated using Eq. 6.4.

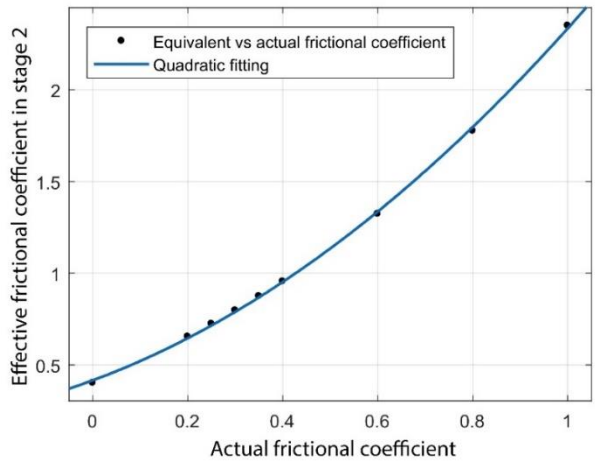

Fig. 6.6. Quadratic fitting for the equivalent friction coefficient

$$\mu_e = 0.9589\mu^2 + 0.9564\mu + 0.4163 \tag{6.4}$$

6.3 Numerical parametric study on dimpled multi-layer structures

6.3.1 FE modelling

The FE models of the plain and dimpled multi-layer columns are similar to those used in previous chapters. Fig. 6.7 shows a typical example of the double-layer dimpled column. In the FE model, all the FE modelling details except for the geometries and the initial velocity of impactor are identical to those in section section 5.2. The ends of both inner and outer columns are fully fixed. The 250.89 kg rigid impactor has an initial velocity of 10 m/s along z-axis, with DOFs in x and y directions restrained. The element sizes are 1 mm and 0.55 mm for the plain and dimpled models, respectively. The Cowper-Symonds material model was employed to characterise the strain-rate sensitivity of the material. A Coulomb friction coefficient of 0.3 and a gap size of 2.17 mm were used as the baseline, where the gap size is defined as the distance between the neutral planes of the dimpled walls, as illustrated in Fig. 6.8.

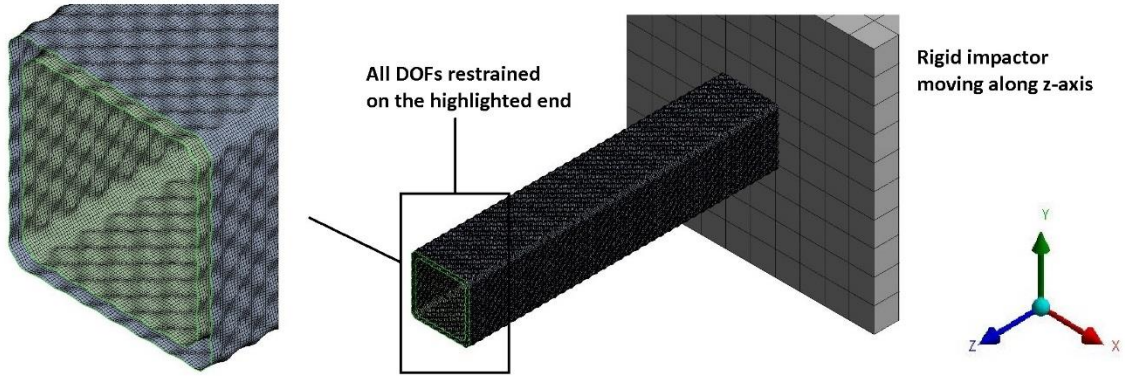

Fig. 6.7. FE model of the double layer dimpled columns

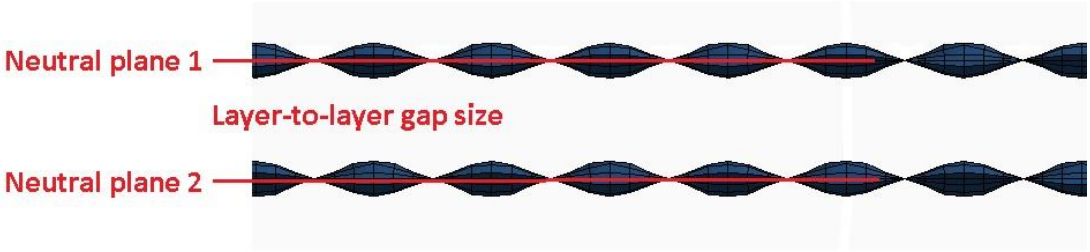

Fig. 6.8. Illustration of the layer-to-layer gap size

6.3.2 Results and discussions

The baseline results were analysed first. When analysing the results, four data sets were analysed as a group under each condition. The four data sets were:

- The outer layer column standalone.
- The inner layer column standalone.
- The outer layer and the inner layer without interaction.
- The double layer columns with interaction.

Comparisons were made mainly between the third and fourth data sets, where the difference can be considered to be caused by the interaction between the inner and outer walls.

The crushing forces and energy absorbed curves for the baseline plain and dimpled columns are shown in Figs 6.9 and 6.10, respectively. Fig. 6.9(a) shows that the crushing force patterns of the plain double-wall columns and summation of the two individual columns are very close, and the waveforms are matched, especially after the progressive buckling has stabilized. By contrast, the crushing force patterns for the dimpled double-wall columns do not agree with the one of

the individual columns added up. This difference between the plain and dimpled columns can be found under other test conditions, too. This phenomenon reveals that unlike in plain columns, introducing extra layers in dimpled columns will result in significant shifting in the crushing force patterns due to the interaction between layers. Additionally, neither layer dominated the crushing process of the dimpled double-wall columns. Therefore, the historical crushing force of the double-wall dimpled columns cannot be predicted using an analytical approach. In terms of energy absorption capability, the difference between the double-wall columns and the summation of two individual columns is below 5% for plain as well as dimpled columns, which implies that the work done by the interaction is not significant.

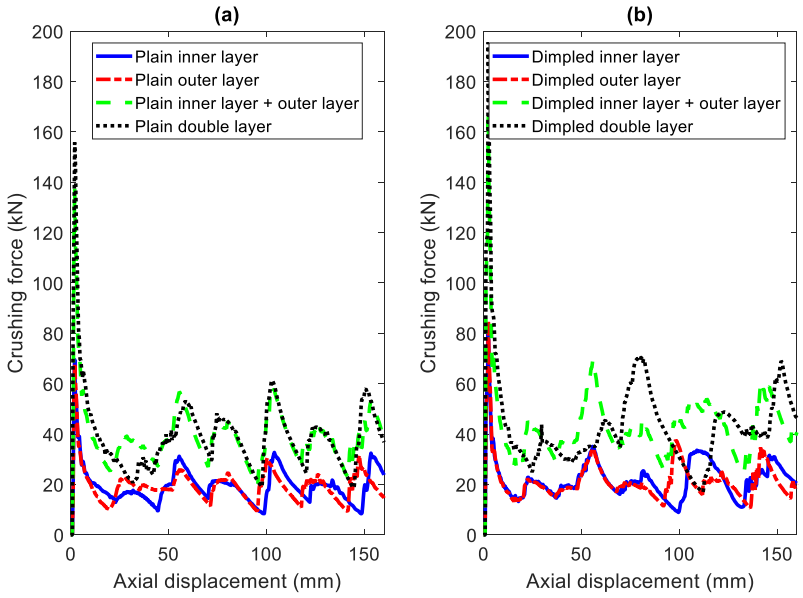

Fig. 6.9. Crushing force – axial displacement curves for the baseline (a) plain and (b) dimpled columns

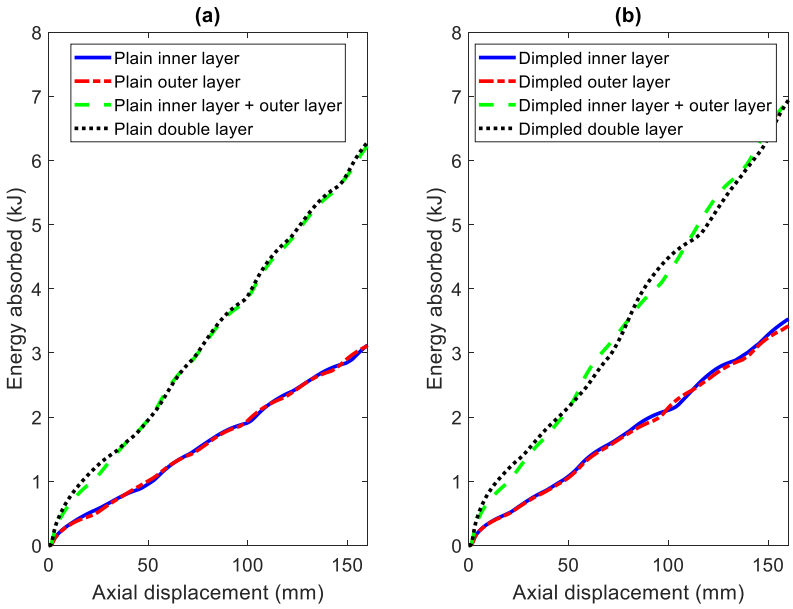

Fig. 6.10. Energy absorbed – axial displacement curves for the baseline (a) plain and (b) dimpled columns

To understand the interaction between layers, the numerical study was extended by carrying out a parametric study on the three factors below:

- The actual friction coefficient μ of the material.
- Number of layers.
- Gap size between layers.

Fig. 6.11 shows the variation of the mean crushing force and the normalized mean crushing force against the actual friction coefficient for plain and dimpled double layer columns, where the normalized mean force is defined in Eq. 6.5 and used to represent the extra energy absorbed due to the layer-to-layer interaction. Large friction coefficients were used to artificially exaggerate the effects of the layer-to-layer interaction. As the friction coefficient increasing from 0.3 to 1, the

normalized mean force increases from 0.989 to 1.042 for dimpled columns, and remains nearly constant for plain columns. It reveals that greater friction coefficients result in a noticeable increase in the normalized mean force of dimpled double-wall columns, while the effect of friction coefficients on the plain double-wall columns may be neglected comparing to their dimpled counterparts. Therefore, the layer-to-layer interaction can be considered to be more significant in dimpled double-wall columns than in plain ones.

$$Normalized\ mean\ force = \frac{Mean\ force\ of\ the\ multi\ layer\ column}{Sum\ of\ the\ mean\ forces\ of\ the\ single\ layer\ columns} \quad (6.5)$$

Similar simulations were then performed on the triple-wall and quad-wall plain and dimpled columns. As shown in Fig. 6.12 (d) and (f), the normalized mean crushing forces considerably increase with the friction coefficient in triple-wall and quad-wall dimpled columns. By contrast, it can be found that the energy absorption performance of plain columns is insensitive to the actual friction coefficient. Furthermore, by comparing the results presented in Fig. 6.12 (b), (d) and (f), it can be seen that introducing more layers in the thin-walled columns can promote the layer-to-layer interaction, especially in the dimpled columns.

The last parameter analysed is the layer-to-layer gap size. Fig. 6.13 shows the variation of normalized mean force against the gap size with two different friction coefficients specified (μ =0.3 and 1). For plain and dimpled columns, with either friction coefficient applied, the normalized mean force only varies within a negligible range as the layer-to-layer gap size increasing. Therefore, the gap size does not appear to be influencing the interaction between layers.

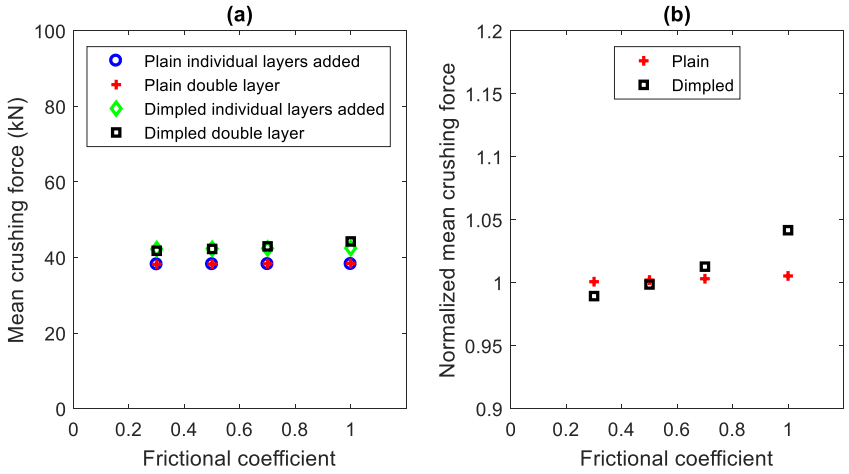

Fig. 6.11. (a) Mean forces and (b) Normalized mean forces – friction coefficient of the double layer plain and dimpled columns

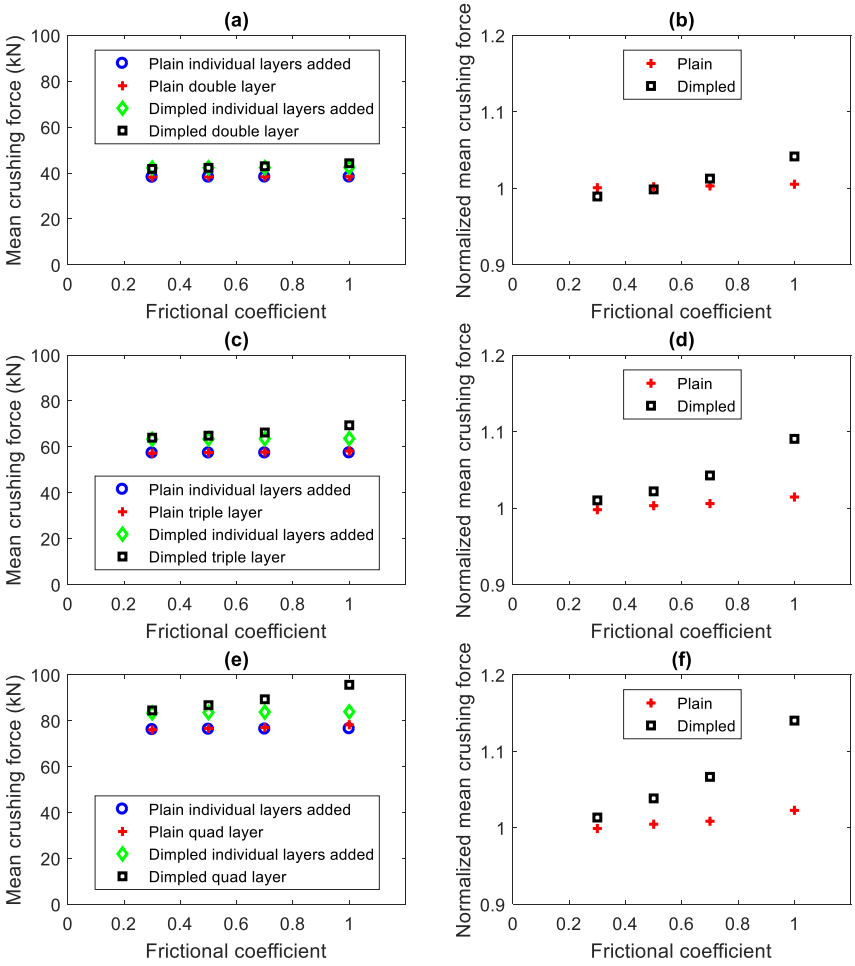

Fig. 6.12. Mean forces and normalized mean forces – friction coefficient of the (a, b) double layer, (c, d) triple layer and (e, f) quad layer columns

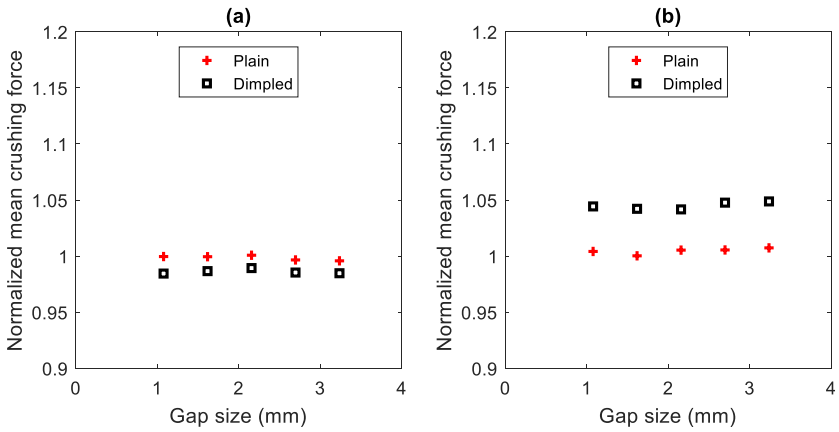

Fig. 6.13. Normalized mean force – gap size in the double layer columns with (a) μ =0.3 and (b) μ =1

6.4 Summary

In this chapter, a series of quasi-static and explicit dynamic simulations were performed to study the interlocking mechanism of the dimpled plates and the response of multi-layer plain and dimpled columns to axial impact loads. In the quasi-static simulations, the FE model was created based on two single-dimple sized square shape plates. The variable equivalent friction coefficient was employed to characterise the relative sliding between two dimpled plates. In the explicit simulations, the FE models used were similar to those in Chapters 4 and 5. The variable normalized mean force was introduced to describe the improvement in energy absorption performance due to the layer-to-layer interaction. The behaviour of plain and dimpled multi-layer columns under axial impact loads were compared, and the influence of a series of parameters on the multi-layer columns' energy absorption performance were studied as well. From the study, the following conclusions can be made:

- As two dimpled plates relatively sliding, there is a three-stage variation of the equivalent friction coefficient μ_e. The first stage can be neglected due to its brief presence. μ_e remains constant in the second stage, and drops in the third stage. The drop of μ_e in the third stage is due to the decrement in contact angle.
- The equivalent friction coefficient μ_e is dependent on the geometry of the dimpled plates and the actual friction coefficient of the material. A parametric study with respect to the actual friction coefficient was performed and an empirical equation was therefore obtained. The relation between the equivalent and actual friction coefficients can be considered as quadratic.
- Extra layers were introduced in the plain and dimpled columns for the purpose of improving their resistance to axial impact loads. Unlike in plain columns, introducing extra layers in dimpled columns causes the crushing force patterns to shift, which cannot be analytically predicted.
- Comparing to plain columns, the energy absorption performance of dimpled columns is more sensitive to the friction coefficient, which implies that the interaction between layers is more significant in dimpled multi-layer thin-walled columns. The interaction can be promoted by introducing more layers of columns. A parametric study on the layer-to-layer gap size reveals that its influence on the energy absorption performance may be neglected.

Chapter 7 Numerical prediction of the response of dimpled structural components to lateral impact loads

7.1 Introduction

Hollow tubular members are widely used in many infrastructures and vehicular systems. As introduced in Chapter 2, the hollow tubular members are prone to transverse impact loading. For example, bumpers and B-pillars of vehicles are under transverse impact loads in the events of collision. Therefore, the structural components' capability of absorbing lateral impact energy is critical to ensure the safety of passengers and infrastructures.

This chapter focuses on the energy absorption characteristics of dimpled thin-walled columns subjected to lateral impact loads. The aim of this chapter is to investigate the response of dimpled columns to lateral impact loads. To achieve this aim, simulations are run based on the FE models validated in Chapters 3, 4 and 5. Comparisons are made among plain columns, dimpled columns, and columns with dimpled geometry and plain material properties (DGPM) throughout this chapter. Analysis on the support conditions of the columns are carried out as well. The main objectives of this chapter are:

- Validating whether the previously developed FE method can be used to predict the response of dimpled columns subjected to lateral impact loads.
- Understanding the failure mechanism and characteristics of dimpled columns under lateral impact loads.

- Comparing the responses of plain, dimpled and DGPM columns to lateral impact loads in terms of the failure mechanism and energy absorption performance.
- Understanding the effects of the dimpled geometry, and therefore identifying the significance and advantages of introducing the dimpled geometry in structural components.
- Understanding the effects of pre-axial compressive loads.
- Investigating the effects of different support conditions.
- Based on the findings, identifying the potential engineering applications which are suitable for the dimpled columns.

7.2 FE modelling and validations

Similar to the simulations in Chapters 4, 5 and 6, the explicit dynamics FE code integrated in ANSYS Workbench 17.1 was used to predict the columns' response to lateral impact loads. All the key features, including material properties, element details, contact method, friction coefficient and sheet thickness factor, are the same as introduced in section 4.2.2.1, which has already been validated. However, it should be noted that the boundary conditions are considerably different from previous simulations. Therefore, further validations are required. To validate the FE modelling method, the experimental and numerical tests carried out by Zeinoddini et al. [66, 67] were reproduced, because the case studied by Zeinoddini et al. [66, 67] is very similar to the case studied in this chapter. Fig. 7.1 shows the FE model to reproduce the experimental and

numerical studies conducted by Zeinoddini et al. [66, 67]. The boundary conditions and dimensions of the model are:

(1) The column has a circular thin-walled section, a length of 1 m, an outer radius of 50 mm and a thickness of 2 mm.

(2) One end of the column is fully fixed.

(3) Constant axial compressive load of 0 or 50% of the column's squash load along the z-axis is applied on the other end of the column.

(4) The solid impactor has a mass of 25.6 kg and an initial velocity of 7 m/s along the –y direction.

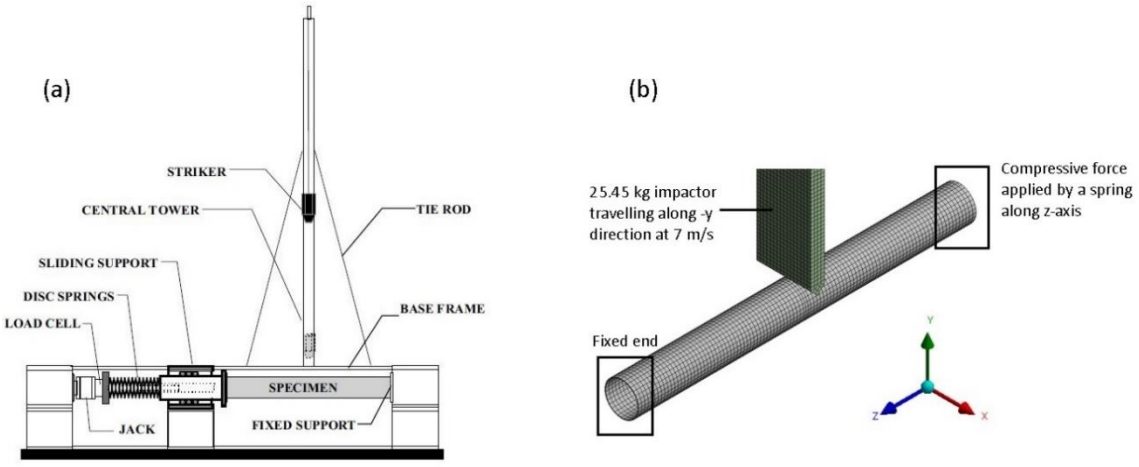

Fig. 7.1. (a) Schematic plot of the experimental setup [66] and (b) FE model used in the present study

After the instant that the axial compressive load is solely applied and before the impact starts, stress waves will propagate along the column and reach a steady state. This process is reflected in the simulations by allowing sufficient time between the axial compressive load being applied and the impact contact being

initiated. An example of the steady-state von-Mises stress distribution prior to the impact is shown in Fig. 7.2.

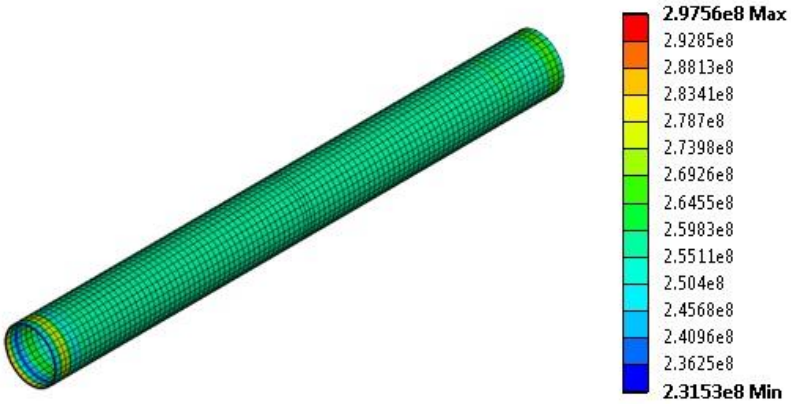

Fig. 7.2. Von-Mises stress (MPa) distribution in the column prior to the impact

To validate the FE method, results were compared under two axial compressive loads. Figs. 7.3 and 7.4 show the numerical and experimental final deformed shapes and the historical impact forces, when the axial compressive loads are 0 and 50% of the column's squash load, respectively. These two loading conditions were selected because of the availability of the published results. For each loading condition, comparison was made among the Zeinoddini's experimental results, Zeinoddini's numerical results, and the numerical results obtained in this study [66, 67]. As shown in Figs. 7.3 and 7.4, in both cases, good agreement between experimental and numerical results can be found in terms of the impact forces and deformed shapes. Therefore, the FE method was validated and can be used to accurately predict the columns' response to lateral impact loads.

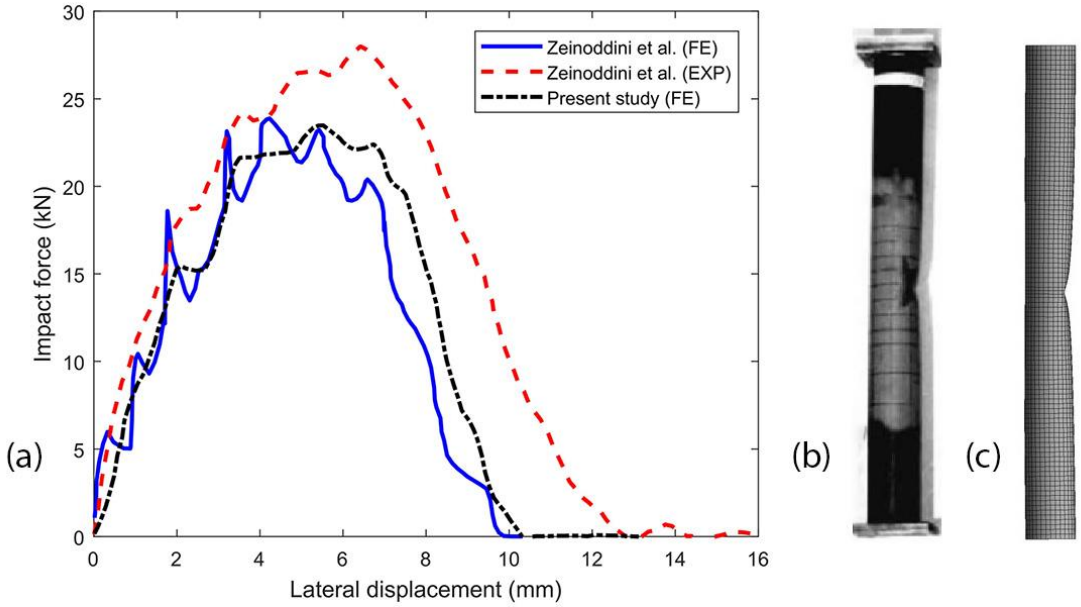

Fig. 7.3. (a) Numerical and experimental impact forces, (b) Experimental deformed shape and (c) Numerical deformed shape when the axial force is 0

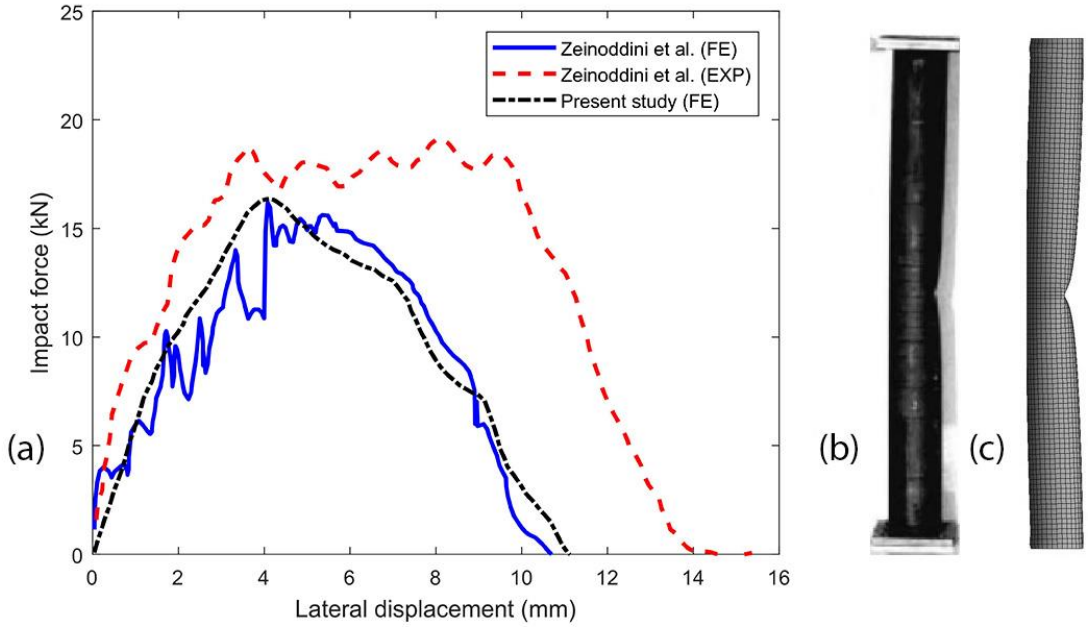

Fig. 7.4. (a) Numerical and experimental impact forces, (b) Experimental deformed shape and (c) Numerical deformed shape when the axial force is 50% of the squash load

7.3 Energy absorption of dimpled columns under lateral impact loads

Square hollow section (SHS) columns were adopted in this study. This chapter focuses on a typical support condition (one end fixed and the other end roller supported with axial compressive loads applied), while other support conditions will be analysed in Section 7.4. Other factors including the impact loading conditions and gauge thickness of columns were kept to be identical in this section. The effects of axial compressive loads on energy absorption were studied.

7.3.1 FE modelling details

The SHS columns adopted in the present study are 500 mm long and 33 mm wide. The actual thickness is 1 mm for plain column walls and 0.959 mm for dimpled column walls, due to the stretched surface after the forming process. As shown in Fig. 7.5, the columns are fully fixed at one end and roller supported at the other end. To represent this support condition, all DOFs of the fully fixed end are constrained, while translational DOFs of the other end are constrained along x and y directions. The external loads consist of two parts:

(1) The first part is a quasi-static constant axial compressive load applied on the roller supported end along z-axis. When selecting the axial compressive loads, it was ensured that the column will neither buckle nor yield solely under the axial compressive load. Constant quasi-static axial compressive load was applied throughout the entire simulated duration.

(2) The second part of the external loads is the impact load from a 4.9 kg impact mass with an initial velocity of 8 m/s along y-axis (i.e. the impact energy is 156.8 J). The initial contact location is the mid-span of the column.

The impactor was considered as a rigid body and translational DOFs of the impact mass were constrained along x and z directions to represent the impact mass sliding along a straight trajectory. Sufficient time was allowed prior to the impact to ensure that the internal stress has stabilized. Symmetric boundary conditions were applied to the FE model along the axial direction (i.e. the symmetrical plane is the yz plane).

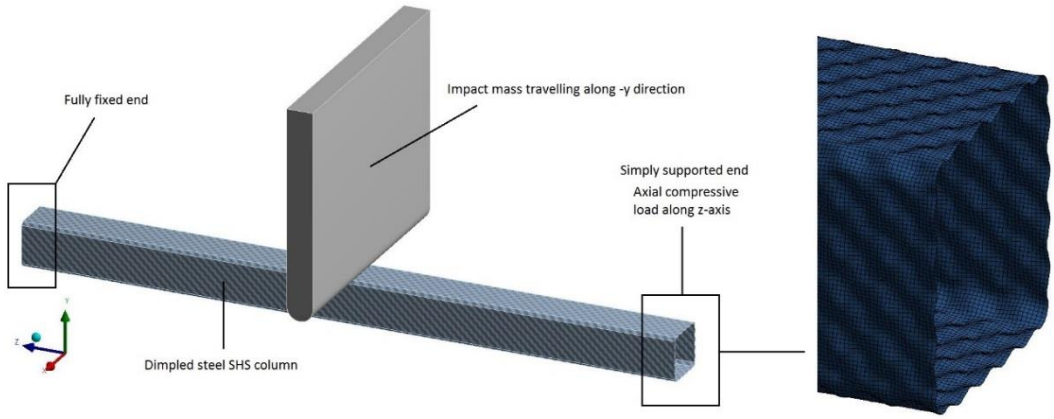

Fig. 7.5. FE model of the dimpled column and impact mass

7.3.2 The failure mechanism of dimpled columns under lateral impact loads

The typical impact force – lateral displacement curves for plain, dimpled and DGPM columns are shown in Fig. 7.6. The results presented are obtained under the axial compressive load of 6 kN. Similar patterns can be obtained under greater or smaller axial compressive loads. The purpose of adding the DGPM

samples is to eliminate the effects of material properties and therefore isolate the effects of the dimpled geometry.

As shown in Fig. 7.6, for plain columns, three peak forces can be observed before the residual force phase. However, for dimpled and DGPM columns, the 1st peak force is not very distinct and therefore may be neglected. The deformed shapes and equivalent plastic strains for the dimpled column at the 1st peak force, 2nd peak force, the maximum peak force and residual force phases are shown in Fig. 7.7. Models presented in Fig. 7.7 have been simplified by applying symmetrical boundary conditions. The 1st peak force appears when the contact between impactor and column starts. The 2nd peak force appears while the hinge at the impact location develops. The maximum peak force appears when the buckling around the fixed end initiates. The global failure modes for plain, dimpled and DGPM columns are similar.

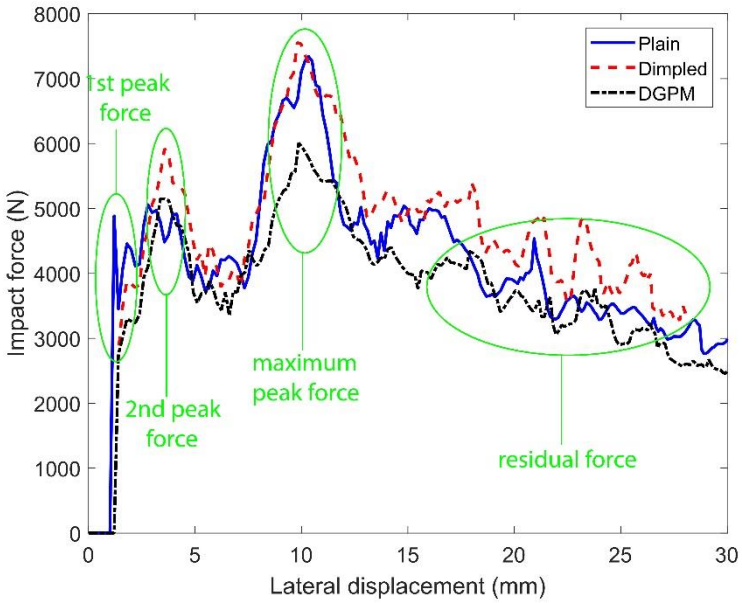

Fig. 7.6. Typical impact force – lateral displacement patterns

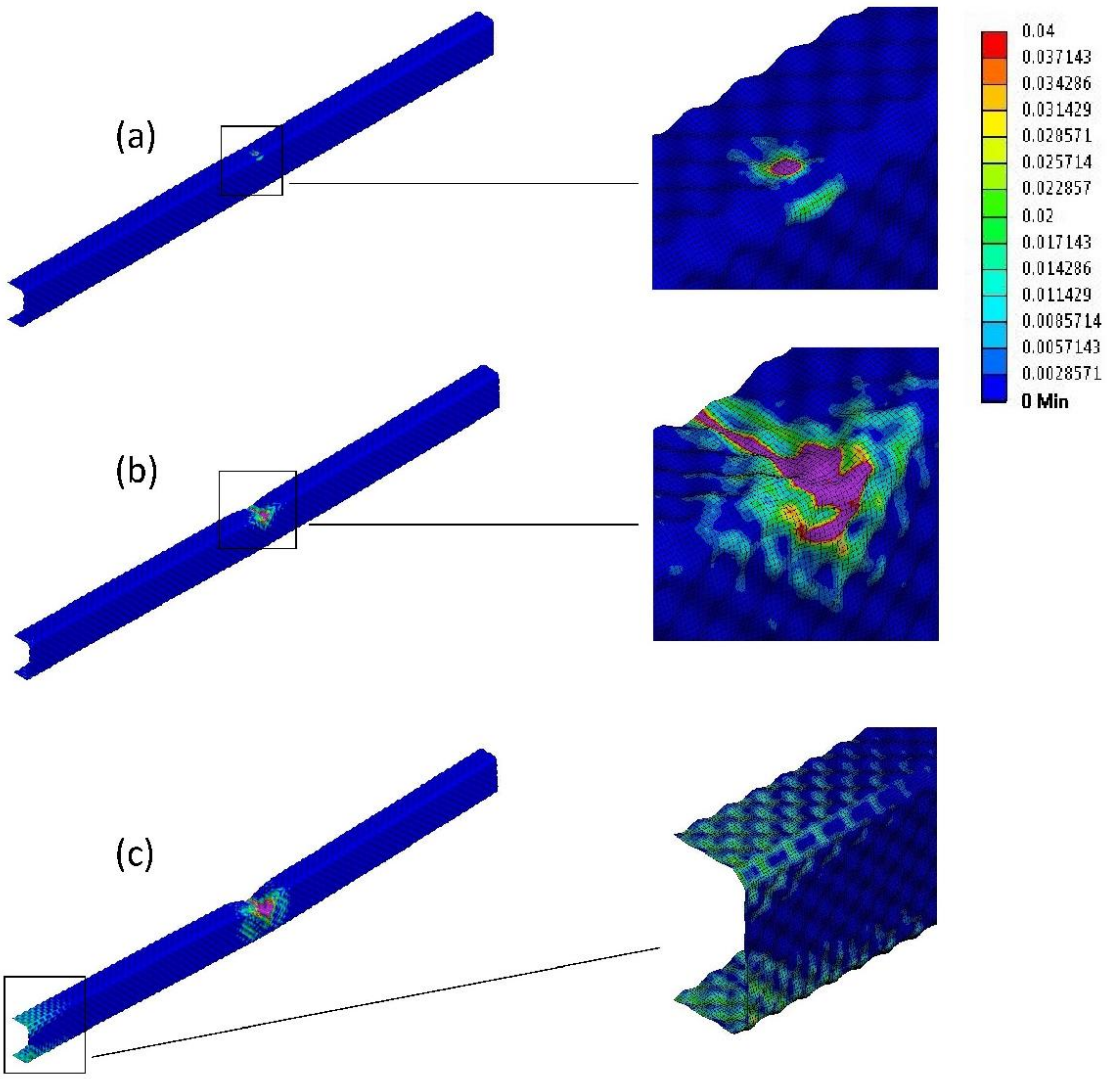

Fig. 7.7. Deformed shapes and equivalent plastic strains of the dimpled column at (a) 1st peak force, (b) 2nd peak force and (c) maximum force

The patterns of equivalent plastic strain distributions for dimpled and DGPM columns are similar to each other, but considerably different from the plain column. In dimpled and DGPM columns, the yielding effect is more concentrated. As shown in Fig. 7.8, when the 1st peak force appears, the surface area of the yielded region is about 160 mm^2 in the plain column, 51.4 mm^2 in the comparable dimpled column and 53.2 in the comparable DGPM column. When the maximum

impact force appears, comparing to the continuous and smooth strain distribution near the fixed end in the plain column, as shown in Fig. 7.9, the strain is distributed along the diagonal direction of dimples in dimpled and DGPM columns, as shown in Fig. 7.7(c).

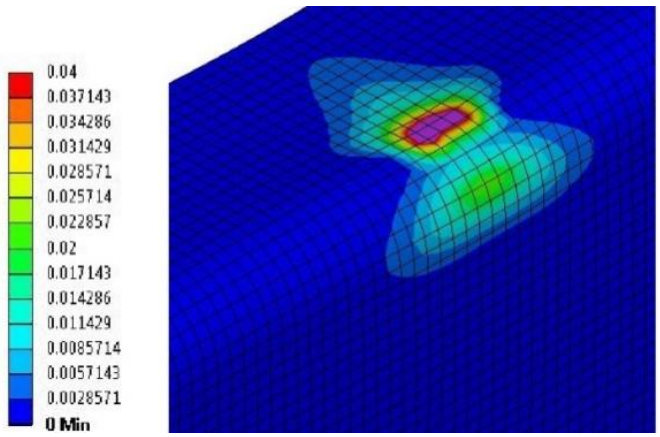

Fig. 7.8. Plastic strain near the impact location of the plain column at the 1st peak force

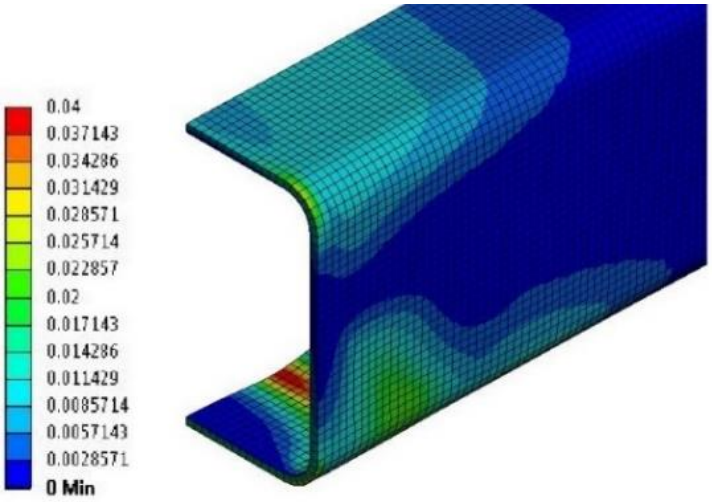

Fig. 7.9. Plastic strain near the fixed end of the plain column at the maximum peak force

7.3.3 Effects of axial compressive loads

In most engineering applications, lower maximum impact forces are usually preferred to reduce the damage to passengers or infrastructures, while greater mean impact forces are usually preferred for high energy absorption capacity. Therefore, the crush efficiency η_c, as defined in Eq. 7.1, was employed to evaluate the energy absorption performance of the columns in this chapter.

$$\eta_c = {}^{P_{mean}}/_{P_{max}} \tag{7.1}$$

The variations of mean force, peak force, 2nd peak force and crush efficiency against the axial compressive load are shown in Figs. 7.10 to 7.13, respectively. As shown in Fig. 7.10, the mean impact forces drop as the axial compressive load increasing. Dimpled columns have greater resistance than the plain and DGPM counterparts. The mean forces of plain and DGPM columns are not significantly different, which reveals that the dimpled geometry does not significantly influence the mean impact force, especially under greater compressive loads. The dimpled columns' mean forces are up to 32.6% and 34.0% greater than those of the comparable plain and DGPM columns, respectively, mainly due to the increased yield strength. Fig. 7.11 reveals that the dimpled columns' peak impact forces are slightly greater than the plain columns' and significantly greater than the DGPM columns'. The comparison between plain and DGPM samples reveals that the dimpled geometry reduces the peak impact forces by up to 20.6%. The reason is that the peak force appears when yielding initiates near the fixed end, and the dimpled geometry causes slowly-developed yielding effect near the fixed end, as described in Section 7.3.2. Fig. 7.12 suggests that the 2nd peak forces are not significantly influenced by axial compressive loads. Additionally, the dimpled

geometry does not appear to affect the 2nd peak force, either. Fig. 7.13 shows the variation of crush efficiency against compressive loads, which is a combined result of the mean impact force and peak impact force. It can be found that the dimpled geometry causes an increment between 12.6% and 20.4% in terms of crush efficiency, mainly due to the reduced peak impact force.

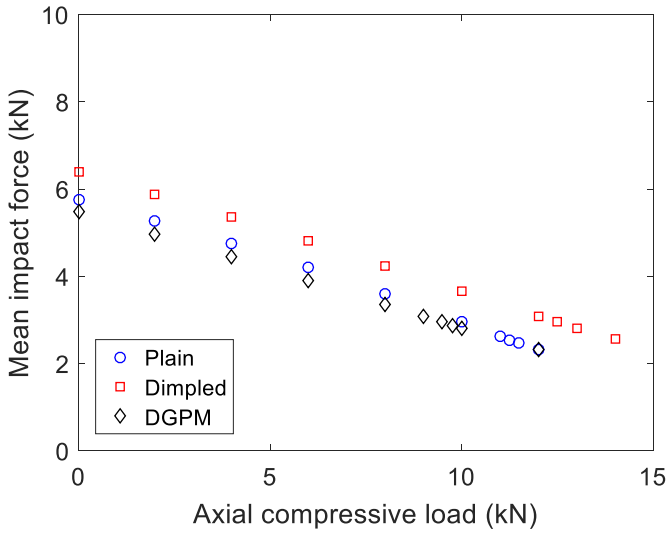

Fig. 7.10. Mean impact force under different axial compressive loads

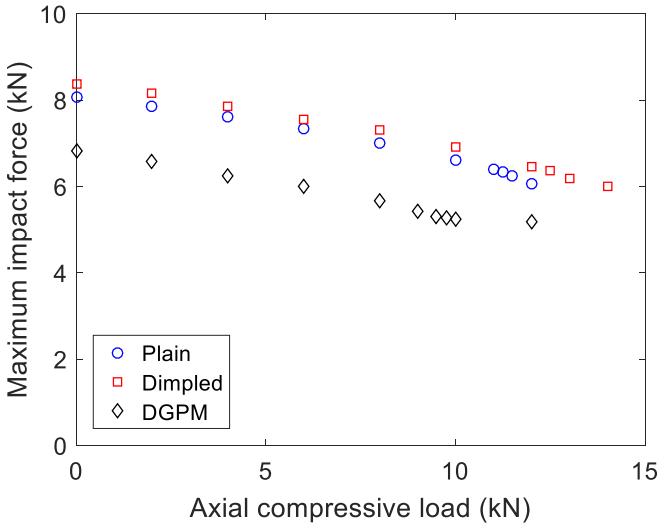

Fig. 7.11. Maximum peak force under different axial compressive loads

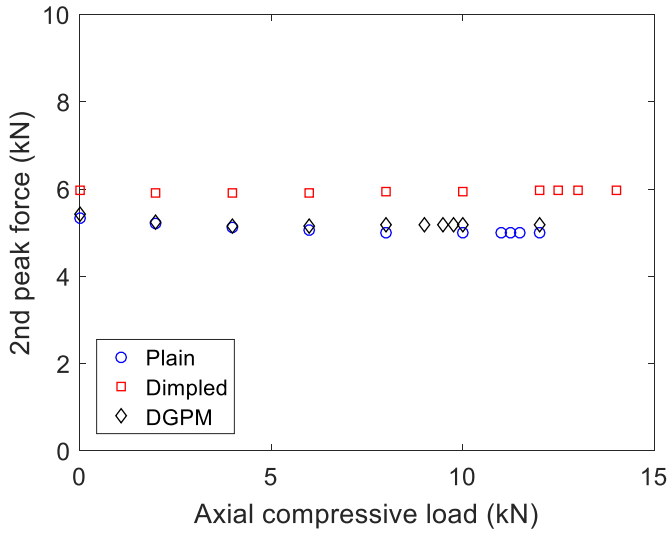

Fig. 7.12. 2nd peak force under different axial compressive loads

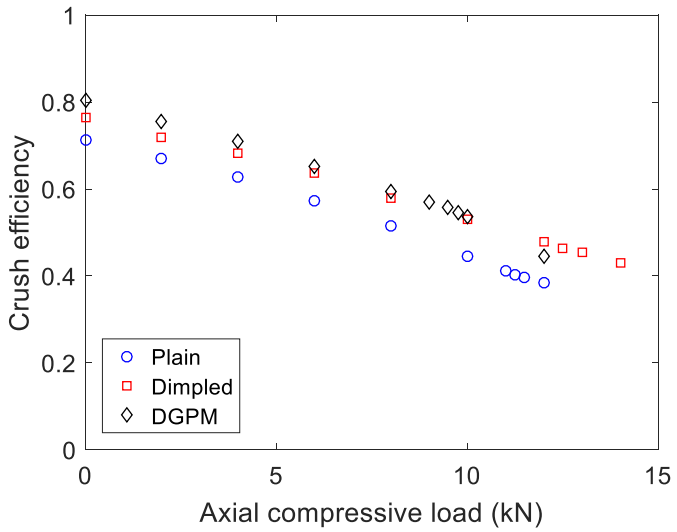

Fig. 7.13. Crush efficiency under different axial compressive loads

The deformed shapes of the three columns under combined axial compressive and lateral impact loads are presented in Fig. 7.14. To evaluate columns' ability of maintaining stability, the ratio $P_{axial,c}/P_y$ is normally used, where $P_{axial,c}$ refers to the critical load of the column (i.e. the maximum axial compressive load that

can be applied before the column losing stability under impact) and P_y refers to the squash load of the column. The numerical results are listed in Table 7.1. The critical loads $P_{axial,c}$ are determined on a trial and error basis. Although the dimpled columns do not show an advantage in terms of the ratio $P_{axial,c}/P_y$, the critical load of the dimpled column is about 11.1% greater than that of the comparable plain column.

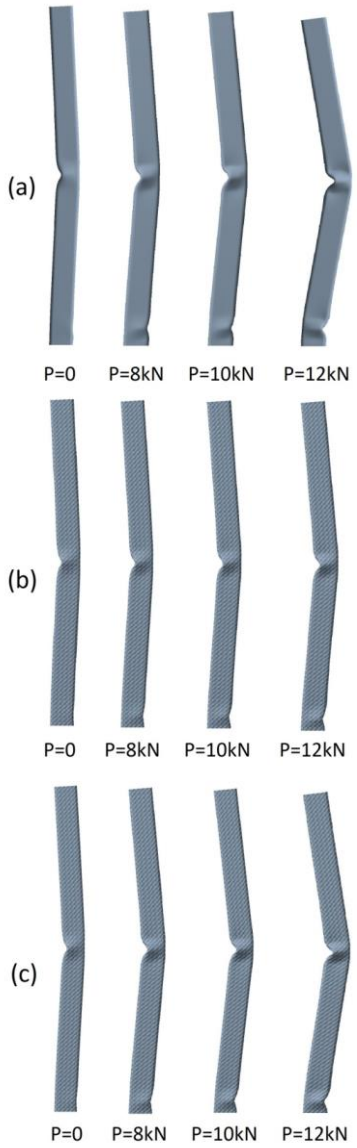

Fig. 7.14. Deformed shapes of (a) plain, (b) dimpled and (c) DGPM columns under combined axial compressive and lateral impact loads

Table 7.1. Critical and squash loads of plain, dimpled and DGPM columns

	$P_{axial,c}$ (kN)	P_y (kN)	$P_{axial,c}/P_y$
Plain	11.25	36.70	30.7%
Dimpled	12.50	41.34	30.2%
DGPM	9.75	33.02	29.5%

7.4 Effects of the support conditions

Plain, dimpled and DGPM columns were analysed under two different support conditions to further investigate the behaviour of dimpled columns under lateral impact loads. The two additional support conditions are fully fixed at both ends and roller supported at both ends. Axial compressive loads were not applied in these conditions. The mean forces, peak forces and crush efficiencies for the three types of columns under the additional two support conditions are presented in Fig. 7.15. It can be found that when the samples are fully fixed at both ends, the mean force, maximum force and crush efficiency of the dimpled column are 7.3%, 0.9% and 6.4% higher than those of the plain column, respectively. When the samples are roller supported at both ends, the mean force, maximum force and crush efficiency of the dimpled column are 16.1%, 15.5% and 0.5% higher than those of the plain column, respectively.

Through comparing the mean and peak forces, it is noticed that the difference in crush efficiencies is mainly caused by peak forces. The advantage of dimpled and DGPM columns in crush efficiency is mainly due to the relatively lower peak impact forces, vice versa. Taking the results presented in Section 7.3 into

account, it appears that advantage of dimpled and DGPM columns in peak forces can only be found when at least one end is fully fixed. When the columns are fixed supported at both ends, peak forces are observed when the fixed ends start to yield. The propagation of yielding effect in dimpled and plain columns are shown in Fig.7.16. The yielding effect near the dimpled column's fixed ends develops from the trough regions of dimples. A similar phenomenon can be observed in the DGPM column as well. Comparing to the continuous yielding effect in plain columns, the discrete yielding effect in dimpled and DGPM columns is in favour of reducing the peak impact force. By contrast, the material near both ends does not experience yielding effects under the roller-roller support condition, and the yielding effect can only be observed near the impact location (i.e. mid-span) when peak forces appears. As shown in Fig. 7.17, the development of the yielding effect in plain and dimpled columns are similar. Therefore, the advantage of dimpled and DGPM columns in the peak impact force no longer exists.

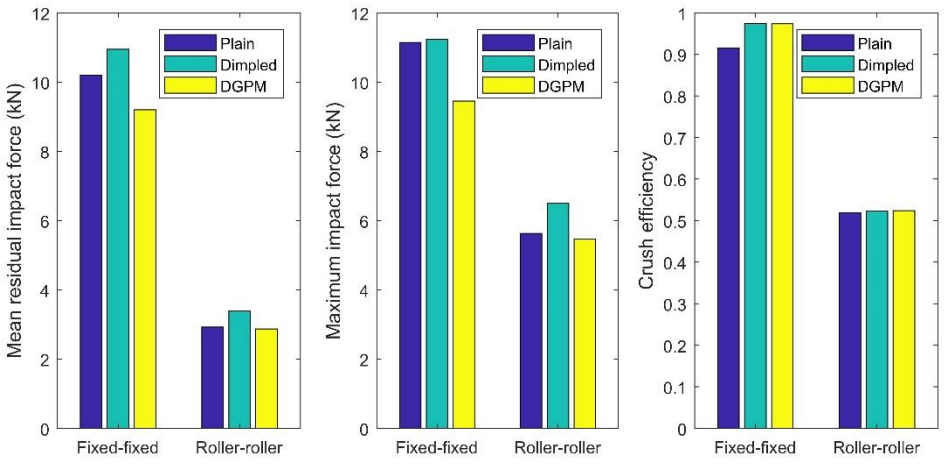

Fig. 7.15. (a) Mean impact force, (b) peak force and (c) crush efficiency under fixed-fixed and roller-roller support conditions

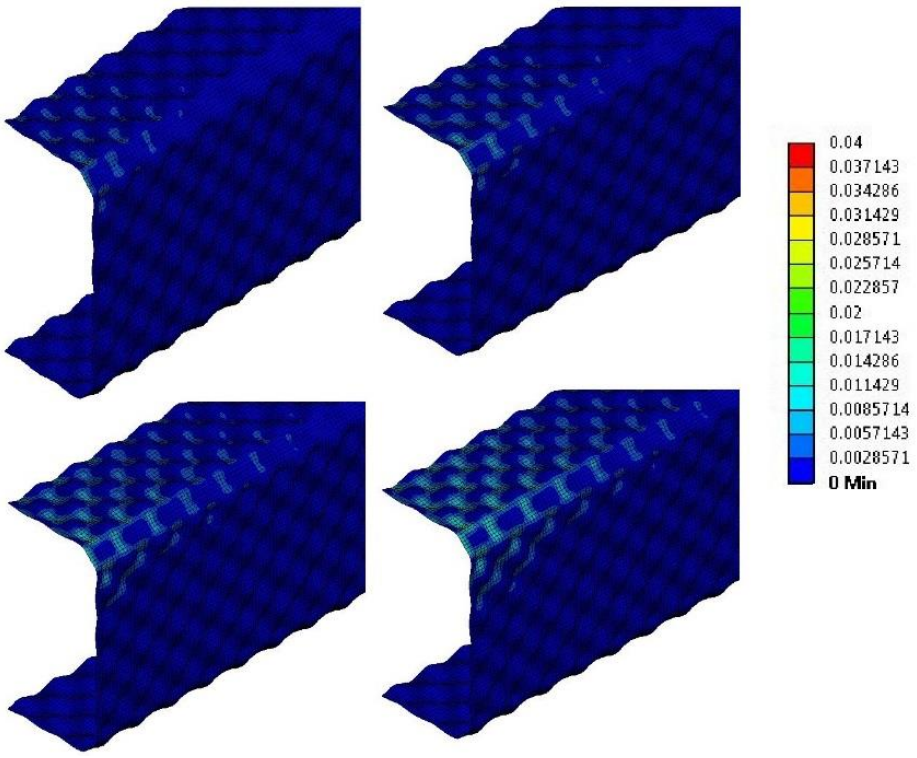

Fig. 7.16. Propagation of yielding near the fixed end in dimpled samples

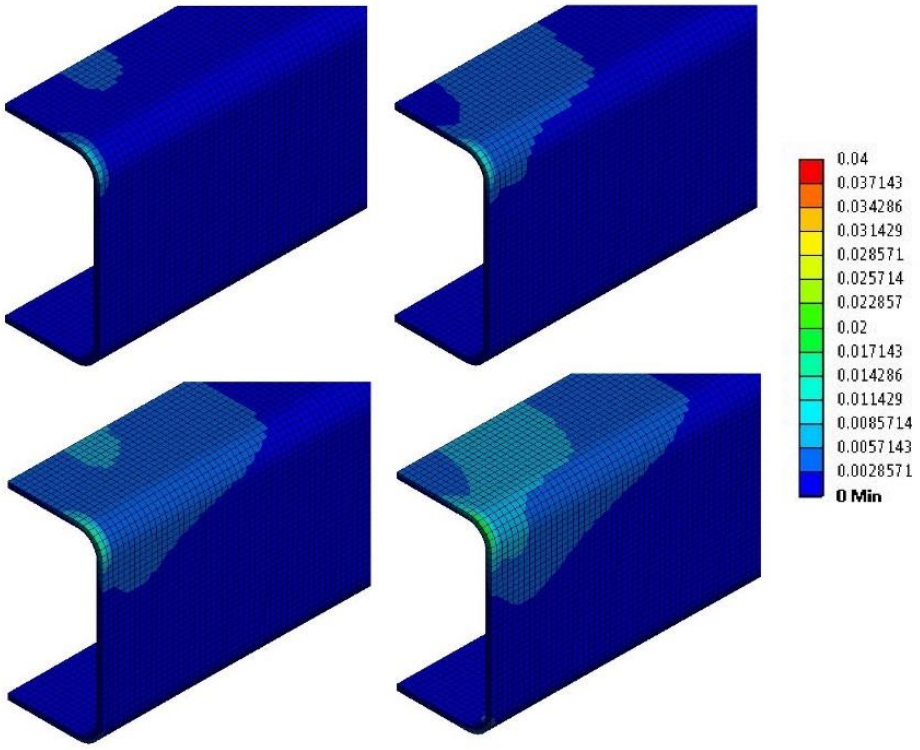

Fig. 7.17. Propagation of yielding near the fixed end in plain samples

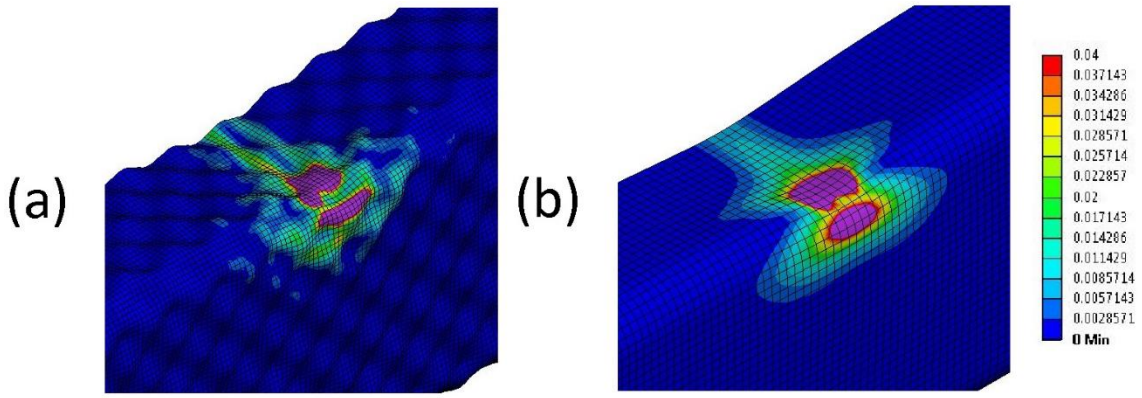

Fig. 7.18. Plastic strain near the impact location of roller-roller supported (a) dimpled and (b) plain columns when the peak impact force appears

To further justify this theory, another support condition was analysed. The columns are fully fixed at one end and free at the other end (i.e. cantilever columns). This support condition can be commonly found in engineering applications such as guard bars and bollards. Three different impact locations were selected: (1) quarter-span, (2) mid-span, (3) three quarter-span. In all three cases, the peak forces are the results of the plastic deformation near the fixed end. The results are shown in Fig. 7.19. Similar to the fixed-fixed and fixed-roller support conditions, dimpled and DGPM columns have relatively high mean impact forces and low maximum impact forces, comparing to the plain counterparts. The propagation patterns of the yielding effect are very similar to those in the fixed-fixed and fixed-roller supported cases as well. Therefore, it can be concluded that the introduced dimpled geometry contributes to reducing peak impact forces and increasing crush efficiencies when at least one end is fully fixed.

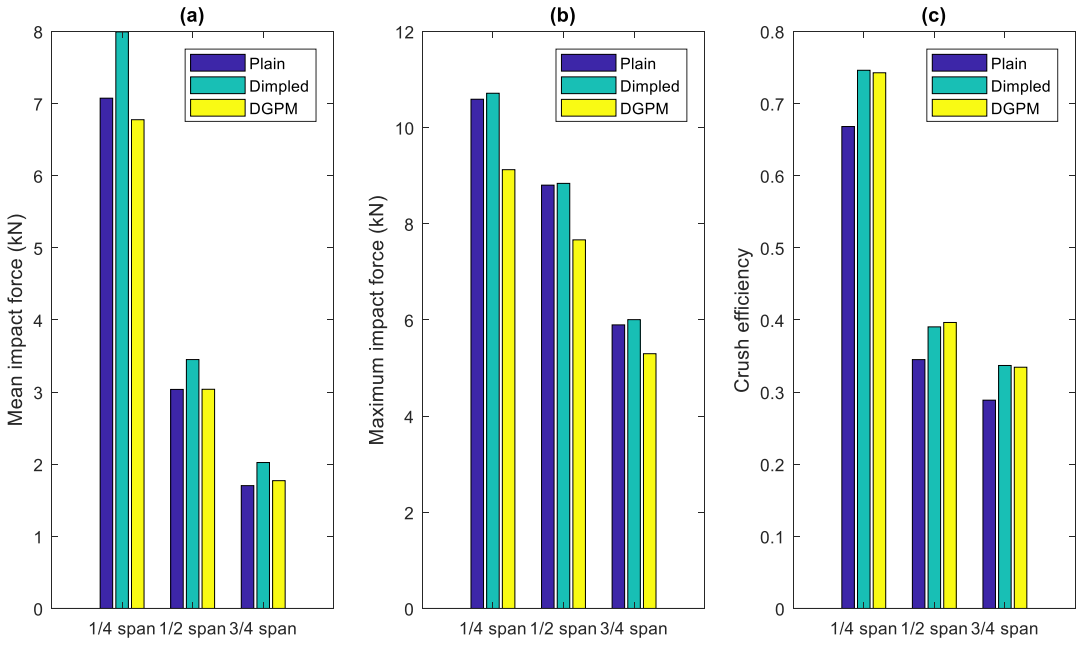

Fig. 7.19. (a) Mean force, (b) peak force and (c) crush efficiency under fixed-free support conditions and different impact locations

7.5 Summary

In this chapter, simulations were performed to study the response of plain and dimpled columns to lateral impact loads. The FE method was validated by comparing to the experimental and numerical results published by other researchers. The fixed-roller support condition was selected to be the baseline to analyse the failure mechanism of plain, dimpled and DGPM columns under lateral impact loads. The study was then extended by applying different axial compressive loads and different support conditions. The same impact energy and dimensions of columns were used in all cases, and the following conclusions can be made from the study:

- The FE method was validated, the results obtained using the FE method agree well with the experimental and numerical results presented in previous publications, including the failure mode, instantaneous crushing force and lateral displacement.
- Under the fixed-roller support condition and lateral impact loads, plain, dimpled and DGPM columns show an initial (1st) peak force, a second (2nd) peak force, a maximum (3rd) peak force and the residual impact force. The 1st peak forces of dimpled and DGPM columns are not distinct, due to the small yielding area when the 1st peak force occurs.
- When the axial compressive loads are applied, the mean impact forces and crush efficiencies of the dimpled column are up to 32.6% and 20.4% greater than those of the plain column, respectively. Additionally, the critical axial load of the dimpled column is 11.1% greater than that of the plain column.
- The fixed-fixed, roller-roller, fixed-free support conditions were analysed, where the fixed-free support condition was analysed with three different impact locations. Results reveal that the introduced dimpled geometry can help reduce maximum impact forces and therefore increase crush efficiencies. But this is only valid when at least one end is fully fixed.

Chapter 8 Conclusions and future work

This thesis has investigated the energy absorption characteristics of the thin-walled columns with dimpled features under various types of impact loading conditions. In this study, the experimental, the explicit finite element methods were used. In this chapter, the main findings are listed. General discussions are made, followed by some recommendations for the future work.

8.1 Main findings

- The UltraSTEEL® dimpling forming process and the tensile tests were simulated, using quasi-static FE simulations. The FE model was created based on a small square plate, by applying symmetric boundary conditions. Experimental quasi-static tensile tests were conducted, which reveals that after the forming process, the yield and ultimate strengths are increased by 25.4% and 8.4%, respectively.
- Dynamic experimental crushing tests were conducted on open section plain and dimpled columns. The experimental results reveal that the specific energy absorption (SEA) values of the open section dimpled columns are approximately 10% higher than those of the plain counterparts. The experimental tests were replicated using the explicit FE method.

- The experimental and numerical results were compared in terms of failure mechanisms, impact force - axial displacement curves, energy absorption - axial displacement curves, and SEA values. Good agreement was observed on all four aspects. To further validate the explicit FE method, it was utilized to simulate the quasi-static crushing tests, a good agreement was found as well.
- The validated explicit FE method was used to predict the crashworthiness of square shape closed section dimpled steel columns under axial impact loads. It was found that after introducing the dimpled feature, although the failure mechanism is very similar to the plain counterpart, the wavelength of the dimpled column is not a constant.
- It was found that the forming depth considerably influences the mechanical properties and the crashworthiness of dimpled columns. An optimization study on the forming depth reveals that as the forming depth increasing, the equivalent yield strength of dimpled plates tends to peak when the forming depth is approximately 1 mm. It is essentially a trade-off between the work hardening and stress concentration effects. Moreover, the optimal forming depth in terms of the specific energy absorption is nearly proportional to the gauge thickness. It is a combined effect of the dimpled geometry and the material's mechanical properties.
- When subjected to inclined axial impact loads, dimpled columns maintain the regular folding mode at an inclined angle which is 4 degrees larger than the plain counterparts. Additionally, plain and dimpled columns perform similarly when resisting the global bending mode.

- The interlocking mechanism between two dimpled plates were investigated numerically. A three-stage variation of the effective friction coefficient was identified. For dimpled plates, the relation between the effective and actual friction coefficients is non-linear and it may be approximated as a quadratic equation.
- For multi-layer dimpled columns, the extra layers will improve the resistance to axial impact loads, causing the crushing force pattern to shift in the meantime. In such circumstances, the energy absorbed by the layer-to-layer interaction can be promoted by introducing more layers of columns. Moreover, the influence of the layer-to-layer gap size is negligible.
- The response of dimpled thin-walled columns to lateral impact loads was studied numerically. Maximum impact forces appear when the plastic deformation near the fixed end starts to develop. The dimpled geometry contributes to reducing maximum impact forces, because the yielding effect propagates discretely in dimpled columns, contrasting to a continuous yielding effect propagation in plain ones. But it is valid only when at least one end of the column is fully fixed. This statement is further justified by the numerical results obtained under other support conditions. Additionally, a parametric study on axial compressive loads reveals that the crush efficiencies of dimpled columns are up to 20.4% higher than those of the plain counterparts, and the critical axial loads of dimpled columns are considerably greater than those of the plain counterparts.

8.2 General discussions and future work

In the present study, the energy absorption characteristics of dimpled steel structures were investigated. However, there are still several limitations of the present study, due to the reasons such as the limited time, computational power and budget for experimental tests. The limitations are pointed out in this section, and the future work is suggested accordingly.

- In the explicit dynamics FE simulations, by using shell elements, uniform thicknesses were assigned to the dimpled plates. However, the thicknesses at different regions are slightly different in reality. Additionally, the mechanical properties of the dimpled plates were assumed to be homogeneous in the impact simulations, whereas they are not homogeneous in reality. The reasons of adopting these simplifications is that in explicit dynamics FE analysis, the time step is proportional to the minimum element size. Therefore, using solid elements will dramatically increase the demanded computational resource. Although it was validated that the explicit dynamics FE method in the present study can accurately predict the failure modes and impact forces, it may not be used to predict the stress/strain distributions throughout the thickness, nor analysing the local fractures. In the future, with the aid of high performance computers and more advanced FE modelling methods/algorithms, the non-uniform thickness, material properties and the stress/strain distributions throughout the thickness should be considered.

- In the present study, some structural failure modes such as ductile tearing and splitting were excluded. The reasons are: (1) these failure modes were not observed in the experimental tests and (2) including these failure modes demands considerably more computing time. However, it has been reported that these failure modes do occur in some cases. The dynamic experimental tests in the present study were conducted with two different kinetic energies, which caused the most typical strain rates and failure modes for the vehicular systems in collisions. In the future, the numerical method should be modified to take other failure modes into account. To improve the reliability of the numerical study, experimental tests under more extreme test conditions need to be performed. The experimental results and phenomenon will be used to validate the modified numerical method.
- The present study focuses on the steel material. By using a similar approach, the present study can be extended to introducing the dimpled features in other materials such as aluminium or stainless steel. It is meaningful because other materials are expected to perform differently due to their own work hardening curves and strain rate sensitivity.
- The present study employs the Cowper-Symonds material model to describe the strain rate sensitivity of the plain and dimpled steel materials. It has been assumed that the strain rate coefficients do not change after the cold-roll forming process. The strain rate coefficients in this thesis were adopted from previously published research papers. The author would suggest to perform high strain rate tensile tests on the plain and dimpled materials in future research for two purposes: (1) evaluating the change in

the strain rate coefficients due to the cold-roll forming process and (2) calibrating the coefficients for more accurate numerical results.

- As introduced in Chapter 6, extra energy could be absorbed through the interaction between dimpled plates. Furthermore, the interaction can be promoted by increasing the normal pressure between walls. Comparing to multi-layer columns, material-filled (e.g. foam-filled, concrete-filled, etc.) dimpled columns are expected to have significantly higher normal pressures when being crushed. Therefore, the energy absorption characteristics of material-filled dimpled columns is a promising research topic in the future.

Reference

[1] Wierzbicki T, Abramowicz W. On the Crushing Mechanics of Thin-Walled Structures. Journal of Applied Mechanics 1983;50:727-734.

[2] Alexander J.M. An approximate analysis of the collapse of thin cylindrical shells under axial loading. The Quarterly Journal of Mechanics and Applied Mathematics 1960;13:1-9.

[3] Abramowicz W, Jones N. Dynamic axial crushing of square tubes. International Journal of Impact Engineering 1984;2(2):179-208.

[4] Abramowicz W, Jones N. Dynamic progressive buckling of circular and square tubes. International Journal of Impact Engineering 1986;4(4):243-270.

[5] Abramowicz W, Wierzbicki T. Axial crushing of multicorner sheet metal columns. Journal of Applied Mechanics ASME 1989;56(1):113-120.

[6] Abramowicz W, Jones N. Dynamic axial crushing of circular tubes. International Journal of Impact Engineering 1984;2(3):263-281.

[7] Jones N. (1990). Structural Impact (pp. 402-404). Cambridge University Press.

[8] Tang Z, Liu S, Zhang Z. Energy absorption properties of non-convex multi-corner thin-walled columns. Thin-Walled Structures 2012;51:112-120.

[9] Abbasi M, Reddy S, Ghafari-Nazari A, Fard M. Multiobjective crashworthiness optimization of multi-cornered thin-walled sheet metal members. Thin-Walled Structures 2015;89:31-41.

[10] Reddy S, Abbasi M, Fard M. Multi-cornered thin-walled sheet metal members for enhanced crashworthiness and occupant protection. Thin-Walled Structures 2015;94:56-66.

[11] Wu S, Sun G, Wu X, Li G, Li Q. Crashworthiness analysis and optimization of fourier varying section tubes. International Journal of Non-linear Mechanics 2017;92:41-58.

[12] Sun G, Pang T, Fang J, Li G, Li Q. Parameterization of criss-cross configurations for multiobjective crashworthiness optimization. International Journal of Mechanical Sciences 2017;124-125:145-157.

[13] Chen W, Wierzbicki T. Relative merits of single-cell, multi-cell and foam-filled thin-walled structures in energy absorption. Thin-Walled Structures 2001;37(4):287-306.

[14] Kim HS. New extruded multi-cell aluminium profile for maximum crash energy absorption and weight efficiency. Thin-Walled Structures 2002;40(4):311-327.

[15] Zhang X, Cheng G, Zhang H. Theoretical prediction and numerical simulation of multi-cell square thin-walled structures. Thin-Walled Structures 2006;44:1185-1191.

[16] Jusuf A, Dirgantara T, Gunawan L, Putra IS. Crashworthiness analysis of multi-cell prismatic structures. International Journal of Impact Engineering 2015;78:34-50.

[17] Jusuf A, Dirgantara T, Gunawan L, Putra IS. Numerical and experimental study of single-walled and double-walled columns under dynamic axial loading. Journal of Mechanical Engineering 2012;9(2):53-72.

[18] Zhang X, Cheng G. A comparative study of energy absorption characteristics of foam-filled and multi-cell square columns. International Journal of Impact Engineering 2007;34:1379-1752.

[19] Hou S, Li Q, Long S, Yang X, Li W. Multiobjective optimization of multi-cell sections for the crashworthiness design. International Journal of Impact Engineering 2008;35:1355-1367.

[20] Zhang Z, Liu S, Tang Z. Design optimization of cross-sectional configuration of rib-reinforced thin-walled beam. Thin-Walled Structures 2009;47:868-878.

[21] Najafi A, Rais-Rohani M. Mechanics of axial plastic collapse in multi-cell, multi-corner crush tubes. Thin-Walled Structures 2011;49:1-12.

[22] Zhang X, Zhang H. Energy absorption of multi-cell stub columns under axial compression. Thin-Walled Structures 2013;68:156-163.

[23] Tran TN, Hou S, Han X, Tan W, Nguyen NT. Theoretical prediction and crashworthiness optimization of multi-cell triangular tubes. Thin-Walled Structures 2014;82:183-195.

[24] Wu S, Zheng G, Sun G, Liu Q, Li G, Li Q. On design of multi-cell thin-wall structures for crashworthiness. International Journal of Impact Engineering 2016;88:102-117.

[25] Estrada Q, Szwedowicz D, Silva-Aceves J, Majewski T, Vergara-Vazquez J, Rodriguez-Mendez A. Crashworthiness behaviour of aluminium profiles with

holes considering damage criteria and dame evolution. International Journal of Mechanical Science 2017;131-132:776-791.

[26] Vinayagar K, Kumar A. Crashworthiness analysis of double section bi-tubular thin-walled structures. Thin-Walled Structures 2017;112:184-193.

[27] Qiu N, Gao Y, Fang J, Feng Z, Sun G, Li Q. Crashworthiness analysis and design of multi-cell hexagonal columns under multiple loading cases. Finite Element in Analysis and Design 2015;104:89-101.

[28] Tran TN, Hou S, Han X, Chau MQ. Crushing analysis and numerical optimization of angle element structures under axial impact loading. Composite Structures 2015;119:422-435.

[29] Zhang X, Zhang H. Some problems on the axial crushing of multi-cells. International Journal of Mechanical Sciences 2015;103:30-39.

[30] White M, Jones N, Abramowicz W. A theoretical analysis for the quasi-static axial crushing of top-hat and double-hat thin-walled sections. International Journal of Mechanical Sciences 1999;41:209-233.

[31] Ly HA, Nguyen HH, Thai-Quang T. Geometrical Optimization of Top-Hat Structures Subject to Axial Low Velocity Impact Load Using Numerical Simulations. International Journal of Mechanical Engineering and Applications 2015;3:40-48.

[32] Zhang X, Wen Z, Zhang H. Axial crushing and optimal design of square tubes with graded thickness. Thin-Walled Structures 2014;84:263-274.

[33] Asanjarani A, Dibajian SH, Mahdian A. Multi-objective crashworthiness optimization of tapered thin-walled square tubes with indentations. Thin-Walled Structures 2017;116:26-36.

[34] Jiang H, Ren Y, Gao B. Research on the progressive damage model and trigger geometry of composite waved beam to improve crashworthiness. Thin-Walled Structures 2017;119:531-543.

[35] Huh H, Kang WJ. Crash-worthiness assessment of thin-walled structures with the high-strength steel sheet. International Journal of Vehicle Design 2002;30(1/2):1-21.

[36] Schneider F, Jones N. Impact of thin-walled high-strength steel structural sections. In: Proceedings of the Institution of Mechanical Engineering, Part D: Journal of Automobile Engineering; 2004;218(2):131-158.

[37] Xue P, Iqbal N, Liao HJ, Wang B, Li YL. Experimental study, on strain rate sensitivity of ductile porous irons. International Journal of Impact Engineering 2012;48:82-86.

[38] Iqbal N, Xue P, Liao HJ, Wang B, Li YL. Material characterization of porous bronze at high strain rates. Material Science and Engineering A;2011:4408-4412.

[39] Ying L, Dai M, Zhang S, Ma H, Hu P. Multiobjective crashworthiness optimization of thin-walled structures with functionally graded strength under oblique impact loading. Thin-Walled Structures 2017;117:165-177.

[40] Tarigopula V, Langseth M, Hopperstad OS, Clausen AH. Axial crushing of thin-walled high-strength steel sections. International Journal of Impact Engineering 2006;32:847-882.

[41] Lam K, Behdinan K, Cleghorn W. A material and gauge thickness sensitivity analysis on the NVH and crashworthiness of automotive instrument panel support. Thin-Walled Structures 2003;41:1005-1018.

[42] Fang J, Qiu N, An X, Xiong F, Sun G, Li Q. Crashworthiness design of a steel-aluminium hybrid rail using multi-response objective-oriented sequential optimization. Advances in Engineering Software 2017;112:192-199.

[43] Reddy TY, Zhang E. Effect of strain hardening on the behaviour of axially crushed cylindrical tubes. In: Advances in engineering plasticity and its applications, Amsterdam; 1993: 775-762.

[44] Shaw MC, Sata T. The plastic behaviour of cellular materials. International Journal of Mechanical Engineering 1966;8(7):469-472.

[45] Reid SR, Reddy TY, Gray MD. Static and dynamic axial crushing of foam-filled sheet metal tubes. International Journal of Mechanical Science 1986;28(5):295-322.

[46] Zarei HR, Kroger M. Optimization of the foam-filled aluminium tubes for crush box applications. Thin-Walled Structures 2008;46:214-221.

[47] Abramowicz W, Wierzbicki T. Axial crushing of foam-filled columns. International Journal of Mechanical Science 1988;30(3-4):263-271.

[48] Hanssen A, Langseth M, Hopperstad O. Static crushing of square aluminium extrusions with aluminium foam filler. International Journal of Mechanical Sciences 1999;41:967-993.

[49] Hanssen AG, Langseth M, Hopperstad OS. Static and dynamic crushing of square aluminium extrusions with aluminium foam filler. International Journal of Impact Engineering 2000;24:347-383.

[50] Seitzberger M, Rammerstorfer FG, Gradinger R. Experimental studies on the quasi-static axial crushing of steel columns filled with aluminium foam. International Journal of Solids and Structures 2000;37:4125-4147.

[51] Seitzberger M, Rammerstorfer FG, Degischer HP. Crushing of axially compressed steel tubes filled with aluminium foam. Acta Mechanica 1997;125(1-4):93-105.

[52] Zhang Y, Lu M, Sun G, Li G, Li Q. On functionally graded composite structures for crashworthiness. Composite Structures 2015;132:393-405.

[53] Thorton PM, Mahmood HF, Magee CL. Energy absorption by structural collapse. In: N. Jones and T. Wierzbicki (eds) Structural Crashworthiness, Butterworrths, 1983: 96-117.

[54] Song J, Chen Y, Lu G. Axial crushing of thin-walled structures with origami patterns. Thin-Walled Strucures 2012;54:65-71.

[55] M. Bambach, H. Jama, X. Zhao, R. Grzebieta. Hollow and concrete filled steel hollow sections under transverse impact loads. Eng. Struct. 2008;30: 2859-2870.

[56] I. Harik, A. Shaaban, H. Gesund, G. Valli, S. Wang. United States bridge failures, 1955-1988. J. Perform Constr. Facil. 1990;4: 272-277.

[57] K. Wardhana, F.C. Hadipriono. Analysis of recent bridge failures in the United States. J. Perform Constr. Facil. 2003;17: 144-150.

[58] J. Fang, Y. Gao, G. Sun, Y. Zhang, Q. Li. Parametric analysis and multi objective optimization for functionally graded foam-filled thin-walled tube under lateral impact. Computational Mater. Sci. 2014;90: 265-275.

[59] Kecman D. Bending collapse of rectangular section tubes in relation to the bus roll over probems. PhD thesis, Cranfield Institute of Technology 1979.

[60] Kecman D. Bending collapse of rectangular and square section tubes. International Journal of Mechanical Science 1983;25(9-10):623-636.

[61] Abramowicz W. Simplified crushing analysis of thin-walled columns and beams. Engineering Transactions 1983;29:3-27.

[62] J.H. Liu, N. Jones. Experimental investigation of clamped beams struck transversely by a mass. Int. J. Impact. Eng. 1987;6(4): 303-335.

[63] J. Yu, N. Jones. Further experimental investigation on the failure of clamped beams under impact loads. Int. J. Solid Struct. 1991;27(9): 1113-1137.

[64] Wierzbicki T, Recke L, Abramowicz W, Guolami T, Huang J. Stress profile in thin-walled prismatic columns subjected crush loading - II. Bending. Computers & Structures 1994;51(6): 625-641.

[65] M. Zeinoddini, J.E. Harding, G.A.R. Parke. Dynamic behaviour of axially pre-loaded tubular steel members of offshore structures subjected to impact damage. Ocean Eng. 1999;26:963-978.

[66] M. Zeinoddini, G.A.R. Parke, J.E. Harding. Axially pre-loaded steel tubes subjected to lateral impacts: an experimental study. Int. J. Impact Eng. 2002;27: 669-690.

[67] M. Zeinoddini, J.E. Harding, G.A.R. Parke. Axially pre-loaded steel tubes subjected to lateral impacts (a numerical study). Int. J. Impact Eng. 2008;35: 1267-1279.

[68] H. Al-Thairy, Y.C. Wang. A numerical study of the behaviour and failure modes of axially compressed steel columns subjected to transverse impact. Int. J. Impact Eng. 2011;38:732-744.

[69] Al-Thairy, Y.C. Wang. A simplified analytical method for predicting the critical velocity of transverse rigid body impact on steel columns. Int. J. Impact Eng. 2013;58:39-54.

[70] Al-Thairy, Y.C. Wang. A simplified analytical method for predicting the critical velocity of vehicle impact on steel columns. J. Constr. Steel Res. 2014;92:136-149.

[71] Al-Thairy, Y.C. Wang. Simplified FE vehicle model for assessing the vulnerability of axially compressed steel columns against vehicle frontal impact. J. Constr. Steel Res. 2014;102:190-203.

[72] S. Santosa, T. Wierzbicki. Effect of an ultralight metal filler on the bending collapse behaviour of thin-walled prismatic columns. Int. J. Mech. Sci. 1999;41(8): 995-1019.

[73] W. Chen. Experimental and numerical study on bending collapse of aluminium foam-filled hat profiles. Int. J. Solids and Struct. 2001;38@7919-7944.

[74] S. Shahbeyk, A. Vafai, H.E. Estekanchi. A parametric study of the bending crash performance of empty and metal foam-filled box-beams. Int. J. Crashworthiness. 2004;9(6):643-652.

[75] J. Fang, Y. Gao, G. Sun, Y. Zhang, Q. Li. Parametric analysis and multi objective optimization for functionally graded foam-filled thin-walled tube under lateral impact. Computational Mater. Sci. 2014;90: 265-275.

[76] R. Wang, L.H. Han, C.C. Hou. Behaviour of concrete filled steel tubular (CFST) members under lateral impact: Experiment and FEA model. J. Constr. Steel Res. 2013;80:188-201.

[77] M. Yousuf, B. Uy, Z. Tao, A. Remennikov, J.Y.R. Liew. Transverse impact resistance of hollow and concrete filled stainless steel columns. J. Const. Steel Res. 2013;82:177-189.

[78] M. Yousuf, B. Uy, Z. Tao, A. Remennikov, J.Y.R. Liew. Impact behaviour of pre-compressed hollow and concrete filled mild and stainless steel columns. J. Constr. Steel Res. 2014;96: 54-68.

[79] Smith R, Altenhof W, Lapain M. Transverse impact loading of aluminium foam filled braided stainless steel tubes. International Journal of Impact Engineering 2016;88:214-226.

[80] Y. Wang, X. Qian, J.Y.R. Liew, M.H. Zhang. Experimental behaviour of cement filed pipe-in-pipe composite structures under transverse impact. Int. J. Impact Eng. 2014;72: 1-16.

[81] J.C. Teng, J.F. Chen, S.T. Smith, L. Lam. FRP – strengthened RC structures. West Sussex, UK: John Wiley & Sons, Ltd. 2001.

[82] S. Rizkalla, T. Hassan, N. Hassan. Design recommendations for the use of FRP for reinforced and strengthening of concrete structures. Prog. Struct. Eng. Mater. 2003;5: 16-28.

[83] M.R. Bambach, M. Elchalakani, X. Zhao. Composite steel-CFRP SHS tubes under axial impact. Compos. Struct. 2009;87:282-292.

[84] M. Bambach, H. Jama, M. Elchalakani. Static and dynamic axial crushing of spot-welded thin-walled composite steel-CFRP square tubes. Int. J. Impact Eng. 2009;36:1083-1094.

[85] M. Bambach, M. Elchalakani. Plastic mechanism analysis of steel SHS strengthened with CFRP under large axial deformation. Thin-Walled Struct. 2007;45:159-170.

[86] M.I. Alam, S. Fawzia. Numerical studies on CFRP strengthened steel under transverse impact. Composite Struct. 2015;120: 428-441.

[87] Alam MI, Fawzia S, Liu X. Effect of bond length on the behaviour of CFRP strengthened concrete-filled steel tubes under transverse impact. Composite Structures 2015;132:898-914.

[88] Cho SR, Truong DD, Shin HK. Repeated lateral impacts on steel beams at room and sub-zero temperatures. International Journal of Impact Engineering 2014;72:75-84.

[89] Demir I, Sayman O, Dogan A, Arikan V, Arman Y. The effects of repeated transverse impact load on the burst pressure of composite pressure vessels. Composites: Part B 2015;68:121-125.

[90] Hadley Industries plc, PO Box 92, Downing Street, Smethwick, West Midlands, B66 2PA, UK

[91] Nguyen VB, Wang CJ, Mynors DJ, English MA, Castellucci MA. Dimpling process in cold roll metal forming by finite element modelling and experimental validation. Journal of Manufacturing Process 2014;16:363-372.

[92] Nguyen VB, Wang CJ, Mynors DJ, English MA, Castellucci MA. Compression tests of cold-formed plain and dimpled steel columns. Journal of Constructional Steel Research 2012;49:20-29.

[93] J. Collins, M.A. Castellucci, I. Pillinger, P. Hartley. The influence of tool design on the development of localised regions of plastic deformation in sheet metal formed products to improve structural performance. In: Proceeding of the 10th international conference on metal forming. Paper No. 68, 2004.

[94] Nguyen VB, Wang CJ, Mynors DJ, English MA, Castellucci MA. Mechanical behaviour of cold-rolled formed dimpled steel. Steel Res Int 2011; Special Issue: 1072-1077

[95] Nguyen VB, Wang CJ, Mynors DJ, Castellucci MA, English MA. Finite Element simulation on mechanical and structural properties of cold-formed dimpled steel. Thin-Walled Structures 2013;64:13-22.

[96] Nguyen VB, Mynors DJ, Wang CJ, Castellucci MA, English MA. Analysis and design of cold-formed dimpled steel columns using Finite Element techniques. Finite Elements in Analysis and Design 2016;108:22-31.

[97] Nguyen VB, English MA. Effects of cold roll dimpling process on mechanical properties of dimpled steel. Paper presented at the 12th International Conference on the Technology of Plasticity, Cambridge, UK, 2017.

[98] S.R. Wu, L. Gu. (2012) Introduction to the explicit finite element method for nonlinear transient dynamics. Wiley press.

[99] ANSYS, Inc. (2009). Chapter 1: Introduction to Explicit Dynamics [PowerPoint slides]. ANSYS, Inc. Proprietary.

[100] ANSYS, Inc. (2009). Chapter 8: Explicit Dynamics: Analysis Settings [PowerPoint slides]. ANSYS, Inc. Proprietary.

[101] ANSYS, Inc. (2009). Chapter 6: Explicit Dynamics: Meshing [PowerPoint slides]. ANSYS, Inc. Proprietary.

[102] ANSYS, Inc. (2009). Chapter 7: Body Interactions [PowerPoint slides]. ANSYS, Inc. Proprietary.

[103] efunda. Buckling of Columns. [online] Available at: http://www.efunda.com/formulae/solid_mechanics/columns/intro.cfm [Accessed 27 Nov 2017].

[104] ANSYS® Academic Research, Release 17.1.